Selective Laser Melting of An Advanced $Al\text{-}Al_2O_3$ Nanocomposite

Quanqan Han

School of Engineering

Cardiff University

This thesis is submitted in fulfilment of the requirement of the degree of

Doctor of Philosophy

August 2017

I dedicate this to my parents and my friends who have always lovingly supported me.

Declaration and Statements

DECLARATION

This work has not been submitted in substance for any other degree or award at this or any other university or place of learning, nor is being submitted concurrently in candidature for any degree or other award.

Signed..... (Quanquan Han) Date .....

STATEMENT 1

This thesis is being submitted in partial fulfilment of the requirements for the degree of Doctor of Philosophy (PhD).

Signed ..... (Quanquan Han) Date .....

STATEMENT 2

This thesis is the result of my own independent work/investigation, except where otherwise stated, and the thesis has not been edited by a third party beyond what is permitted by Cardiff University's Policy on the Use of Third Party Editors by Research Degree Students. Other sources are acknowledged by explicit references. The views expressed are my own.

Signed ..... (Quanquan Han) Date .....

STATEMENT 3

I hereby give consent for my thesis, if accepted, to be available online in the University's Open Access repository and for inter-library loan, and for the title and summary to be made available to outside organisations.

Signed ..... (Quanquan Han) Date .....

Acknowledgements

It has been one tough journey but I am truly blessed to have so many people that have accompanied me when I boarded this ship. The following are those people who in different ways, have helped and contributed to my PhD study.

First, I would like to sincerely appreciate my supervisor Prof. Rossitza Setchi, and co-supervisors, Prof. Sam L. Evans and Prof. Bhushan L. Karihaloo, for giving me this opportunity to carry out this interesting research. They have consistently given me valuable guidance and inspiration throughout this study, which have helped me bring it to completion. Prof. Setchi not only provides me with fantastic platform to carry out my research at Cardiff University but also sponsors me to attend international conferences abroad, which allows me to meet and communicate with international experts on additive manufacturing.

I would also like to thank my colleagues, Mr. Qixiang Feng, Mr. Syafiq Abdull Sukor, for their kind support, comments and feedback. Dr. Franck Lacan, Dr. Emmanuel Brousseau, Dr. David Clark, Dr Chunlei Qiu and Prof. Dongdong Gu are gratefully appreciated for their assistance with the experiments and providing feedback on the papers. In addition, I gratefully appreciate the financial support of China Scholarship Council and Cardiff University, which allows me to conduct my study without worrying about any financial issues.

Finally, I would like to express my deepest appreciation to my parents for their endless love and support. I am fully aware of the fact that this thesis would have never been completed without their love and support.

Abstract

Selective laser melting (SLM) has been widely used to manufacture customised metallic parts because it provides an integrated way to manufacture three-dimensional (3D) parts from computer-aided design models after several sub-processes. On the other hand, aluminium-based nanocomposites are widely used in the aerospace and automotive industries due to their light weight, high specific strength, excellent wear resistance, but their manufacturability and mechanical properties are not well understood when these new materials are employed in SLM. This is an important consideration because, compared with traditional manufacturing technologies, SLM offers the ability to manufacture engineering parts with very complex geometries by employing a layer-by-layer manufacturing principle. Hence, this thesis systematically studies the SLM of an advanced Al-Al_2O_3 nanocomposite that is synthesised using high-energy ball-milling (HEBM) process.

The aim of this study is to use SLM to fabricate a nearly full dense Al-Al_2O_3 nanocomposite composed of 96 vol.% Al and 4 vol.% Al_2O_3 powder. The synthesis and characterisation of ball-milled powder is the first contribution of this study, which also investigates the influence of milling and pause duration on the fabrication of ball-milled composite powder. The second contribution of this work is the development of a 3D finite element model to predict the thermal behaviour of the first layer's composite powder. Both the transient temperature distribution and molten pool dimensions are predicted within the laser scanning, which

enables a more efficient selection of the process parameters (e.g. hatch spacing and scanning speed).

The third contribution of this study is the optimisation of the SLM process parameters and microstructure investigation of the fabricated samples. The optimum laser energy density and scanning speed that are used to fabricate nearly full dense Al-Al_2O_3 nanocomposites are found to be 317.5 J/mm^3 and 300 mm/s, respectively. The relative density is evaluated by quantifying the porosity on both the horizontal and vertical sections. The fabricated composite parts were observed to exhibit a very fine granular-dendrite microstructure due to the rapid cooling, while the thermal gradient at the molten pool region along the building direction was found to facilitate the formation of columnar grains.

The final contribution of this study is the investigation of mechanical properties such as tensile strength, microhardness and macro and nanoscale wear behaviour. Compared to pure Al, the addition of 4 vol.% Al_2O_3 nanoparticulates was found to contribute to a 36.3% and 17.5% increase in the yield strength and microhardness of the composite samples, respectively. Cold working was found to contribute to a 39% increase in microhardness due to grain deformation. The pin-on-disc wear testing and atomic force microscopy (AFM) nanoscratching were performed to study the macro and nanoscale wear behaviour of the fabricated samples, respectively.

Table of Contents

List of Figures

List of Tables

List of Abbreviations

3D	Three-dimensional
AFM	Atomic force microscopy
AM	Additive manufacturing
AMCs	Aluminium-based metal matrix composites
ASTM	American society for testing and materials
BPR	Ball to powder wright ratio
CI	Carr index
CNC	Computer numerical control
DED	Direct energy deposition
DMLS	Direct metal laser sintering
EBM	Electron beam melting
EDS	Energy dispersive X-ray spectroscopy
FDM	Fusion deposition modelling
FEA	Finite element analysis
FWHM	Full width at half maximum
HAZ	Heat affected zone
HEBM	High-energy ball-milling
ISO	International organisation for standardisation
LENS	Laser engineering net shaping
LOM	Laminated object manufacturing
MEMS	Micro-electromechanical systems

OM	Optical microscopy
PCA	Process control agent
PSD	Position sensitive detector
SEM	Scanning electron microscopy
SLM	Selective laser melting
SLS	Selective laser sintering
TEM	Transmission electron microscopy
UAM	Ultrasonic additive manufacturing
UTS	Ultimate tensile strength
UV	Ultraviolet
XRD	X-ray powder diffraction

Nomenclature

A	absorptivity
A'	Adhesive force
$c(T)$	Specific heat
d	Powder bed thickness
d'	Average grain size
f	Friction force
H	Heat transfer coefficient
h	Hatch spacing
H'	Enthalpy
H''	Absorbed laser energy
$I(r)$	Heat flux
k_b	Thermal conductivity of bulk material
k_p	Thermal conductivity of powder bed
L	Sliding distance
l	Track length
l_p	Point distance
M	Voltage-output difference between the scratching and nonscratching
M_d	Measured frictional signal under the downhill motion

M_u	Measured frictional signal under the uphill motion
N	Normal load
n	Number of tracks
P	Laser power
P_r	Recoil pressure
r	Radial distance from the laser centre
r_0	Laser spot radius
T_o	Substrate temperature
T_a	Ambient temperature
T_b	Material boiling point
T_s	Powder bed surface temperature
t	Scanning time
t_e	Laser exposure time
v	Laser scanning speed
v_l	Laser moving speed between two adjacent points, 5,000 mm/s
V_A	Apparent volume
V_T	Tapped volume
V_Δ	Volume loss of specimen
W_1	Weight of Al
W_2	Weight of Al_2O_3
W_i	Weight of input
W_o	Weight of output

W_{Δ}	Weight loss
ρ_b	Density of bulk material
ρ_p	Density of powder
Δ_{flat}	Friction-loop offset of the flat
Δ_{slope}	Friction-loop offset of the slope
$\Delta T(z,t)$	Temperature increase along z direction
α	Conversion factor between lateral force and lateral signal
α'	Thermal diffusivity
ε	Laser energy density
β	Full width at half maximum
θ	Slope angle of the calibration grating
θ'	Bragg angle
φ	yield
φ'	powder bed porosity
λ	Wavelength of the X-radiation
γ	Surface tension
γ_i	Volume percentage of component i
ω	Wear rate
μ	Friction coefficient

List of Publications

Journal Publications

[1] Quanquan Han, Yanquan Geng, Rossitza Setchi, Franck Lacan, Dongdong Gu and Sam L. Evans. "Macro and nanoscale wear behaviour of Al-Al_2O_3 nanocomposites fabricated by selective laser melting." *Composites Part B: Engineering* 127 (2017): 26-35.

[2] Quanquan Han, Rossitza Setchi, Franck Lacan, Dongdong Gu and Sam L. Evans. "Selective laser melting of advanced Al-Al_2O_3 nanocomposites: Simulation, microstructure and mechanical properties." *Materials Science and Engineering A* 698 (2017): 162-173.

[3] Quanquan Han, Rossitza Setchi, and Sam L. Evans. "Characterisation and milling time optimisation of nanocrystalline aluminium powder for selective laser melting." *The International Journal of Advanced Manufacturing Technology* 88 (2017): 1429-1438.

[4] Quanquan Han, Rossitza Setchi, and Sam L. Evans. "Synthesis and characterisation of advanced ball-milled Al-Al_2O_3 nanocomposites for selective laser melting." *Powder Technology* 297 (2016): 183-192.

Conference Publications

[1] Quanquan Han, Rossitza Setchi, Sam L. Evans and Chunlei Qiu. “Three-dimensional finite element thermal analysis in selective laser melting of Al-Al2O3 powder.” Presented at: *The 27th Annual International Solid Freeform Fabrication Symposium - An Additive Manufacturing Conference*, Austin, Texas, USA, 8-10 August 2016.

[2] Quanquan Han, Rossitza Setchi and Bhushan L. Karihaloo. “Challenges and opportunities in the additive layer manufacturing of Al-Al2O3 nanocomposites.” Presented at: *SDM'2015 International Conference on Sustainable Design and Manufacturing*, Seville, Spain, 12-14 April 2015.

Chapter I

Introduction

1.1 Research Motivation

Aluminium has been widely used in aerospace and automotive industries due to its light weight, high specific strength and excellent corrosion resistance. However, compared to pure aluminium and various unreinforced aluminium alloys, aluminium-based metal matrix composites (AMCs) provide better mechanical and physical properties, including greater strength, improved high temperature properties, wear resistance and a controlled thermal expansion coefficient (Srivatsan et al. 1991; Lloyd 1994; Surappa 2003). Over the past few years, these attributes have found broad application in several demanding fields like the automotive, aerospace, defence, sports, electronics and biomedical industries, as well as for other industrial purposes (Koli et al. 2013). For instance, in the automotive industry, AMCs are typically used to fabricate pistons, cylinders, brakes and power transfer system elements.

A wide range of reinforcement particulates such as Al_2O_3, SiC, B_4C, TiC and TiO_2 have been used in AMCs (Mazahery et al. 2009), however, compared to other reinforcements, nanoscale Al_2O_3 particulates are capable of improving both their wear behaviour and high temperature properties without introducing any undesirable phases and are therefore widely used in AMCs (Durai et al.

2007). Studies have shown that the strength of Al-Al_2O_3 nanocomposites increases with the volume fraction of nano Al_2O_3; however, the strengthening effect is found to level off when the volume fraction is above 4 vol.%, which is attributed to the clustering of nano Al_2O_3 particulates (Kang and Chan 2004; Poirier et al. 2010).

The application of Al-Al_2O_3 composites has been limited to a few very specific areas due to their high processing costs and the lack of a feasible fabrication method (Zebarjad and Sajjadi 2007). On the other hand, since the first technique for additive manufacturing (AM) became available in the late 1980s and was used to fabricate models and prototypes, AM process has experienced more than 30 years' development and is acted as one of the rapidly developing advanced manufacturing techniques in the world (Gibson et al. 2010). In comparison with conventional manufacturing technologies, which generally adopt materials removal principle, AM employs the layer-by-layer manufacturing principle to build parts.

Amongst current AM processes, Selective laser melting (SLM) is widely used to manufacture 3D complex-shaped metallic parts (Gu et al. 2012; Read et al. 2015). Therefore, the SLM of Al-Al_2O_3 nanocomposites is expected to show great potential in the fabrication of advanced engineering components to meet the demanding requirements of the aerospace and automotive domains. The research problems of this study include the synthesis of an advanced Al-Al_2O_3 nanocomposite suitable for SLM and the fabrication of nearly full dense parts using SLM.

1.2 Research Aim and Objectives

The overall aim of this study is to employ SLM to fabricate an advanced Al-Al_2O_3 composite. The advanced nanocomposite powder suitable for SLM needs to be synthesised prior to the SLM; finite element thermal simulation should be conducted to provide a more efficient selection of process parameters within SLM. The optimum process parameters within SLM should be employed to fabricate nearly full dense parts to investigate the microstructure and mechanical properties of the composite samples. Therefore, the individual objectives towards achieving this aim include:

i. To investigate high-energy ball-milling of Al-Al_2O_3 powder in order to synthesise an advanced nanocomposite suitable for SLM.
ii. To develop a computational model in order to simulate the laser-material interaction. The predicted thermal information is expected to enable a more efficient selection of process parameters in fabricating bulk samples.
iii. To study the SLM process parameters in order to use the optimum combination to fabricate full-dense parts and investigate the microstructure of the fabricated samples. The optimum process parameters (e.g. laser energy density, scanning speed) are determined by quantifying the relative density of the as-fabricated samples.
iv. To investigate the mechanical properties (i.e. tensile strength, microhardness and macro and nanoscale wear behaviour) of the fabricated samples in order to explore the influences of Al_2O_3

reinforcement and microstructure change on mechanical properties alteration.

1.3 Research Methodology

The following research methodology is employed in order to achieve the above aim and objectives:

- The synthesis of an advanced Al-4 vol. % Al_2O_3 composite powder suitable for SLM is the first objective of this study and can be achieved by employing high-energy ball-milling (HEBM) process because, HEBM is a simple and effective technique to refine particle grain size and disperse reinforcement materials homogeneously in a metal matrix. Another advantage of HEBM lies in its ability to produce bulk quantities of solid-state materials using simple equipment at room temperature. The ball-milled powder samples are taken out every 4h for analysis (e.g. particle size, morphology and flowability) in order to determine the optimum milling time. Systematic analytical techniques used to analyse the samples include x-ray powder diffraction (XRD), scanning electron microscopy (SEM), transmission electron microscopy (TEM) and energy dispersive X-ray spectroscopy (EDS). The optimum milling time is employed to produce bulk composite powder for SLM.
- In order to provide a more efficient selection of process parameters used in SLM of bulk samples, a thermal simulation is conducted prior to the SLM experiments. A 3D finite element model is developed in the ANSYS

Multiphysics package platform to predict the thermal behaviour of the first layer's composite powder. Furthermore, in order to reduce the computational time, the first layer consists of three single tracks; both the transient temperature distribution and molten pool dimensions are predicted in the thermal simulation. The simulation results are also compared with the SLM fabricated single tracks and single layer in order to validate the simulation.

- A Renishaw AM250 SLM system is employed in this study to achieve the process parameters optimisation to fabricate the nearly full dense parts. Thus, the as-fabricated cubic samples (8x8x8 mm) under different conditions are both horizontally and vertically sectioned and then polished. The laser energy density and scanning speed are optimised by quantifying the relative density of the polished samples using ImageJ software. Due to the rapid cooling, the fine granular-dendrite microstructure is expected to be formed and further influence the mechanical properties of the fabricated samples. The polished sample surface is etched using Keller's reagent for 30s in order to reveal the microstructure prior to the microstructure inspection using optical microscopy (OM) and SEM.
- In order to explore the influences of Al_2O_3 reinforcement and microstructure change on mechanical properties alteration, the tensile strength, microhardness and wear behaviour of the fabricated samples are investigated. The tensile and microhardness tests are performed using a Zwick/Roell tester with a strain rate of 0.3 mm/min and Innovatest

with a 100g load and 10s dwell time, respectively. Pin-on-disc wear tests and atomic force microscopy (AFM) tip-based nanoscratching are conducted to investigate the macro and nano-scale friction and wear behaviour of the fabricated samples.

1.4 Organisation of the Thesis

This thesis is organised as follows:

Chapter 1 introduces the study by highlighting the research motivation, aim and objectives as well as the methodology of the research.

Chapter 2 reviews the related literature within the scope of this study. It briefly reviews the typical process parameters and defects within SLM followed by the aluminium matrix composites and HEBM process. After that, it discusses the application of finite element analysis in SLM and provides a discussion on AFM tip-based nanoscratching in nanoscale friction and wear investigation. The application of AFM in the study of nanoscale friction and wear is discussed afterwards. This chapter also provides a discussion on the challenges and opportunities in SLM of aluminium.

Chapter 3 addresses the first objective; it focuses on the synthesis and characterisation of an advanced Al-4 vol.% Al_2O_3 nanocomposite powder suitable for SLM.

Chapter 4 addresses the second objective; it focuses on the study of finite element simulation of SLM first layer's composite and outlines the 3D finite

element model that is developed to predict the thermal behaviour, including transient temperature distribution and molten pool dimensions.

Chapter 5 addresses the third objective; it focuses on the optimisation of SLM process parameters (e.g. laser energy density and scanning speed) and analysis of microstructure of the fabricated samples.

Chapter 6 addresses the last objective; it focuses on the investigation of mechanical properties of the fabricated samples in order to explore the influences of Al_2O_3 reinforcement and microstructure change on mechanical properties alteration. Typical mechanical properties that are studied include tensile strength, microhardness and macro and nanoscale wear behaviour.

Chapter 7 highlights the contributions and conclusions of this study, and outlines future work.

Chapter II

Literature Review

This chapter reviews related work that provides key ideas that are applicable to achieving those objectives that are defined in chapter 1. This chapter thus is organised as follows: Section 2.1 reviews the SLM with a focus on typical process parameters and defects that are formed within SLM. Section 2.2 and 2.3 discuss advanced aluminium matrix composites and the HEBM process employed to produce them. Section 2.4 discusses the finite element simulation used in selective laser melting. Section 2.5 discusses the application of atomic force microscopy in studying nanoscale friction and wear behaviour. Section 2.6 discusses the challenges and opportunities in selective laser melting of Al-Al_2O_3 nanocomposites, while Section 2.7 provides a summary of the chapter.

2.1 Selective Laser Melting

Compared to other metal-based AM processes (e.g. electron beam melting), SLM is widely used to manufacture metallic components by employing a high power-density laser. SLM is an integrated process that involves materials, manufacturing and physics and thus, the working efficiency and quality of the fabricated parts are greatly influenced by a wide range of process parameters.

2.1.1 Typical Process Parameters Used in SLM

In this subsection, the four typical process parameters used in SLM are discussed in detail. They are laser power, scanning speed, hatch spacing and powder layer thickness. It should be noted that those parameters are strongly interdependent.

i. Laser power. Figure 2.1 shows the schematic illustration of SLM; a substrate for part creation is fixed on the building platform and levelled in the chamber. The laser beam scans the powder bed to create the first cross-sectional profile according to the CAD data of the component to be produced. Laser power is crucial because it determines the input energy density when the laser scans powder layer. During the laser-material interaction, a higher laser power generally results in more energy input to fully melt the deposited powder. Kempen et al. (2011) studied the influence of laser power on SLM of AlSi10Mg alloys and found that the relative density increased from 98.5% to 99.3% when the laser power increased from 170 W to 200 W. High power lasers are finding more applications in processing metal based composites and materials with high reflectivity (e.g. aluminium) (Buchbinder et al. 2008).

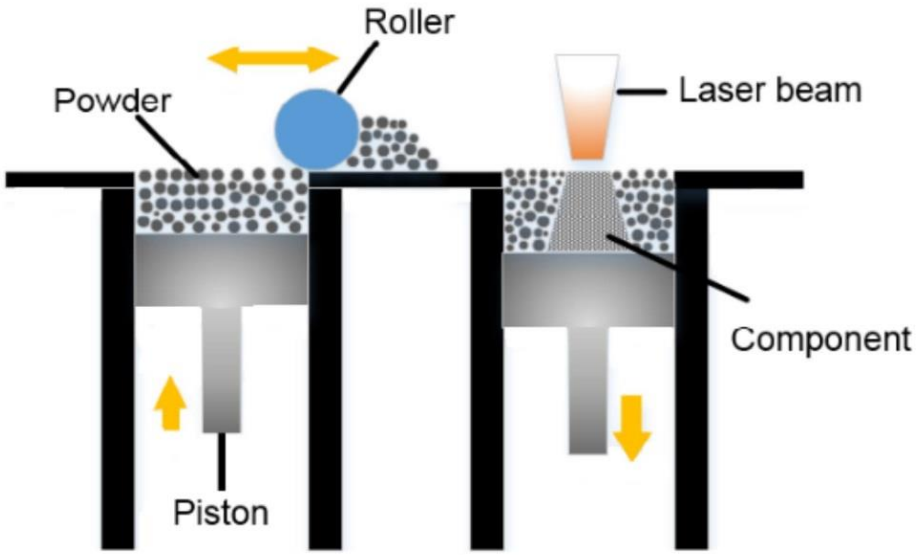

Figure 2.1: Schematic illustration of SLM.

ii. Scanning speed. Previous studies have shown that scanning speed could determine the microstructure and mechanical properties of the fabricated components by changing the stability of molten pool (Gu et al. 2012). Yadroitsev et al. (2007) investigated the influence of scanning speed (0.06-0.24 m/s) on single tracks of the first layer of stainless steel grade 904L, it was found that with an increase in the scanning speed while maintaining the laser power of 50 W, the track width and zone of powder consolidation decreased.

iii. Hatch spacing. Hatch spacing is important because, it could influence the laser energy density and further determine the overlap area between two adjacent tracks. Thijs et al. (2010) investigated the influence of hatch spacing (50, 75 and 100 µm) on the properties of SLM manufactured bulk Ti-6Al-4V samples; it was found that the formed molten pool width was approximately 100 µm under the optimised parameters (42 W, 200 mm/s

and 75 µm), and neighbouring scanning tracks hardly touched each other when a hatch spacing of 100 µm was used. When a hatch spacing of 50 µm was employed, however, the tracks overlapped 50% indicating that the molten pool width was not influenced significantly by a lowering in hatch spacing. Yadroitsev et al. (2007) studied the influence of hatch spacing on porosity of Inconel 625 alloy manufacturing by SLM; it was found that the porosity decreased with an increase in the hatch spacing from 60 to 100 µm. A further increase of the hatch spacing, however, resulted in a strong increase in porosity.

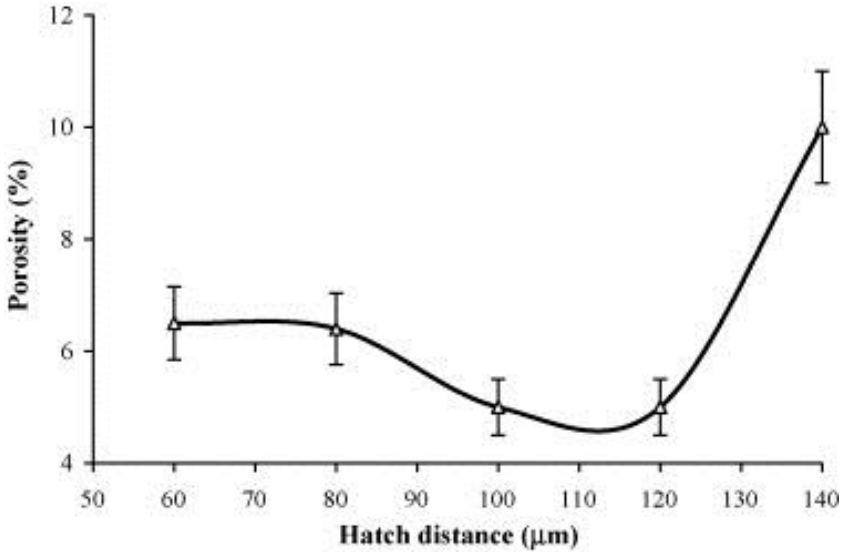

Figure 2.2: Samples porosity with hatch spacing (powder layer thickness 50 µm, laser power 50 W, scanning speed 0.13 m/s) (Yadroitsev et al. 2007).

iv. Powder layer thickness. As SLM is a layer-by-layer manufacturing process, the powder layer thickness is one of the determinant factors of this process. The appropriate selection of the layer thickness should be based on both the particle size and the shrinkage extent. Small layer

thickness enables to achieve good accuracy but does not favour productivity of the manufacturing process. Vandenbroucke and Kruth (2007) investigated the influence of layer thickness on top surface roughness (Ra) of SLM fabricated titanium alloy; it was found that the roughness increased from 8 to 20 μm with an increase in layer thickness from 20 to 50 μm. The top surface roughness improved strongly for smaller layer thickness because, higher thermal conductivity and the presence of less powder led to smaller and more stable molten pools.

The typical process parameters used in SLM need to be optimised in order to manufacture full-dense components, otherwise it may result in the formation of defects during the SLM. The defects within SLM are discussed in next subsection.

2.1.2 Defects in SLM

Typical defects that are formed within SLM include balling, porosity and cracking.

i. Balling. The term ‘balling’ refers to the formation of a large ball of molten material, with a fraction of this ball incorporated in the solidified layer. Li et al. (2012) investigated the balling behaviour of stainless steel and nickel powder during SLM and found that the SLM balling phenomenon can be divided into two types: ellipsoidal balls with dimension of about 500 μm and spherical balls with dimension of about 10 μm.

The formation of balling is thought to be strongly dependent on scanning speed and laser power. Yadroitsev et al. (2012) investigated the SLM of stainless steel and found that balling could occur at high speeds when using relatively high laser power (50 W) (Yadroitsev et al. 2010). Kruth et al. (2014) investigated the selective laser melting of iron-based powder and found that high scanning speeds combined with high laser powers resulted in less balling. This was because the molten pool rapidly solidified behind the laser spot when the length of the molten track was short. Aboulkhair et al. (2016) found that balling formed on top of the AlSi10Mg layer when the scanning speed was up to 750 mm/s while maintaining the laser power of 100 W; Figure 2.3 shows the formed balling defects on the surface of SLM fabricated AlSi10Mg layers.

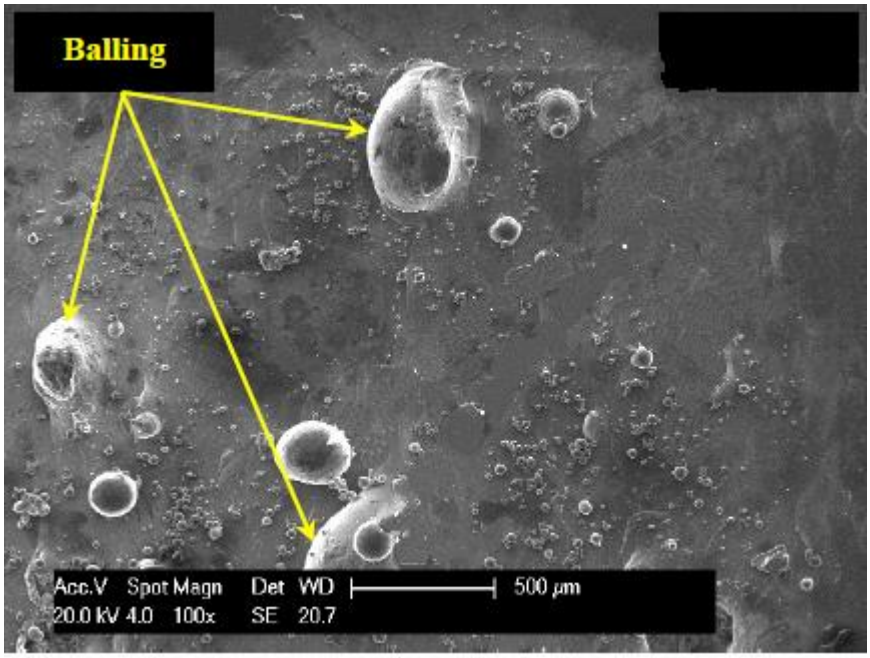

Figure 2.3: Balling formed on AlSi10Mg layers (Aboulkhair et al. 2016).

ii. Porosity. Porosity refers to the fraction of pores or voids formed within the samples; it is generally considered to be the primary defect of SLM-fabricated parts. Pores may be categorised as either metallurgical pores or keyhole pores (Aboulkhair et al. 2014; Haboudou et al. 2003). Metallurgical pores are spherically shaped and small in size; they are created from gases trapped within the molten pool or evolved from the powder during consolidation, which suggests that metallurgical-pore level is determined by the powder morphology and powder bed. Keyhole pores, in contrast, are irregularly shaped and large in size; they are attributable to the rapid solidification of the metal without the complete filling of gaps (with molten metal in particular) at relatively high scanning speeds.

Pores that are induced by oxidation may be classified as keyhole pores, since non-melted or partially melted powders can become trapped when two thin oxide films meet. Another significant factor in the formation of keyhole pores is the interaction of recoil pressure and Marangoni convection within the molten pool (Khairallah et al. 2016). This mechanism is thought to be the dominating factor when relatively high laser power and low scanning speeds are employed in processing certain metal powders (e.g. aluminium and its alloys).

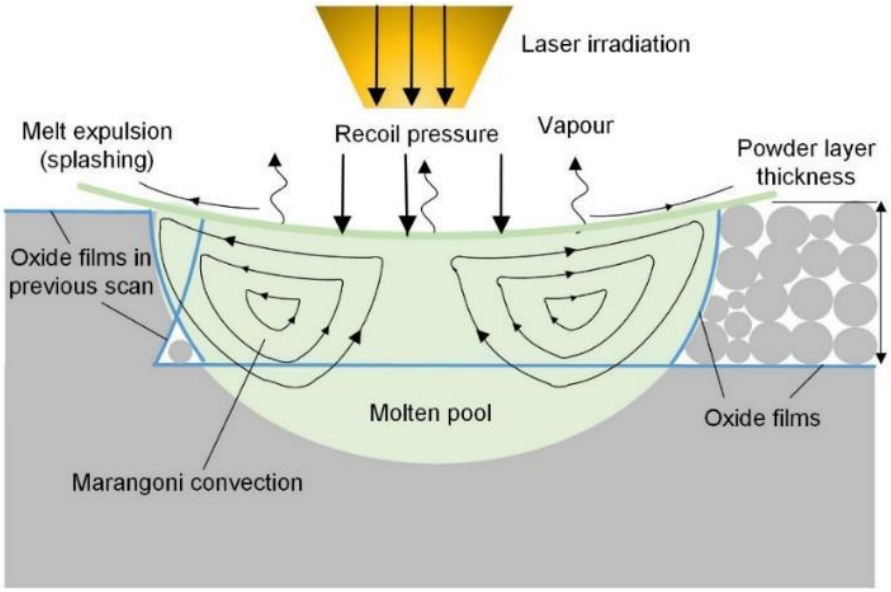

Figure 2.4: Schematic diagram of laser-material interaction within selective laser melting (SLM)

Figure 2.4 shows the laser-material interaction within the molten pool. Due to the local difference of the surface tension induced by the temperature gradient, the liquid in the molten pool flows from the high-temperature regions to the relatively cool region. It has been found that increasing the laser power and reducing the spot size both make Marangoni convection stronger and move the centres of the cells closer to the pool edge (Limmaneevichitr and Kou 2000). When the temperature on the surface becomes greater than the material's boiling point, strong vaporisation occurs, and the induced recoil pressure, together with the Marangoni convection, causes a change in the molten pool shape and subsequent splashing.

The collapse of the vapour cavity that is produced by the recoil pressure also results in the formation of keyhole pores; this process can be completed within 5 μs (Khairallah et al. 2016). The recoil pressure (P_r) is determined by the strong vaporisation, which may be expressed as (Anisimov and Khokhlov 1995):

$$P_r = 0.54 P_a \exp\left(\frac{\lambda}{k_B}\left(\frac{1}{T_b} - \frac{1}{T}\right)\right) \quad (2.1)$$

where P_a =1 bar is the ambient pressure, λ = 3.225 ev/atom is the vaporisation energy per Al atom, k_B= 8.617x10^{-5} ev/K is the Boltzmann constant, T is the surface temperature and T_b is the boiling point of the material. The T_b for Al and Al_2O_3 is 2,743 K and 3,250 K, respectively. In order to push the molten material out of the cavity, the recoil pressure should be greater than the pressure produced by the surface tension, $P_r > \frac{\gamma}{2r_0}$, where γ is the surface tension at the boiling point and r_0 is the laser-spot radius. King et al. (2014) have determined that, for a laser-spot size of tens of micrometres, the ejection of the molten material is independent of the spot size. The condition $T = T_b$ can thus be considered to be the threshold for the generation of recoil pressure; the temperature (T) that is reached in relation to exposure time (t) can be expressed as:

$$T = T_0 + \Delta T(z, t) \quad (2.2)$$

where T_0 and $\Delta T(z,t)$ denote (respectively) the preheated temperature and the temperature increase along the z direction with time. The temperature increase can be expressed as (Dahotre and Harimakar 2008)：

$$\Delta T(z,t) = \frac{H''}{k}\left(4\alpha' t\right)^{1/2} f\left(\frac{z}{\left(4\alpha' t\right)^{1/2}}\right) \tag{2.3}$$

where the function $f(x)$ is defined as:

$$f(x) = \frac{1}{\sqrt{\pi}}\{\exp(-x^2) - x(1-g(x))\} \tag{2.4}$$

and:

$$g(x) = \frac{2}{\sqrt{\pi}}\int_0^x e^{-\xi^2} d\xi \tag{2.5}$$

where H'' denotes the absorbed laser energy and α' is the thermal diffusivity. The latter is shown by $\alpha' = {}^{k}/_{\rho c}$, where k is the thermal conductivity of the powder bed, and c and ρ denote the specific heat and powder density, respectively. The temperature increase at the surface under laser irradiation can thus be obtained by substituting $z = 0$ and $H'' = \frac{2AP}{\pi {r_0}^2}$ in equation (2.3), which produces:

$$\Delta T(0,t) = \frac{4\sqrt{t}AP}{\pi^{\frac{3}{2}} {r_0}^2 \sqrt{\rho c k}} \tag{2.6}$$

where A and P denote the absorptivity and employed laser power, respectively. The maximum surface temperature T that is reached under specific exposure times can thus be determined.

Several recent studies have reported porosity minimisation strategies for selective laser melting process. For instance, Aboulkhair et al. (2014) investigated the windows of parameters required to produce high density AlSi10Mg parts using selective laser melting; their study found that the type of pore formed during SLM was related to the employed scanning speeds, metallurgical pores tended to be formed at lower speeds whereas keyhole pores were created with increasing scanning speeds, along with a reduction in metallurgical. Sun et al. (2016) employed SLM process to successfully fabricate high density (>99%) 316L stainless steel parts with high build rates; it was recommended to find out a suitable power energy density for a material and then adjust the scanning strategy or scanning parameters.

iii. Cracking. The process of selective laser melting gives rise to large thermal gradients during the rapid melting of metallic powders; thermal induced cracking may be formed in certain alloys during the solidification, which cannot be eliminated via process optimisation (Harrison et al. 2015). Mercelis and Kruth (2006) found that the generation of cracking within SLM may be attributed to two mechanisms: thermal gradient mechanism and the cool-down phase of molten top layers.

In the thermal gradient mechanism, the rapid heating of the top surface combined with the relatively low thermal conductivity of the powder, created a steep temperature gradient (Mercelis and Kruth 2006). The rapid cooling resulted in a shrinkage of the upper layer, inducing a bending angle towards the laser source and in turn generating a tensile

stress in the building direction. When the tensile stress exceeds the ultimate tensile strength (UTS) of the solid material, the solid phase could fracture and result in cracking. Figure 2.5 shows the formed micro-cracks within SLM fabricated nickel superalloys.

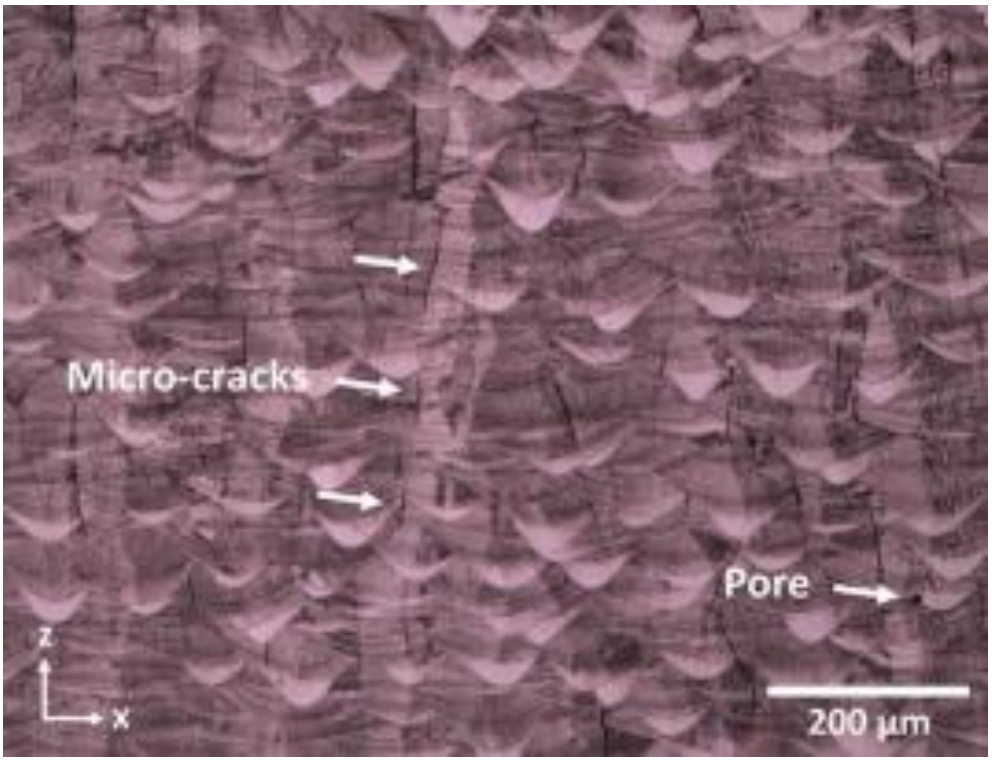

Figure 2.5: Optical micrograph showing the cracks in SLM fabricated nickel superalloys (Harrison et al. 2015).

2.2 Aluminium-based Metal Matrix Composites

The most commonly used reinforcements in aluminium-based metal matrix composites (AMCs) are SiC and Al_2O_3 (Ramnath et al. 2014); they both increase the tensile strength, hardness, density and wear resistance of AMCs. The particle

distribution of the reinforcements plays a significant role in the properties alteration of AMCs (Murty et al. 2003).

Early studies reported the mechanical properties of SiC reinforced AMCs. For instance, Ozden et al. (2007) investigated the impact behaviour of extruded SiC reinforced AMCs under different temperatures; it was found that the impact behaviour of composites was affected by clustering of particles, particle cracking and weak matrix-reinforcement bonding. The effect of the test temperature on the impact behaviour of all composites, however, were not very significant. Natarajan et al. (2006) compared the wear behaviour of SiC reinforced AMCs with the conventional grey cast iron sliding against automobile friction material. It was found that the wear resistance of the composite was higher than the conventional grey cast iron and it thereby was a very suitable material for brake drum.

Compared to SiC reinforcement, Al_2O_3 exhibits better thermal stability at high temperatures as undesirable phases are not produced in such materials (Durai et al. 2007; Rahimian et al. 2009). Rahimian et al. (2009) studied the effect of particle size, sintering temperature and sintering time on the properties of Al-Al_2O_3 composites, made by powder metallurgy. In their study, the average particle sizes of Al_2O_3 were 3, 12 and 48μm, and the weight percentage of Al_2O_3 was fixed at 10 wt. %; the Al particle size was 30 μm with a purity of 99.97%. The effect of Al_2O_3 particle size on the mechanical properties of the composites is shown in Table 2.1.

Table 2.1: Influence of Al_2O_3 particle size on mechanical properties (Rahimian et al. 2009).

Al_2O_3 size (μm)	**Relative density (%)**	**Hardness (HB)**	**Yield strength (MPa)**	**Elongation (%)**
Pure Al	99.23	31	93	50
3	97.41	65	210	46
12	98.2	58	180	26
48	96.71	53	140	18

It was found that finer Al_2O_3 particles reinforced AMCs exhibited higher hardness and yield strength and this could be contributed to the larger interfacial area between the strengthening phase and the Al matrix. Furthermore, the elongation of the composite samples increased with a reduction in the Al_2O_3 particle size. Kumar et al. (2013) investigated the characterisation of Al-Al_2O_3 AMCs using electromagnetic stir casting method; they found that the hardness and tensile strength increased and electromagnetic stirring action produced AMCs with smaller grain size and good reinforcement-matrix interface bonding. Several studies focused on the mechanical properties of AMCs reinforced with nanoscale Al_2O_3; it was shown that the strength of Al-Al_2O_3 nanocomposites increases with the volume fraction of nano Al_2O_3; however, the strengthening effect is found to level off when the volume fraction is above 4 vol.%, which is attributed to the clustering of nano Al_2O_3 particles (Kang and Chan 2004; Poirier et al. 2010).

Nonetheless, due to the significant surface energy of the nano particles, the dispersion of nano Al_2O_3 reinforcement amongst Al matrix has always been a challenge for researchers and practitioners. The next section discusses an

effective method that is used to synthesise the nanocomposite and disperse the nano Al_2O_3 reinforcement uniformly amongst Al matrix.

2.3 High-Energy Ball-Milling

High-energy ball-milling (also known as mechanical milling) is a simple and effective technique to refine particle grain size (~100 nm) and disperse reinforcement materials homogeneously in a metal matrix (Khan et al. 2008; Liao and Tan 2011). Another advantage of high-energy ball-milling (HEBM) lies in its ability to produce bulk quantities of solid-state materials using simple equipment at room temperature.

2.3.1 Operating Principle

The most commonly used ball mill for synthesising AMCs is planetary ball mill, which is generally equipped with 2 or 4 grinding bowls; the operating principle is shown in Figure 2.6.

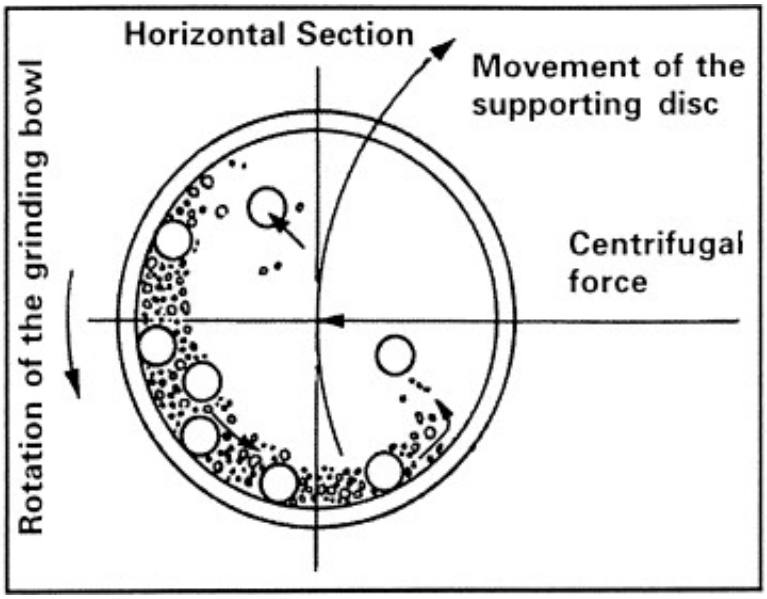

Figure 2.6: Schematic diagram of planetary ball mill (Suryanarayana 2001).

The grinding bowls are arranged on a rotating supporting disc and a special drive mechanism causes them to rotate around their own axes. The centrifugal forces from the rotation of the grinding bowls around their own axes and from the rotating supporting disc on the contents of the grinding contents which consists of materials to be ground and grinding balls. Since the grinding bowls and the supporting disc rotate in opposite directions, the centrifugal forces alternately act in the same direction and opposite directions. This results in the grinding balls to run down the inside wall of the bowl–the friction effect, followed by the material being ground and grinding balls hitting the opposite wall of the grinding bowl as impact effect. The impact effect is amplified by the impact of the grinding balls against each other (Suryanarayana 2001; Zhang 2004).

Due to the intensive impact of grinding balls and bowls, the particle size of the materials is refined and the reinforcement is dispersed uniformly. Several

process parameters used in HEBM could affect the properties of the ball-milled powder, and the next subsection discusses the typical process parameters in HEBM.

2.3.2 Process Parameters in HEBM

HEBM process is a complex process and hence involves a number of parameters, but not all of them are completely independent. Typical process parameters include milling speed, milling time, grinding medium, ball-to-powder weight ratio, milling atmosphere and process control agent. A proper selection of those parameters could improve the milling efficiency and reduce the contamination during HEBM.

i. Milling speed. It is easy to realize that the faster the mill rotates the higher would be the energy input into the powder. However, above a critical speed, the balls will be pinned to the inner walls of the bowl and cannot drop to exert any impact force. Moreover, a super high speed may result in a high temperature of the bowl. This may result in a decomposition of metastable phases formed during the milling.

ii. Milling time. This is the most important parameter. Normally, the milling time depends on some other parameters to achieve a steady state. But it should be noted that the level of contamination increases and some undesirable phases may form if the milling time is longer than required.

iii. Grinding medium. Hardened steel, tool steel, tempered steel, WC-Co and stainless steel are the most common types of materials used for the grinding medium. The density of the grinding medium should be high

enough so that the balls can create enough impact force on the powder. Moreover, it would be desirable to have the grinding bowls and the grinding medium made of the same material in order to avoid cross contamination.

The size of the grinding medium also has an influence on the milling efficiency. It has been found that the highest collision energy can be obtained if balls with different diameters are used. In the initial stage of milling, the powder being milled gets coated onto the surface of the balls and also gets cold welded. The advantage is that it prevents excessive wear and avoids contamination of the powder; the disadvantage however is that, it is difficult to detach the powder and so the yield is low. It is possible that the different sized balls produce shearing forces that help to detach the powder from the surface of the balls.

iv. Ball-to-powder weight ratio (BPR). In general, the higher the BPR, the shorter the time required is. A ratio of 10:1 is most commonly used in milling a small quantity of powders.

v. Milling atmosphere. The main effect of the milling atmosphere is on the contamination of the powder. The presence of air in the grinding bowls could give rise to the formation of oxides and nitrides in the powder. High purity argon thus is most commonly used to prevent oxidation and contamination of the powders.

vi. Process control agent (PCA). The refinement among powder particles can occur only when a balance is maintained between cold welding and fracturing of particles. A process control agent is added in order to reduce

the effect of cold welding because, the PCA is absorbed on the surface of the particles which prevents excessive cold welding and further stops agglomeration. A wide range of PCAs have been used in practice at a level of about 1-5 wt% of the total powder weight. The most commonly used PCAs include stearic acid, hexane, methanol and ethanol. In particular, stearic acid has been widely used in HEBM of aluminium powders (Suryanarayana 2001).

2.3.3 HEBM of Al-Al_2O_3 Composites

The main challenges in HEBM of Al-Al_2O_3 composites lie in: (1) enabling the uniform distribution of the Al_2O_3 reinforcement in Al matrix and (2) enabling no excessive cold working.

Several studies reported the synthesis and characterisation of the ball-milled Al-Al_2O_3 composites. For instance, Prabhu et al. (2006) employed a SPEX mill to synthesize Al-Al_2O_3 composite powders with volume fraction of 20% and found that the Al_2O_3 reinforcement (5 μm in diameter) were distributed homogeneously in the Al matrix after 20 hours of milling at a BPR of 10:1. Zebarjad and Sajjadi (2007) investigated the physical and mechanical properties of the Al-Al_2O_3 composites produced by the HEBM method and found that the milling time had a significant effect on the mechanical and physical properties of the composites; however, increasing the milling time was shown to have no significant effect on the properties when the steady state was achieved. Another study of the effect of milling on composite microstructures found that at the

beginning of the process the powders tended to absorb iron, and the trend gradually decreased until the steady state. Moreover, the increase of milling time contributed to the formation of fine Al_2O_3 particulates and their uniform distribution performance (Zebarjad and Sajjadi 2006).

More recently, Khorshid et al. (2010) investigated the mechanical properties of aluminium matrix composites reinforced by two sizes of Al_2O_3 particles (35 nm and 0.3 μm) by wet attrition milling, and found that the hardness and yield strength improved with the increased amount of Al_2O_3; nonetheless, when the fraction exceeded 4 wt.%, both the hardness and strength decreased. Poirier et al. (2010) studied the mechanical properties of ball-milled Al-Al_2O_3 nanocomposites and established that the hardness of the composites was five times higher than pure unmilled Al; a decrease in the Al_2O_3 particle size from 400 nm to 4 nm gave rise to an increase of 11% in the hardness of the composites. Su et al. (2012) investigated the processing, microstructure and tensile properties of Al-Al_2O_3 nano composites by ball milling and ultrasonic treatment. They determined that, compared to an aluminium alloy, the ultimate tensile strength and yield strength of the Al-1 wt.% Al_2O_3 composite increased by 37% and 81%, respectively; this can be explained by the grain refinement and homogeneous dispersion of the nano reinforcements.

The aforementioned studies successfully applied high-energy ball-milling in the fabrication of Al-Al_2O_3 composites. However, the flowability of the synthesised composite powder has not been studied and the synthesised composite powder has not been applied in selective laser melting.

2.4 Finite Element Analysis in SLM

Researchers have employed finite element analysis (FEA), one of the most widely used numerical methods in use today, for temperature field analysis in various AM processes. This section thereby reviews the application of FEA in SLM.

In early papers, Childs (2005) investigated the influence of process parameters on the mass of melted single layers in SLM and found that an increase in scanning speed resulted in a larger melted mass. Matsumoto et al. (2002) proposed a method for calculating the distribution of temperature and stress in the SLM of single metallic layers; they found that the solid layer on the powder bed warped due to the rapid heating and cooling while the laser scanned the track. Dai and Shaw (2002) investigated the effect of the laser scanning strategy on residual stress and distortion and found that a scanning pattern with frequent 90° changes in the scanning direction at every turn could lead to a reduction of concave upwards and downwards distortions.

More recently, Hussein et al. (2013) developed a transient finite element model for the analysis of temperature and stress fields in single layers built without support in SLM. They found that the predicted length of the molten pool increased at higher scanning speeds, while both the width and depth of the molten pool decreased. Li and Gu (2014) analysed thermal behaviour during the SLM of aluminium alloy powders and obtained the optimum molten pool width (111.4 μm) and depth (67.5 μm) for a specific combination of parameters (laser power 250 W and scanning speed 200 mm/s). Roberts et al. (2009) developed an

element birth-and-death strategy to analyse the 3D temperature field in multiple layers within a powder bed. Similar studies have explored the behaviour of other materials during SLM. For example, Kolossov et al. (2004) developed a 3D finite element model to predict the temperature distribution on the top surface of a titanium powder bed during the laser sintering process; it was found that the changes of thermal conductivity in powder bed determined the behaviour and development of thermal processes. In addition, Patil and Yadava (2007) investigated the temperature distribution in a single metallic powder layer during metal laser melting and found that temperature increased with increases in laser power and laser exposure time, but decreased with an increase in hatch spacing.

It may be concluded that the thermal behaviour within SLM can be predicted by FEA, which may facilitate a more efficient selection of process parameters during SLM of various metallic materials and further improve the productivity.

2.5 AFM Tip-based Friction and Wear

Due to its low cost and its ability to achieve atomic-level manipulation using a relatively simple system, atomic force microscopy (AFM) is widely used in various nanotechnology and nanomanufacturing applications. Due to its capability of applying extremely small forces and visualising surface topography with a resolution below 0.1 nm in vacuum condition (Cho 2009; Geng et al. 2014), AFM can thus be used to investigate nanoscale friction and wear behaviour. Another advantage of AFM is that the technique can simulate a single asperity contact

situation against a counter surface, which provides a way to investigate the friction mechanisms involved in ultra-precise components. The basic operating principle of an AFM involves scanning a specimen surface under a controlled load using a sharp tip, which is normally made of silicon, silicon nitride or a diamond coating; the sensors that are employed can then detect atomic-scale interaction forces with a nano-Newton resolution (Kim et al. 2012; Chung and Kim 2007; F. Zhang et al. 2016).

2.5.1 Wear Behaviour and SLM

For the past two decades, researchers have investigated the effects of experimental parameters such as normal load, velocity and humidity on nanoscale-friction behaviour (Kim et al. 2012; Gnecco et al. 2002). Bhushan and Kwak (2007) examined the velocity dependence of nanoscale wear when using AFM and found that the wear rate increased with the logarithm of velocity and levelled off afterwards when the velocity varied from 0.1 to 100 mm/s. Wang et al. (2015) investigated the humidity dependence of the tribochemical wearing of monocrystalline silicon and found that the tribochemical wearing's relative humidity dependence could be explained with a model involving the formation of Si-O-Si chemical bonds between two solid surfaces.

Several recent studies have reported the macroscale wear performance of SLM-fabricated parts. For instance, Kang et al. (2016) employed dry sliding to investigate the wear behaviour of hypereutectic Al-Si alloys fabricated by SLM and found that nanosize Si particles grew to become larger particles due to

extended solidification times when the laser power was greater than 210 W, which in turn resulted in poor wear resistance of the fabricated samples. Jue et al. (2017) studied the microstructure and mechanical properties of SLM-fabricated Al-based composites and found that the microstructural features and hardness of the composites were the dominating factors to determine wear performance during pin-on-disc testing. Sun et al. (2014) investigated the sliding wear characteristics of SLM 316L stainless steel and found that the wear rate of SLM steel was dependent on the porosity and by obtaining full density it was possible to achieve wear resistance similar to that of standard bulk 316L steel. The nanoscale wear behaviour of SLM-fabricated samples has yet to be reported.

2.5.2 Lateral-force Calibration

A calibration of the lateral (friction) force is generally required for accurate friction measurements when using AFM nanoscratching, because the detected signal takes the form of lateral voltage output rather than direct friction force during the nanoscratching process; a conversion factor α therefore is required, which may be obtained from the wedge calibration method, as shown in Figure 2.7.

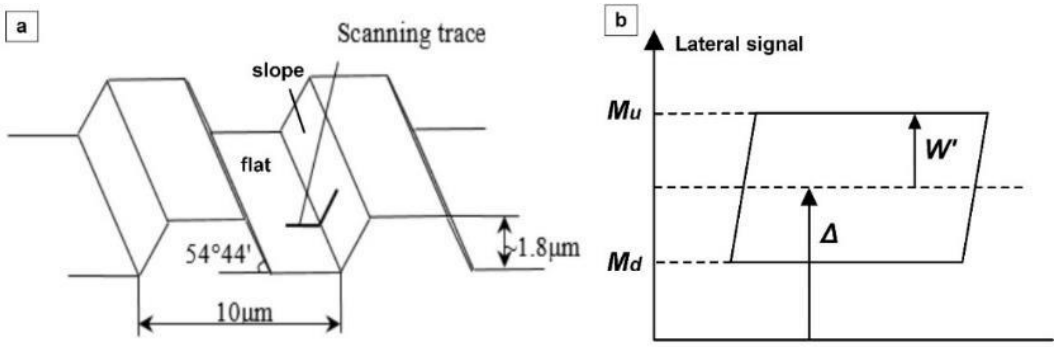

Figure 2.7: Schematic diagram of (a) TGF11 calibration grating and (b) friction loop.

A standard TGF11 silicon calibration grating can be scanned with a relatively small normal load using a diamond tip; the conversion factor between the lateral force and the lateral signal from the friction loops of a defined flat and slope can be determined by (Wang and Zhao 2007):

$$\alpha = \frac{\mu(N+A' \cos\theta)}{(\cos^2\theta - \mu^2 \sin^2\theta) W'_{slope}} \quad (2.7)$$

where N is the applied (and relatively small) normal load in the calibration; A' and θ denote the adhesive force and slope angle of the calibration grating (Figure 2.7a), respectively; and μ is the friction coefficient between the tip and the calibration grating, which can be determined by (Varenberg et al. 2003):

$$\mu^2 \sin\theta \left(N \cos\theta + A'\right) - \frac{\Delta_{slope} - \Delta_{flat}}{W'_{slope}} \left(N + A' \cos\theta\right) \mu + N \sin\theta \cos\theta = 0 \quad (2.8)$$

where Δ_{flat} and Δ_{slope} denote the friction-loop offset of the flat and slope (Figure 2.7b), respectively; and W'_{slope} is the friction-loop half-width of the slope. Δ and W' can be expressed as:

$$\Delta = \frac{M_u + M_d}{2} \quad (2.9)$$

and:

$$W' = \frac{M_u - M_d}{2} \quad (2.10)$$

where M_u and M_d denote the measured frictional signal under the uphill and downhill motions, respectively. Based on equations (2.8)–(2.10), the conversion factor α can be obtained; the friction force f under specific normal load during the AFM nanoscratching can thus be determined by:

$$f = \alpha \cdot M \tag{2.11}$$

where M denotes the voltage-output difference between the scratching and non-scratching stages; this difference is recorded by the position sensitive detector (PSD) in the horizontal plane.

2.6 Challenges and Opportunities in SLM of Al-Al_2O_3 Nanocomposites

Several studies have successfully applied SLM in the fabrication of full-dense Fe, Ti and Ni alloys (Guan et al. 2013; Gu et al. 2011; Harrison et al. 2015). However, several challenges and opportunities remain in SLM of Al-Al_2O_3 nanocomposites.

2.6.1 Challenges

The main challenges within SLM of Al-Al_2O_3 nanocomposites include oxidation, high thermal conductivity and reflectivity as well as poor flowability of the powder.

i. Oxidation. Oxidation is considered to the most significant problem in SLM of Al. First, the formed oxide film on the powder surface can be incorporated into the molten pool, which affects the wetting to the surrounding powders. Second, any previously built solid tracks on the side and below the molten pool are also covered by the oxide films (Louvis et

al. 2011). Previous studies have shown that the oxide film on the upper surface of the pool is vaporized under the high temperatures of a laser beam (Limmaneevichitr and Kou 2000). The oxides at the sides of the pool, however, remain intact and the oxides stirred into the molten pool generate regions of weakness and porosity within the part. Figure 2.8 shows the schematic of the pores induced by oxide films.

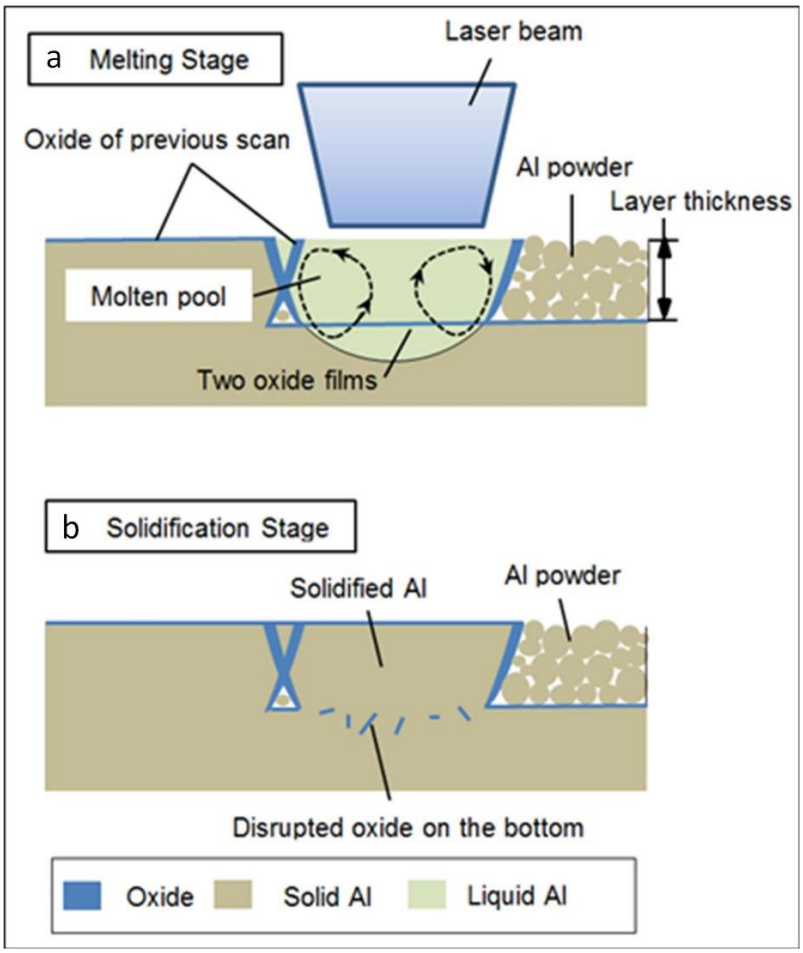

Figure 2.8: (a) Marangoni convection in molten pool (b) oxide disruption and solidification (Louvis et al. 2011).

As it is likely that the formation of oxide films during the SLM process cannot be avoided completely, new methods need to be devised

to minimise the influence of oxide films if the component produced is to be 100% dense (Louvis et al. 2011). Furthermore, it is important that the underlying and surrounding solid regions partially remelt so that the regions can wet and fuse within the molten pool. On the other hand, the added Al_2O_3 reinforcements exhibit poor wetting ability, a high laser powder thus is required to fully melt the Al_2O_3 particles, and prevents the formation of porosity and microcracks within the produced parts.

ii. High thermal conductivity. The thermal conductivity of Al is around 9 times higher than Ti and 13 times higher than stainless steel. This indicates that a higher laser power is required to fully melt Al and the Al_2O_3 powders (Steen et al. 2010).

iii. High reflectivity. The measured reflectivity of Al is 91% higher than Ti (70%), which indicates higher power lasers are needed to accumulate sufficient heat energy to fully melt the powders (Fischer et al. 2003).

iv. Poor flowability. Due to the light weight of Al, it is a challenge to deposit a thin powder layer uniformly on powder bed; a nonuniform powder layer may result in a poor dimensional accuracy and mechanical properties of the fabricated components.

The aforementioned challenges suggest the SLM of Al-Al_2O_3 nanocomposites is fairly difficult to produce nearly full-dense components. On the other hand, several studies have examined the SLM of Al alloys and provided insight and useful research methodologies which may be employed in the investigation of SLM of Al-Al_2O_3 nanocomposites.

2.6.2 Opportunities

The opportunities for SLM of Al-Al_2O_3 nanocomposites include:

i. Various Al alloys have been successfully processed using SLM. For instance, Rao et al. (2016) investigated the influence of process parameters on SLM manufactured aluminium alloy A357; it was found that the anisotropy of SLM-fabricated samples was caused by the directionality of the microstructure due to differences in the deformation response in both horizontal and vertical tensile samples. Prashanth et al. (2014) studied the effect of heat treatment on the microstructural and tensile behaviour of Al-12Si components produced by SLM; their study found that the annealing temperature that is employed is a major factor in affecting the microstructure and mechanical properties of the components.

   Kimura et al. (2017) investigated the effect of Si content on the mechanical and thermal conductivity of Al-xSi alloys fabricated by SLM; it was found that, with an increase in Si content, both yield strength and ultimate tensile strength increased, while elongation and thermal conductivity decreased. Li et al. (2016) employed a 200 W laser power to investigate the influence of low temperature powder drying on the relative density of SLM manufactured Al-12Si alloys; they found that the fabricated components using dried powder exhibited higher relative density because, the surface moisture was removed and thus prevented the formation of oxides during the SLM.

ii. Relative high-power lasers have been successfully applied to manufacture ceramic reinforced AMCs using SLM. A high laser power is required because, more heat energy input is needed to fully melt the ceramic reinforcement materials which normally have much higher melting temperature than aluminium.

Gu et al. (2012) employed a ytterbium fibre laser with a power of 200 W to fabricate AlSi10Mg-TiC nanocomposites and found that a ring-structured nanoscale TiC reinforcement was uniformly distributed along the Al boundaries, resulting in a remarkable improvement in both tensile strength and microhardness. Dadbakhsh et al. (2012) also examined the role of Fe_2O_3 additives in the development of the SLM processing window of pure aluminium powder. They reported that in-situ material reaction between Al and Fe_2O_3 powder released extra heat and energy which promoted the formation of a molten pool and improved the SLM processability over a wide range of SLM parameters. The released energy (which is proportional to the Fe_2O_3 content) is capable of manipulating the visual surface profile and roughness. However, the hardness of the fabricated composite samples was found to increase with an increase in the content of Fe_2O_3, which was attributed to the superior microstructure features of the particle reinforced matrix.

2.7 Summary

This chapter discussed the related work in the area of selective laser melting and synthesis of Al-Al_2O_3 composites, however, process knowledge is still lacking for the SLM of Al-Al_2O_3 nanocomposites. The typical process parameters used in selective laser melting include laser power, scanning speed, hatch spacing and powder layer thickness; unsuitable selection of them may lead to the formation of defects during the process. High-energy ball-milling is a simple and effective method to refine Al grain size and disperse Al_2O_3 nanoparticles homogeneously amongst Al matrix to synthesise an advanced Al-Al_2O_3 nanocomposites. Finite element analysis has been widely used for thermal behaviour prediction in selective laser melting so that a more efficient selection of process parameters could be offered in fabricating bulk samples. Although several challenges are remaining in selective laser melting of Al-Al_2O_3 nanocomposites such as oxidation, high reflectively and thermal conductivity and poor flowability, several studies have successfully applied in fabricating some types of Al alloys and Al-based composites, which provided insight and useful research methodologies which may be employed in the investigation of SLM of Al-Al_2O_3 nanocomposites.

Chapter III

Synthesis and Characterisation of Advanced Composite Powder

This chapter addresses the first research objective of this thesis. It focuses on the synthesis and characterisation of advanced Al-Al_2O_3 composite powder using high-energy ball-milling process and systematic analytical techniques. The hypothesis is that a short milling and long pause combination provides a higher yield and narrower particle size distribution range than long milling and a short pause. The chapter is organised as follows: Section 3.1 introduces the research methodology, including the research hypotheses, experimental techniques and theory. Section 3.2 provides the experimental study, including the materials used and procedures. Section 3.3 details the experimental results and discussion and Section 3.4 summarises this chapter afterwards.

3.1 Research Methodology

High-energy ball-milling (HEBM) is used in this study because, it is a simple and effective technique to refine particle grain size (~100 nm) and disperse reinforcement materials homogeneously in a metal matrix (Khan et al. 2008; Liao and Tan 2011; Razavi Tousi et al. 2009). Another advantage of HEBM lies in its ability to produce bulk quantities of solid-state materials using simple equipment at room temperature.

3.1.1 Research Hypotheses

The milling time is the most significant parameter during HEBM, the optimum milling time can be determined by evaluating the characteristics of ball-milled powder up to 24 hours of milling. The research hypotheses within HEBM of Al-4 vol.% Al_2O_3 nanocomposite powder include:

i. The HEBM contributes to Al grain refinement. The longer the milling time, the smaller the grain size is.
ii. The Al_2O_3 reinforcement could function as the grinding media and accelerate the Al powder refinement; the Al_2O_3 may be dispersed homogenously amongst Al matrix after about 20 hours of milling.
iii. A short milling and long pause combination may provide a higher yield and narrower particle size distribution range than long milling and a short pause.

3.1.2 Experimental Techniques and Theory

A standard 170 mesh sieve (90 μm) was employed to sieve the ball-milled composite powder in order to obtain a powder suitable for the SLM. The weight loss (W_Δ) and yield (φ) can be expressed as:

$$W_\Delta = W_i - W_o \qquad (3.1)$$

$$\varphi = \frac{W_{90}}{W_i} \times 100\% \qquad (3.2)$$

where W_i and W_o denote the weight of input and output, respectively, and W_{90} represents the weight of the powders that passed through the sieve with a particle size of less than 90 μm.

To measure the flow behaviour of the sieved ball-milled powders, the Carr index (CI) was used. The Carr index is the ratio of the difference between the apparent volume and the tapped volume to the apparent volume, and can be expressed as (Cain 2002; Carr 1965):

$$CI = \frac{V_A - V_T}{V_A} \times 100\% \qquad (3.3)$$

where V_A denotes the apparent volume that results from pouring the powder into a heap or container in the absence of any applied compression, and V_T represents the tapped volume resulting from the application of compression, for example, impact or vibration. Generally, a Carr index of less than 15% is considered to be an indicator of good flowability while greater than 20% indicates poor flowability (Yadroitsev 2009). The apparent and tapped volumes of the sieved ball-milled powders were measured in terms of ASTM D7481-09 to calculate the Carr index using a 100 mL standard graduated cylinder.

Other metrology and analytical techniques were employed for phase identification, grain size and uniformity evaluation and micro-hardness measurement for microstructure changes. More specifically, scanning electron microscopy (SEM) was used to observe the powders' morphology evolution. In addition to phase identification, X-ray powder diffraction (XRD) was also used to evaluate the average grain size when the grain size was less than 100 nm. The

average grain size d' can be expressed using the Scherrer equation (Choi et al. 2008):

$$d' = \frac{0.9\lambda}{\beta \cos\theta'} \qquad (3.4)$$

where β and θ' denote the full width at half maximum (FWHM) and Bragg angle, respectively, and λ is the wavelength of the X-radiation. Transmission electron microscopy (TEM) together with energy-dispersive X-ray spectroscopy (EDS) was used to evaluate the uniformity of the nano Al_2O_3 in the Al matrix by measuring the atomic and weight percentages of the constituent elements. On the other hand, the weight percentage of the Al elements in the Al-Al_2O_3 nanocomposite was determined by

$$W\% = \frac{W_1 + \frac{9}{17} \cdot W_2}{W_1 + W_2} \times 100\% \qquad (3.5)$$

where W_1 and W_2 denote the weight of Al and Al_2O_3 powders, respectively. This indicator can be used to validate the results from the TEM and EDS results.

To investigate the effect of both ball milling and nano Al_2O_3 reinforcements on the powders' mechanical properties, the Al and Al-Al_2O_3 composite as well as the raw Al powders were separately mounted in carbon-filled phenolic resins. The specimens were polished before microhardness testing. The Micro-Vickers Hardness Testing Machine HM-101 (Mitutoyo UK Ltd) was employed to measure the specimens' microhardness. The average Vickers hardness of each specimen was determined by measuring four different indentations with an applied load of 50 g.

3.2 Experimental Study

3.2.1 Raw Materials and Apparatus

Raw Al and Al_2O_3 powders were obtained from commercial vendors. Raw Al powder (-325 mesh, 99.5%) was acquired from the Alfa Aesar Corporation (Ward Hill, MA), and Al_2O_3 powder (50 nm particle size, TEM) was obtained from Sigma-Aldrich Ltd. (Dorset, UK). Figure 3.1a and b show the irregular shape of the raw Al and high surface energy-induced Al_2O_3 clusters. More details on the morphology of Al_2O_3 powder may be found in appendix A (Figure A-1). The particle size distribution of the Al was measured using the Malvern Mastersizer3000 (Malvern, U.K.). Figure 3.1c shows the average particle size of raw Al was 17.1 μm. A laboratory planetary mill with four working stations (PULVERISETTE 5 classic line, Fritsch GmbH, Idar-Oberstein, Germany) was employed to conduct the ball-milling experiments (Figure 3.1d) in this study.

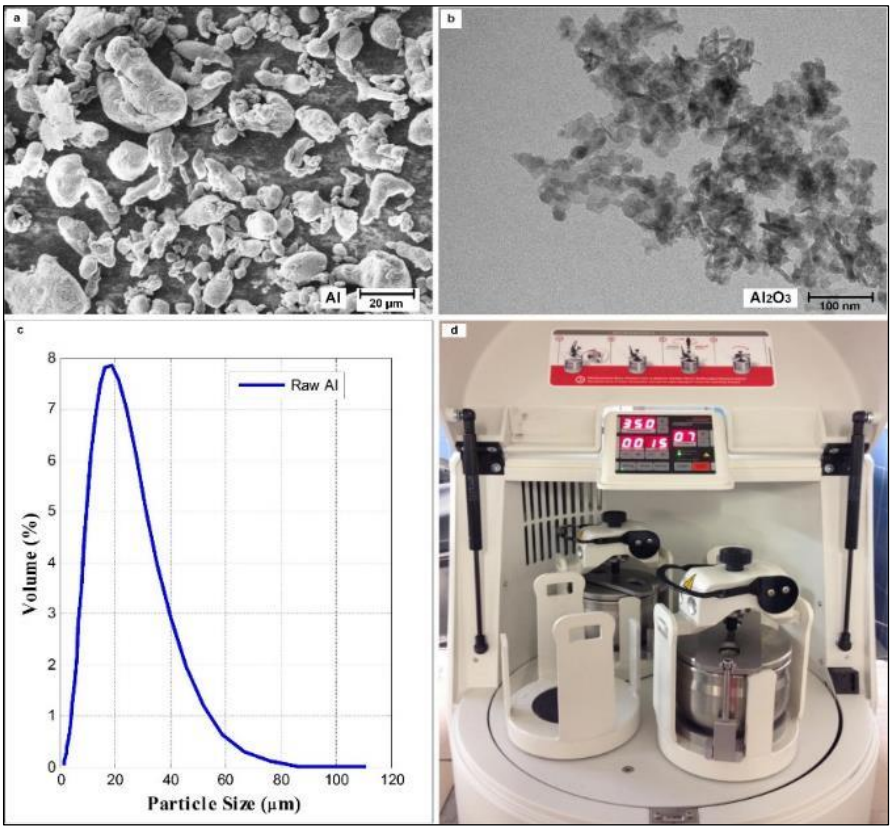

Figure 3.1: Raw materials and apparatus (a) raw Al, (b) raw Al_2O_3 powder, (c) particle size distribution of raw Al and (d) the employed ball mill machine.

3.2.2 Experimental Procedures

A stainless steel bowl was loaded with 200 g Al and 4 vol.% of Al_2O_3 powders with a ball-to-powder weight ratio of 5:1; meanwhile, to identify the effect of the nanoscale Al_2O_3 reinforcements on the ball-milled composite powders, 200 g of Al without Al_2O_3 was loaded into another stainless steel bowl (Han et al. 2017a). To prevent excessive cold-welding, 3 wt.% of stearic acid was widely used in previous studies when ball milling of Al powders, this is because 3 wt.% is not only sufficient to prevent excessive cold welding of the milled Al but also minimising the contamination of the ball-milled powders (Cintas et al. 2005;

Suryanarayana 2001); therefore, the suggested 3 wt.% of stearic acid is employed and 200 g Al powder without stearic acid was milled followed by 200 g Al powder with 3 wt.% stearic acid. 3 wt.% stearic acid was also added to the bowl loaded with 200 g Al and 4 vol.% of Al_2O_3 powders.

Further, to prevent oxidation during the HEBM process, the grinding bowls were filled with argon gas, and a lock device was used to gas-tight seal the bowls in the glove box. The milling speed was set at 350 rpm, and the samples were taken out every four hours for analysis until 24 hours of milling had been completed. To investigate the influence of the milling and pause time on the yield and powder characteristics, two sets of experiments were conducted separately; the first set of experiments employed a 15-minute milling and 5-minute pause combination (further referred to in this thesis as method 1) while the second experiment involved a 10-minute milling and 15-minute pause combination (method 2) (Han et al. 2016). The samples that were taken out were subject to systematic analysis for powder characterisation, which is discussed in the next section.

3.3 Results and Discussion

Powder characterisation is considered to crucial, because the ball-milled powders under different conditions generally offer different characteristics and properties; systematic analytical methods thus are required to evaluate the characteristics of the ball-milled powders suitable for selective laser melting.

3.3.1 Particle Size Distribution and Yield Evaluation

The milled Al powder without a PCA is shown in Figure 3.2 up to 6 hours of milling. It can be seen that the Al particles welded together to form a spherical shape with an average particle size of 2.5 mm (Figure 3.2c). It should be noted that some of the particles stuck to the surface of the stainless steel balls and some were flattened due to the intensive impact. This can be attributed to the ductile and soft nature of Al. Unfortunately, the stuck ductile Al hindered further grain refinement due to a lack of sufficient collision energy.

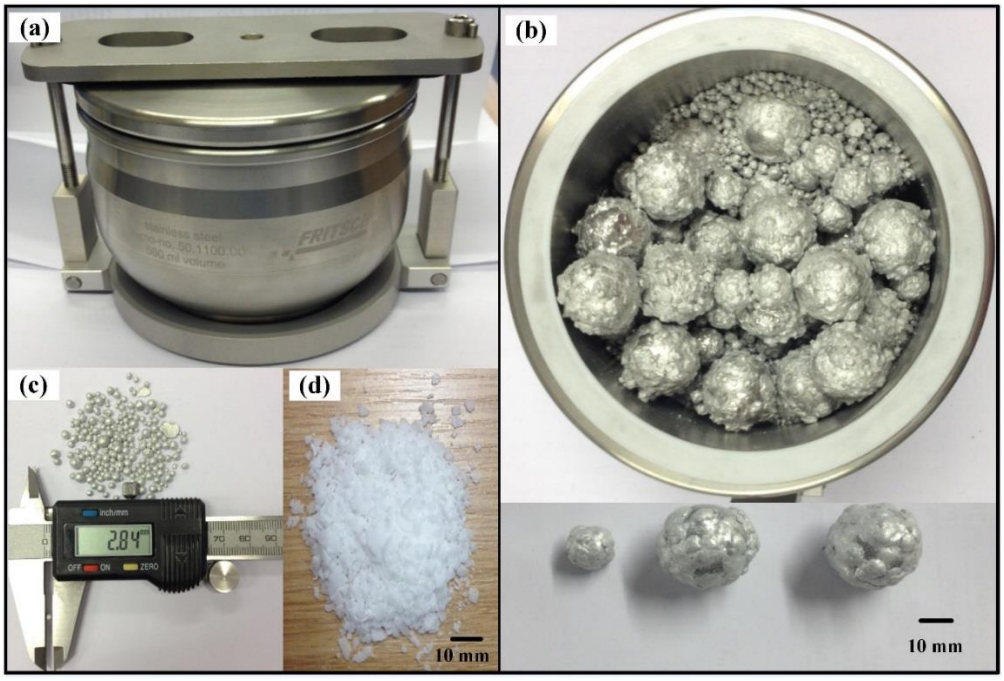

Figure 3.2: The milled Al powders without a PCA (a) the bowl with lock system (b) the ball-milled pure Al without PCA up to 6 h (c) particle size of the ball-milled Al and (d) the stearic acid powder.

Figure 3.3 shows the Al particle size variation following up to 6 hours of milling without a PCA. The average particle size remained approximately 2.5 mm after 6 hours of milling, which confirmed the fact that the stuck Al hindered further

grain refinement and confirmed the necessity for the usage of a lubricant. Therefore, 3 wt.% stearic acid (Figure 3.2d) was added to refine the Al grain size and avoid any unwarranted and excessive cold welding of the Al particles amongst themselves, onto the internal surface of the bowl and to the surfaces of the grinding balls.

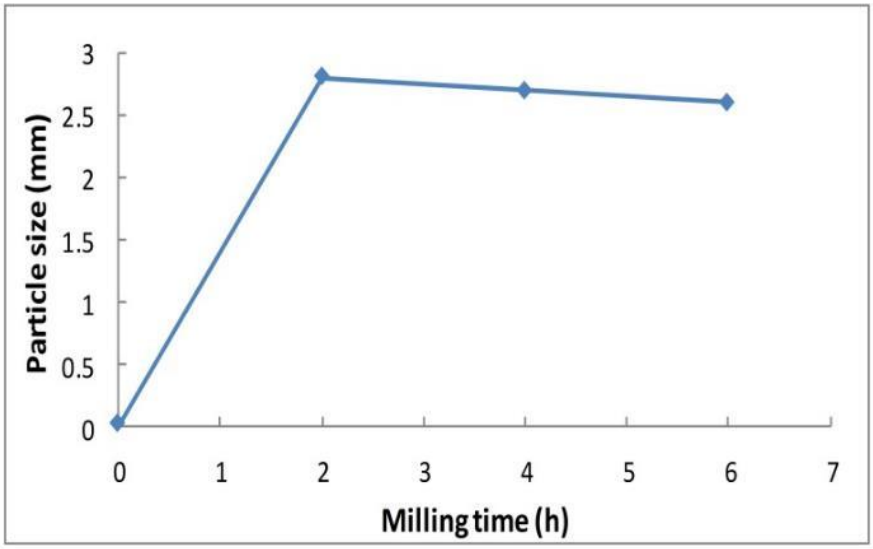

Figure 3.3: Al particle size variation following up to 6 hours of milling.

Figure 3.4a and b show two types of Al-4 vol.% Al_2O_3 composite powder ball-milled for 20 hours when employing two different combinations of milling and pause duration. More specifically, when the milling and pause time were set at 15 and 5 minutes, respectively (method 1), some large and plate-like particles formed in the ball-milled composite powder (Figure 3.4a), which can be attributed to the agglomeration of the very fine composite powder. Nevertheless, very few plate-like particles were found in the composite powder when employing the 10-minute milling and 15-minute pause combination (method 2, Figure 3.4b).

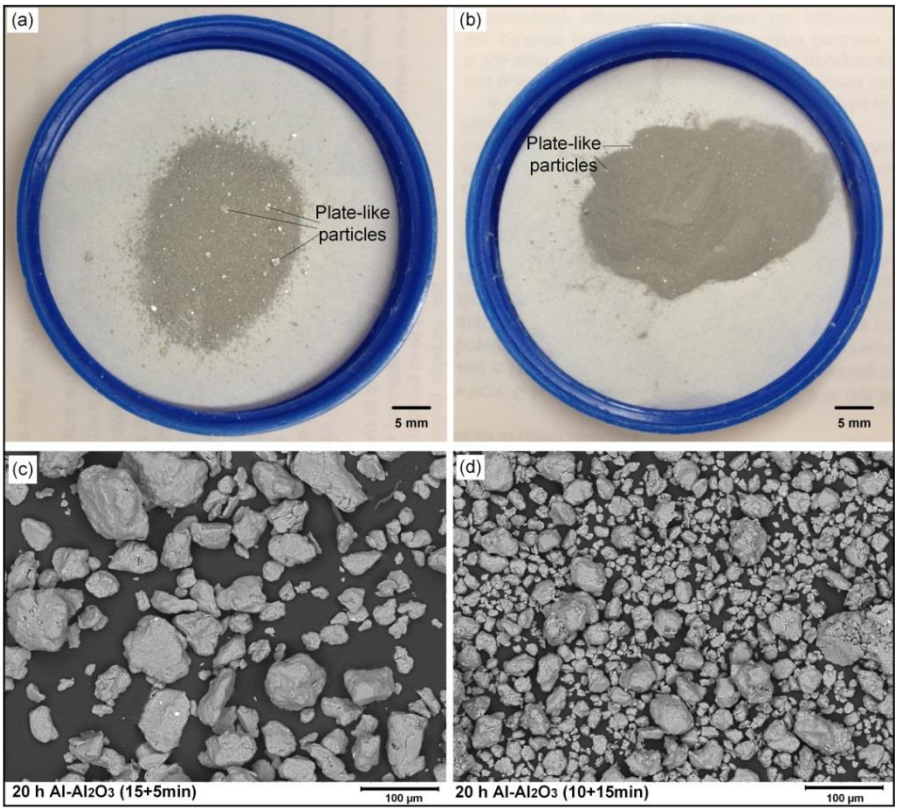

Figure 3.4: Two types of composite powder ball-milled for 20 hours.

To produce advanced Al-Al_2O_3 nanocomposite powders suitable for the SLM, both types of composite powder were subject to sieving. The particles that passed through the 170 mesh sieve ($\leqslant$90 μm) are shown in Figure 3.4c and d, that is, Figure 3.4c shows the sieved composite powder fabricated by method 1 (15+5 minutes) while Figure 3.4d shows the sieved composite powder produced by method 2 (10+15 minutes). Compared to the method 1-produced composite powder, the composite powder produced by method 2 offered a much smaller particle size and more spherical particle shape.

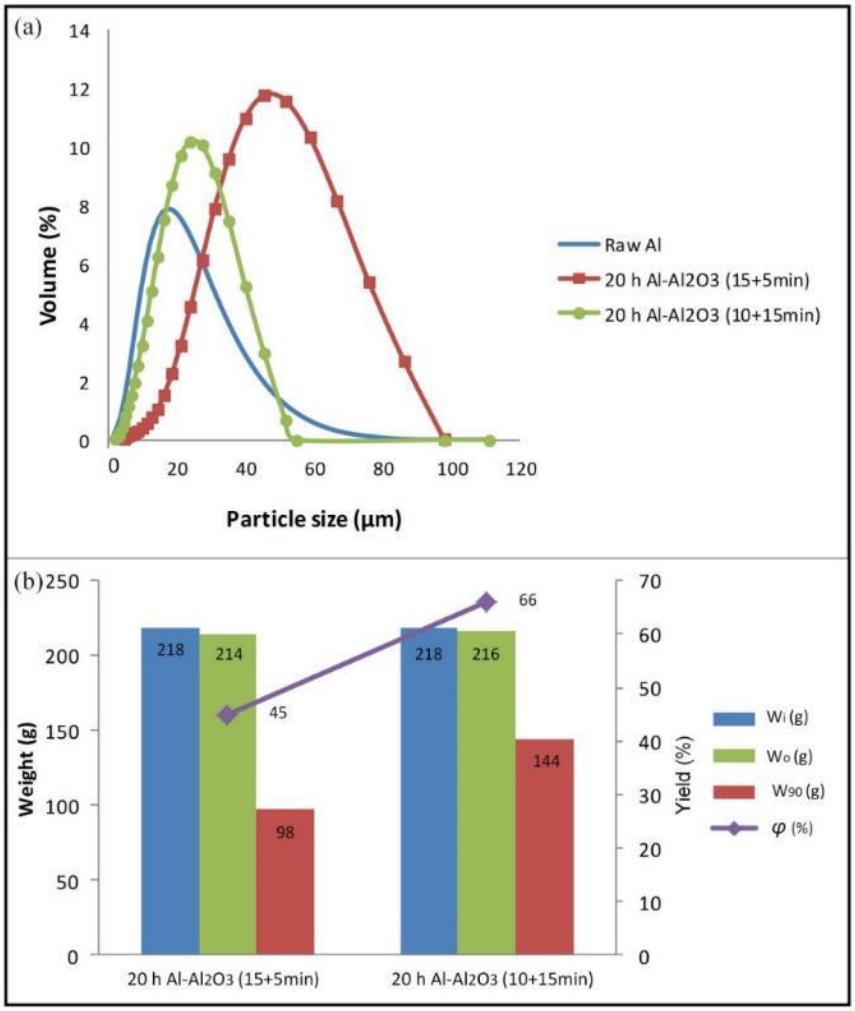

Figure 3.5: The particle size distribution and yield of the sieved nanocomposite powders.

Further, the particle size distribution of the two sieved composite powders was obtained using the Malvern Mastersizer3000 (Figure 3.5a). Following ball milling for 20 hours, the composite powder from method 1 provided an average particle size of 45 µm with a broad range of particle sizes between 5 and 90 µm while method 2 produced a composite powder exhibiting an average particle size of 25 µm with a much narrower particle size range between 2 and 55 µm. Therefore, from a particle size distribution point of view, the sieved composite

powder ball-milled for 20 hours from method 2 would be more suitable than the method 1-produced composite powder for the SLM for two reasons. First, small particles tend to provide larger surface areas and thus contribute to a higher laser energy absorption rate during the laser melting stage than large particles, and second, the particles with a narrow range of particle sizes could ensure high dimensional accuracy in each powder layer during the powder deposition stage and further ensure the dimensional accuracy of the final parts.

In addition to particle size distribution, yield was another key factor employed to evaluate the two methods used to produce advanced SLM suitable Al-Al_2O_3 nanocomposites. In both experiments, the weight of the input (W_i) was 218 g, which consisted of 200 g Al, 4 vol.% of Al_2O_3 (12 g) and around 3 wt.% of stearic acid (6 g). When method 1 was employed, the weight of the output (W_o) was approximately 214.5 g compared to 216 g from method 2. Due to the presence of sufficient lubricant, almost no powder was found sticking to the surface of the grinding bowls and balls after 20 hours of milling. In terms of equation (3.1), the weight loss (W_Δ) in the two experiments was 3.5 g and 2 g for methods 1 and 2, respectively. Moreover, after sieving, the weights of the particles with a particle size of less than 90 μm (W_{90}) were 98 g and 144 g, respectively. Yields (φ) of 45% (method 1) and 66% (method 2) can thereby be determined using equation (3.2). It should be noted that, for both the methods, there was no apparent change in particle size distribution and yield of the ball-milled powder between 20 and 24 hours of milling.

It should be noted that method 1 provided a high weight loss and low yield while method 2 offered a low weight loss and relatively high yield, which can be attributed to the different weights of the stearic acid that remained in the composite powders after 20 hours of milling. Indeed, due to the intensive impacts of the grinding balls during HEBM, the temperature in the bowls increased gradually, and when the temperature was over 90°C, the lubricant (stearic acid) started to volatilise, which led to the welding and agglomeration of the refined composite powder. Generally, a short milling and long pause time combination together with built-in fans could cool the grinding bowls better than a long milling and short pause time combination. Therefore, the weight loss (W_{Δ}) of 3.5 g and 2 g for methods 1 and 2, respectively, can be primarily attributed to the volatilisation of the stearic acid.

3.3.2 Morphological Evolution

The morphology of the composite powder was considered to be important to determine whether it would be suitable for SLM as this would affect the powder's flow behaviour in the powder layer deposition stage. Figure 3.6 shows the morphological evolution of the Al-Al_2O_3 nanocomposites and Al powders following up to 20 hours of milling when method 2 was used.

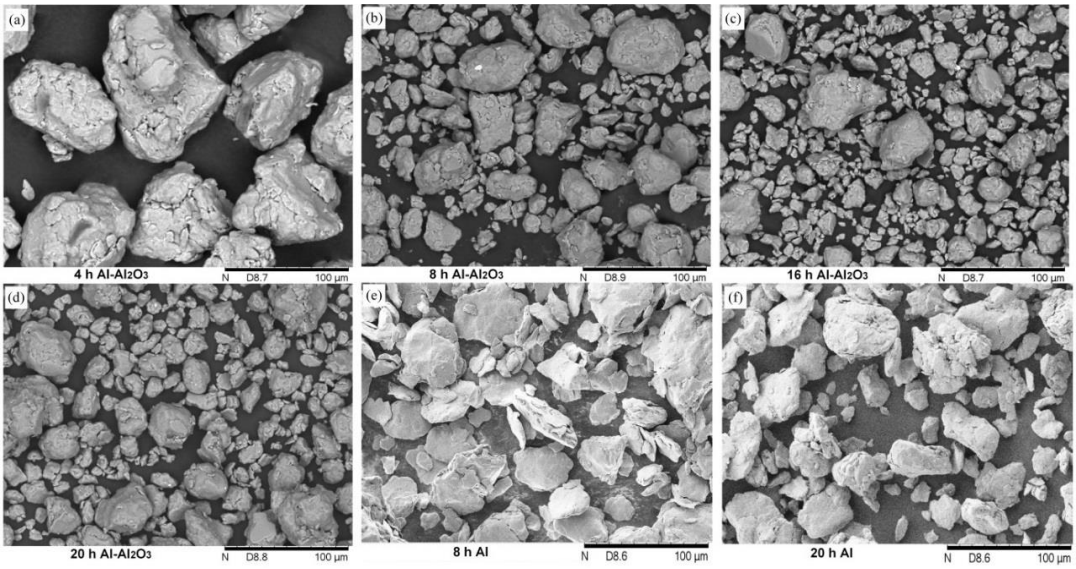

Figure 3.6: The morphological evolution of the Al-Al_2O_3 nanocomposites and Al powders ball-milled for up to 20 hours.

More specifically, Figure 3.6a shows the morphology of the composite powder ball milled for 4 hours; it can be seen that the welded particles had irregular shapes and had particle sizes of more than 100 µm, which can be explained by the ductile nature of Al. With the continued milling process, the fracture mechanism was activated, and some large particles were crushed due to intensive impacts, which resulted in morphological changes and particle size reduction (Figure 3.6b). When the milling time was increased to 16 hours, the fracture phenomenon was more prominent and a considerable number of small particles (particle size around 20 µm) were formed. Meanwhile, some particles exhibited nearly spherical shapes whilst a few large particles remained (Figure 3.6c).

When the milling time was extended to 20 hours (Figure 3.6d), the composite powder offered a much narrower particle size range and more nearly

spherical particles were formed. In fact, there was no apparent change in the particle size and morphology when the milling time was over 20 hours, and this can be attributed to the achieved steady state between the cold-welding and fracture mechanisms. However, Tousi et al. (2009) found that the Al-Al_2O_3 composite powder could reach steady state when the milling time was up to 15 hours. This can be explained by the employment of process parameters, that is, in the present work, the employed ball-to-powder weight ratio was 5:1 compared to the 15:1 in literature. A higher ball-to-powder weight ratio could generate more intensive impacts of the grinding balls and thereby shorten the milling time. On the other hand, the higher weight ratio tended to produce a smaller quantity of milled powder in one milling.

To investigate the effect of the added nano Al_2O_3 on the powders' morphological evolution, the morphologies of the Al powder subjected to 8 and 20 hours of milling were also examined and are shown in Figure 3.6e and f. It can be seen that, compared to the composite powder ball-milled for 8 hours, the Al powder ball-milled for 8 hours was still in the plastic deformation stage, and cold-welding was the prominent mechanism as most of the particles were plate-like in shape. This can be explained by the fact that the added 4 vol.% of nano Al_2O_3 reinforcement functioned as the grinding media in the composite powder ball-milled for 8 hours. Together with the loaded grinding balls, this stimulated and shortened the plastic deformation duration, and the fracture mechanism was activated ahead of 8 hours of milling. When both the nanocomposite and Al powders ball-milled for 20 hours were compared, the former exhibited more spherical shapes and a narrower range of particle size distribution than the latter,

which suggested that the former would be more suitable for the SLM process and would offer better flowability. More details on the morphological evolution of the pure Al and nanocomposite powder may be found in appendix A (Figure A-4, 5).

3.3.3 Flowability Analysis

Composite powders' flowability is considered crucial for the SLM process as it determines the powder's deposition performance. Generally, good-flowing powders generate powder layers with continuous and uniform thickness while poor-flowing powders lead to non-uniform layers, which are detrimental to the dimensional accuracy and mechanical properties of the final parts. The CI can be used to evaluate the flow behaviour of advanced ball-milled Al-Al_2O_3 nanocomposite powders. As mentioned previously, powders with a CI of less than 15% are considered to have good flowability while a CI greater than 20% implies poor flowability.

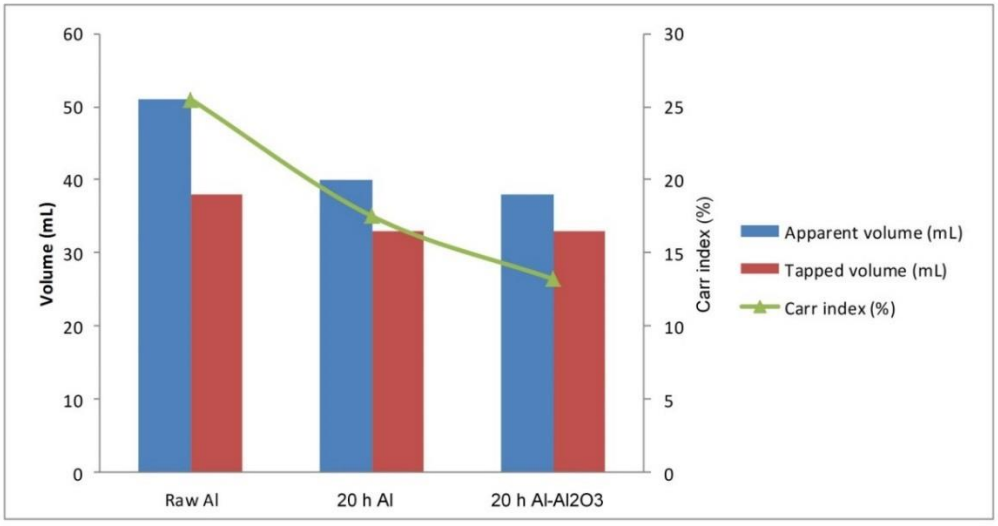

Figure 3.7: Flowability measurements and the Carr index (CI).

Figure 3.7 shows the measurement results for 55 g of raw Al and the same mass of Al and Al-Al_2O_3 nanocomposite powders ball-milled for 20 hours. The measured apparent and tapped volumes for the raw Al were 51 mL and 38 mL, respectively. The tapped volume was obtained by tapping the 100 mL cylinder 500 times and measuring the tapped volume to the nearest graduated unit. Using equation (3.3), the CI was determined to be 25.5%. Likewise, the measurements of the Al and Al-Al_2O_3 nanocomposite powders ball-milled for 20 hours were taken, and further, the CI values were determined to be 17.5% and 13.2%, respectively.

The results indicated that amongst the three powders, the Al-Al_2O_3 nanocomposite powder ball-milled for 20 hours exhibited the best flowability followed by the Al ball-milled for 20 hours, while the raw Al offered poor flowability with a CI of 25.5%. This can be explained by two factors, the first of which is the powder's morphological evolution. Generally, spherical powders tend to have better flowability than non-spherical powders. The morphologies of the raw Al and the Al and Al-Al_2O_3 nanocomposite powders ball-milled for 20 hours are shown in Figures 3.1 and 3.4, respectively. As shown, some of the composite particles have a nearly spherical shape while most of the Al powder ball-milled for 20 hours is equiaxed in shape; the raw Al however exhibits an irregular shape. The second factor is the addition of the stearic acid, which functioned as a lubricant and further improved the flow behaviour of the ball-milled powders by reducing the friction between adjacent particles.

Therefore, it can be concluded that the raw Al powder was likely to be unsuitable for the SLM process because, during the powder layer deposition, a non-uniform layer could be generated, resulting in poor dimensional accuracy of the final parts. Notwithstanding, when employing a combination of 10-minute milling and a 15-minute pause, the produced advanced Al-Al_2O_3 nanocomposite powder ball-milled for 20 hours not only provided an ideal particle size distribution, but also offered good flowability and was therefore considered to be suitable for the SLM process.

3.3.4 Phase Identification and Uniformity Evaluation

To investigate contamination and the phases formed during the ball-milling process, the XRD patterns of the composites and Al powders following up to 20 hours of milling were measured and are shown in Figure 3.8. More specifically, after 20 hours of milling, the diffraction patterns of the milled Al still exhibited typical Al peaks, but these were broadened, which could be attributed to refinement of the Al grains. It also indicated that the iron elements from the grinding bowl and balls were not present or were below the levels of detection. This finding was in agreement with (Choi et al. 2008), in which the observed XRD patterns of Al broadened and mean grain size reduced until the milling time was up to 24 hours. This phenomenon validated the hypothesis that the ball milling significantly contributed to the grain refinement. Nonetheless, the peaks of the composite powder ball-milled for 20 hours exhibited a slightly horizontal offset and relatively weak intensity compared to the 20 hours-milled Al. This can be

explained by the fact that the nano Al_2O_3 reinforcements were embedded in the Al matrix, which also broadened the peaks of the composite powder.

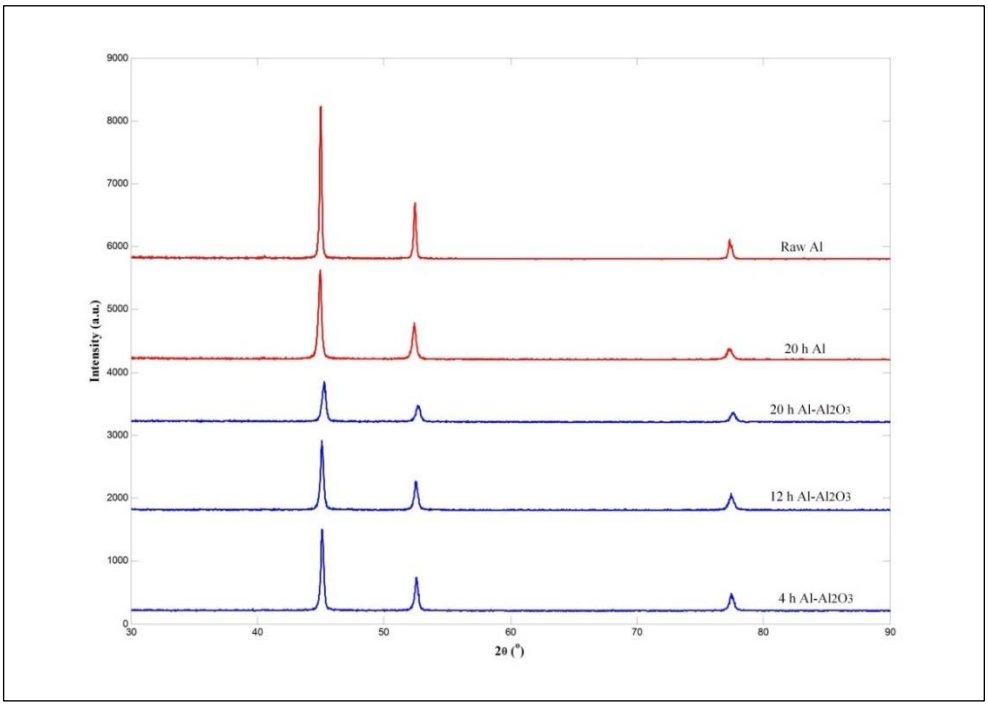

Figure 3.8: The XRD patterns of the Al-Al_2O_3 composite and Al powders ball-milled for up to 20 hours.

It should also be noted that the patterns of the Al_2O_3 powder were not detected in the XRD spectrum, this however was different from the observation elsewhere (Prabhu et al. 2006). In literature, the spectrum of nano Al_2O_3 powder was detected in the composite powder's XRD diffraction patterns. This can be attributed to the fact that the employed volume fraction of Al_2O_3 powder in (Prabhu et al. 2006) ranged from 20% to 50%, which was much higher than the volume fraction used in the present work (4 vol.%). It can be seen that the measured FWHM of the 20 hours-milled composite powder was larger than that of 20 hours-milled Al, which validated the hypothesis that the added nano Al_2O_3

reinforcement would serve as the grinding media and accelerate the Al powder grain refinement. The average grain size of the Al and Al-Al_2O_3 composite powders ball-milled for 20 hours were determined using equation (3.4) and were 48 nm and 42 nm, respectively. The patterns of the Al-Al_2O_3 nanocomposite powder after 4 and 12 hours of milling are also shown in Figure 3.8, which illustrates that the peaks broadened with the continued milling process.

The uniformity of the nano Al_2O_3 reinforcements in the Al matrix was crucial for the mechanical property improvement of the composite, but the XRD spectrum could not provide more information on this. TEM inspections however did offer a visual and qualitative evaluation. Figure 3.9a shows a typical TEM image of Al powder milled for 20 hours, and some individual Al grains can be clearly observed. Meanwhile, Figure 3.9b shows the TEM image of the composite powder ball-milled for 20 hours in which the dispersed nano Al_2O_3 particles were embedded in Al and the original Al grains were split into new grains. This behaviour finally contributed to the improvement in the mechanical properties of the Al-Al_2O_3 nanocomposite. Other study (Kang and Chan 2004) also found that the nano Al_2O_3 particles tended to fill in the gaps between Al powders during powder mixing process. The nano Al_2O_3 could pin grain boundaries and give rise to grain-refinement to improve the mechanical properties. It was also reported that when the volume fraction of Al_2O_3 was over 4%, the nano particles on the grain boundaries would reach saturation and the effect of the nano particles on grain boundary pinning could diminish and thereby reduce the mechanical properties of the composite.

Indeed, when subjected to external load, the Al matrix bears the major portion of the applied load while the small dispersed particles (Al_2O_3) hinder the motion of the dislocations; plastic deformation is thereby restricted such that yield and tensile strength, as well as hardness, are improved. Even at high temperatures, the strengthening remains and for extended time periods because the dispersed Al_2O_3 particulates are unreactive with the Al matrix.

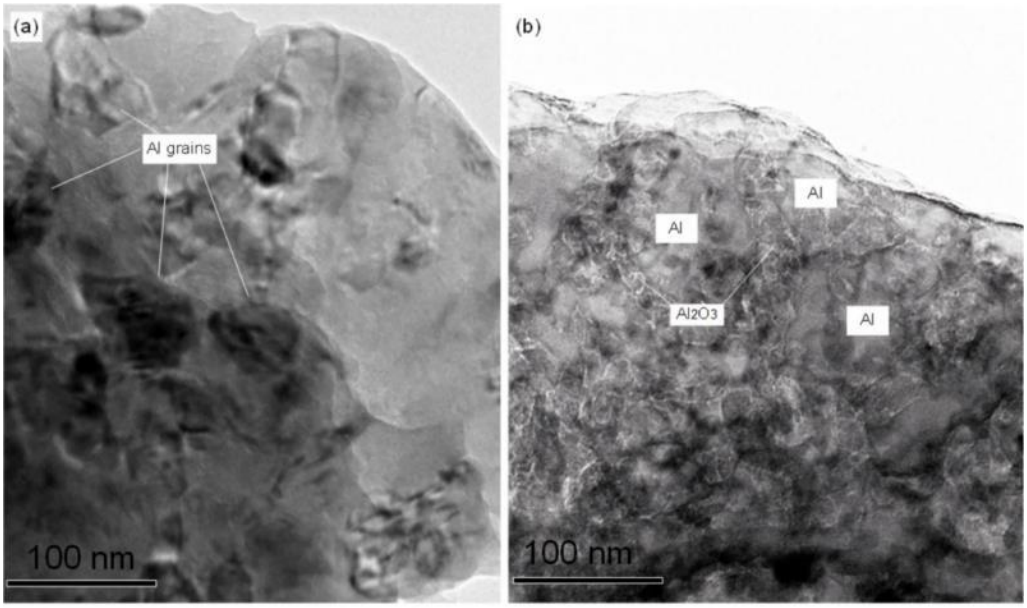

Figure 3.9: TEM images of the Al and Al-Al_2O_3 nanocomposite powders ball-milled for 20 hours.

Nonetheless, it was not easy to quantitatively measure the uniformity of the dispersed nano Al_2O_3 reinforcements in the Al matrix. Compared to the other analytical techniques (e.g. TEM), EDS mapping provided a relatively accurate method to evaluate the uniformity. Figure 3.10a shows the measured area of a composite particle while Figure 3.10b shows the distribution of the two elements Al and O in the measured image field. It can be seen that the oxygen was

uniformly distributed in the measured image field, and only Al and O were detected in the EDS spectrum (Figure 3.10c).

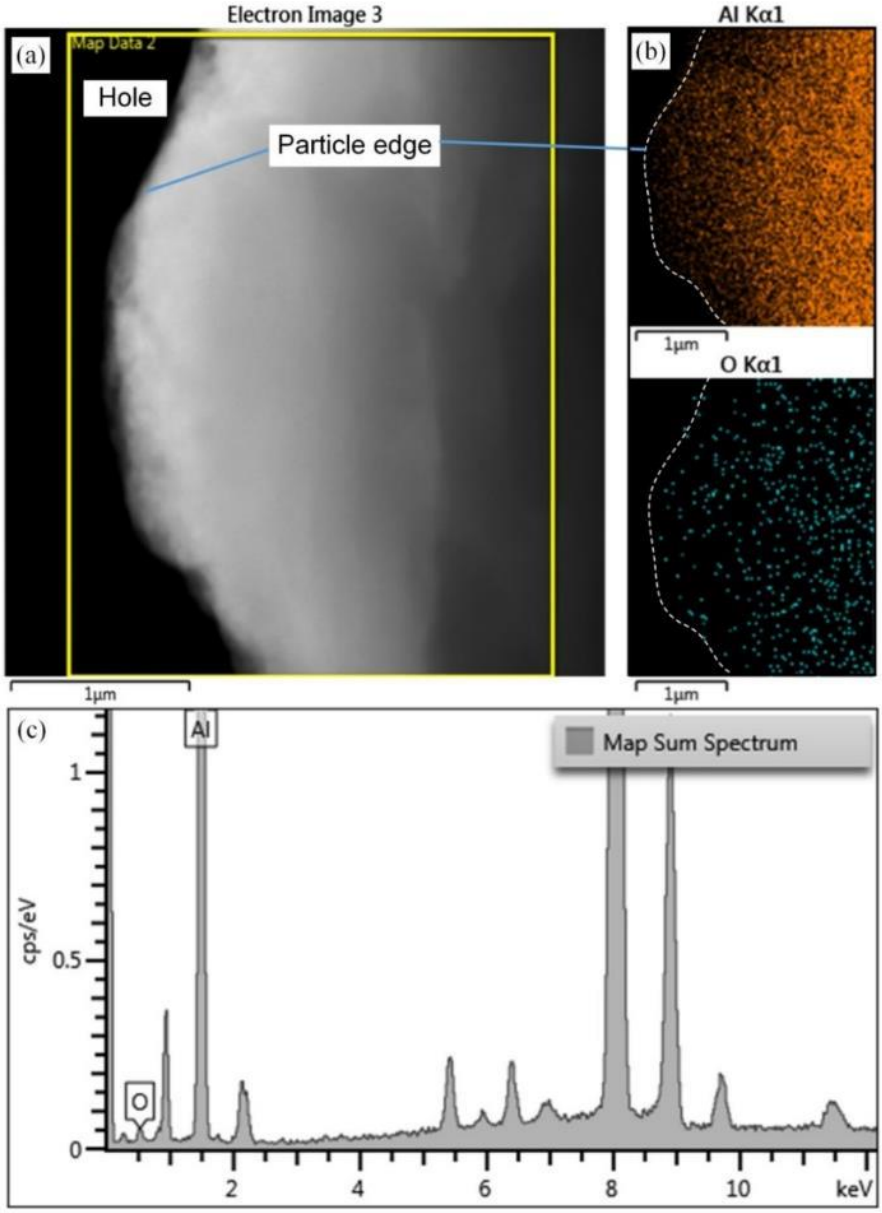

Figure 3.10: EDS patterns of the Al-Al_2O_3 nanocomposite powder ball-milled for 20 hours.

The atomic and weight fractions of the Al and O elements are shown in Table 3.1. The weight percentages of the Al and O elements determined using EDS were 97.64% and 2.36%, respectively. As the Al weight percentage determined using equation (3.5) was 97.34%, the weight percentage of the O element was 2.66%. On the other hand, due to oxidation, a very thin oxide film had formed on the surfaces of the composite particles, and Figure 3.11 shows at TEM image of the formed oxide films with a thickness of 3 nm.

Due to the fact that the thickness of the oxide film was ultrathin, the weight of the O element from the film was relatively low and could be neglected when calculating the weight percentage of the O element. Thus, the results obtained from EDS mapping and equation (3.5) were considered to be consistent. Therefore, it can be concluded that the hypothesis was validated that the nano Al_2O_3 particles were dispersed relatively uniformly in the Al matrix after 20 hours of milling.

Table 3.1**:** Atomic and weight fractions of the elements of the nanocomposite powder ball-milled for 20 hours

Element	**Atomic %**	**Weight %**
Al	96.08	97.64
O	3.92	2.36
Total	100	100

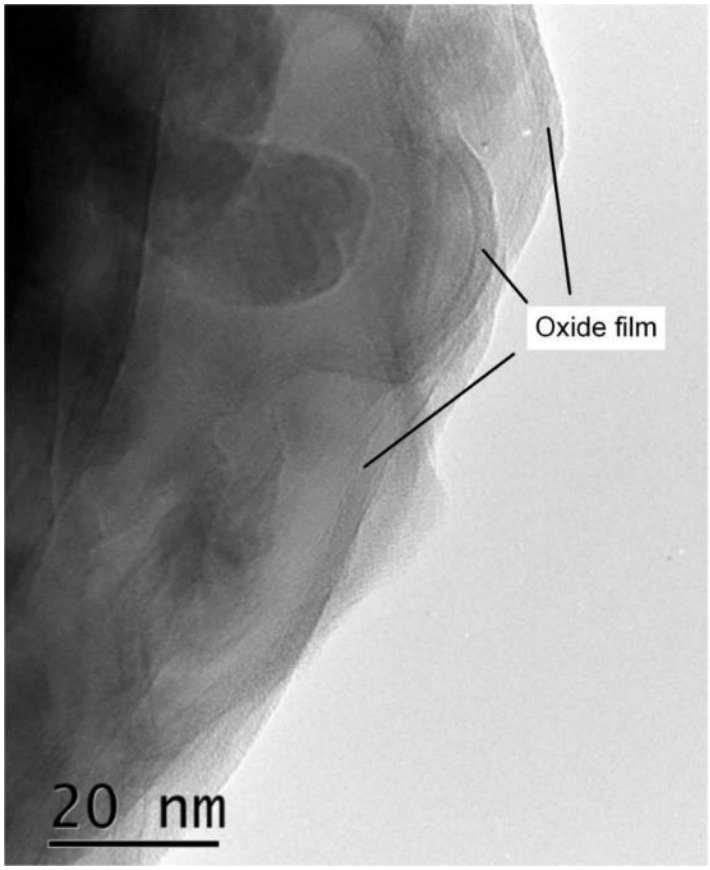

Figure 3.11: Formed oxide films on the surface of the Al-Al_2O_3 nanocomposite powder.

3.3.5 Microhardness Analysis

Figure 3.12a shows a prepared microhardness testing specimen of the Al-Al_2O_3 nanocomposite powder ball-milled for 20 hours. Optical microscopy inspections indicated that the composite powders were uniformly mounted in the phenolic resins. The obtained Vickers microhardness results are shown in Figure 3.12b. It can be seen that the measured microhardness values of the raw Al varied from 49 HV0.05 to 58 HV0.05, and an average microhardness of 52.2 HV0.05 was thereby obtained.

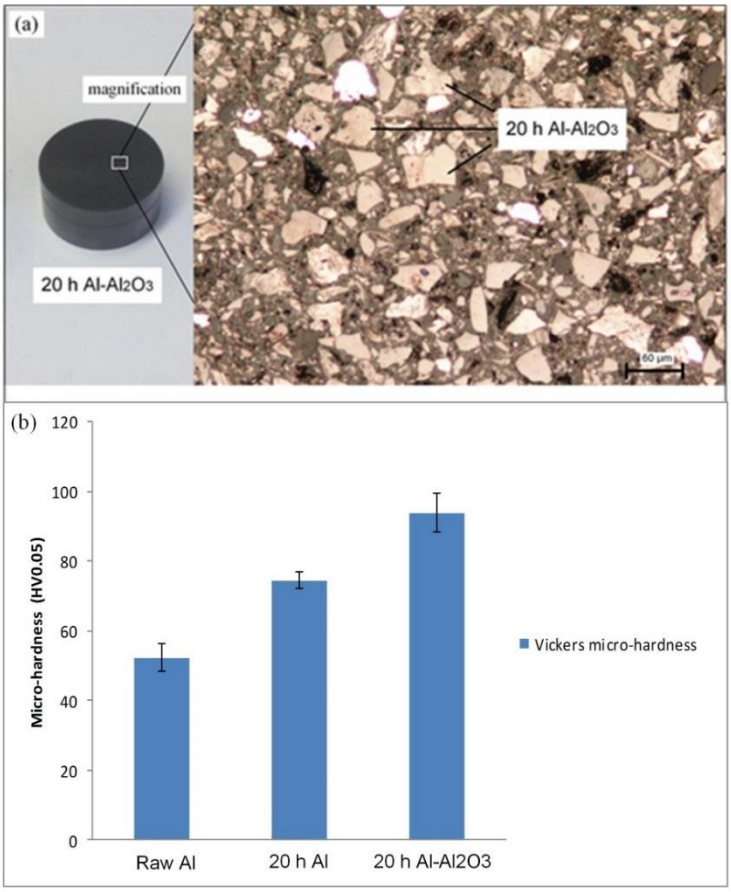

Figure 3.12: Microhardness testing results.

Compared to the raw Al, the obtained average Vickers hardness of the Al powder ball-milled for 20 hours was 74.5 HV0.05. The significant increase in microhardness was closely correlated to the observed powder's microstructure evolution. More specifically, the broadened peaks in Figure 3.8 indicated the Al grain refinement induced by HEBM and the TEM image in Figure 3.9a validated that the Al grain size was refined after 20 hours of milling. The Al grain refinement resulted in the increase in the grain boundaries, which thereby restricted dislocation motion and plastic deformation.

As for the Al-Al_2O_3 nanocomposite powder ball-milled for 20 hours, the measured average microhardness increased by 26% in comparison with the Al powder ball-milled for 20 hours. Likewise, this can also be explained by the powder's microstructure changes. In the first place, the observed FWHM of the 20 hours-milled composite powder was larger than that of 20 hours-milled Al powder (Figure 3.8), which indicated the average grain size of the nanocomposite powder was smaller than the Al powder.

In addition, the addition of the 4 vol.% nano Al_2O_3 reinforcement was another factor that resulted in the increase in hardness. The TEM image (Figure 3.9b) and EDS spectrum (Figure 3.10) indicated that the Al_2O_3 reinforcement was distributed uniformly amongst the Al matrix up to 20 hours of milling. Therefore, both the effect of the ball milling on the Al matrix and the effect of the Al_2O_3 reinforcement contributed to the increase in the microhardness of the milled composite powder.

3.4 Summary

This chapter addresses the synthesis and characterisation of ball-milled Al-Al_2O_3 nanocomposite powder for selective laser melting. It focused on the study of the effect of milling and pause duration on the yield of Al-Al_2O_3 nanocomposite powder and employed advanced nano-metrology methods and analytical techniques to study the characteristics of the composite powder. The composite powder ball-milled for 20 h was considered to be suitable for selective laser melting due to its nearly spherical morphology, good flowability and high

mechanical property. It was found that the Al_2O_3 reinforcement functioned as the grinding media and accelerated the Al powder refinement; the Al_2O_3 was dispersed fairly homogeneously amongst Al matrix after about 20 hours of milling. Furthermore, a short milling and long pause combination provided a higher yield and narrower particle size distribution range than long milling and a short pause. In addition, the employed analytical techniques and advanced metrology methods in this chapter can also be used to explore the synthesis of other new materials used for selective laser melting.

Chapter IV

Finite Element Simulation of First Layer in SLM

This chapter addresses the second research objective of this thesis. It investigates the simulation of selective laser melting the first layer's Al-Al_2O_3 powder in order to provide a more efficient combination of process parameters used in fabricating bulk samples. A 3D finite element model is developed to predict the transient temperature distribution and molten pool dimensions during the laser scanning. Further, in order to validate the simulation results, the selective laser melting of first layer's Al-Al_2O_3 powder is performed prior to the SLM of bulk specimens. This chapter is organised as follow: Section 4.1 offers details of the 3D finite element modelling. Section 4.2 provides the results of thermal behaviour prediction, including transient temperature distribution and molten pool dimensions. Section 4.3 discusses the experimental validation and Section 4.4 summarises this chapter afterwards.

4.1 Finite Element Modelling

The quality of the parts produced via SLM generally depends on the thermal behaviour of the molten pool under various operating parameters, such as laser power, scanning speed, hatch spacing and scanning strategy (Mercelis and Kruth 2006). In order to obtain the desired SLM components, further research is thus

required to explore the correlation between the process parameters and the thermal behaviour during SLM (Childs et al. 2004). It is difficult to measure the thermal behaviour during practical SLM applications, however, due to the extremely rapid melting and cooling rate; numerical simulation is thereby considered to be a suitable approach for exploring these issues.

4.1.1 Assumptions

The following assumptions are made in this simulation in order to create a mathematically tractable model:

- The composite powder bed was assumed to be homogeneous and continuous.
- The heat flux from the laser beam was modelled as Gaussian-distributed heat flux in space and was given directly on the top of the composite powder bed.
- The convective heat transfer coefficient between the environment and the powder bed was assumed to be a constant.
- Radiation was ignored.
- The laser is assumed to be running continuously.

4.1.2 Modelling and Simulation Setup

A basic heat transfer model consists primarily of a heat source module and a thermal physics module. The thermal equilibrium equation follows the classical 3D heat conduction equation given by (Hussein et al. 2013):

$$\rho c \frac{\delta T}{\delta t} = \frac{\delta}{\delta x}\left(k \frac{\delta T}{\delta x}\right) + \frac{\delta}{\delta y}\left(k \frac{\delta T}{\delta y}\right) + \frac{\delta}{\delta z}\left(k \frac{\delta T}{\delta z}\right) + Q \qquad (4.1)$$

where ρ is the material density; c is the specific heat capacity; T is the temperature; t is the interaction time and $Q = (x, y, z, t)$ is the volumetric heat generation. The heat flux $I(r)$ follows a Gaussian distribution and can be expressed as (Hussein et al. 2013):

$$I(r) = \frac{2AP}{\pi {r_0}^2} \exp(-\frac{2r^2}{{r_0}^2}) \qquad (4.2)$$

where A is absorptivity, P and r are laser power and radial distance from the laser centre, respectively, and r_0 denotes the laser spot radius.

The absorptivity of a composite powder containing *n* components can be calculated using the following equation (Tolochko et al. 2000):

$$A = \sum_{i=1}^{n} A_i \gamma_i \qquad (4.3)$$

where A_i and γ_i denote the absorptivity and volume fraction of a component, respectively. Tolochko et al. (2000) measured the absorptivity of Al_2O_3 powder to be 3% under a pulsed Nd-YAG laser (λ=1.06μm pulse duration of 5ms, repetition rate up to 20Hz, energy content per pulse up to 20J). In the present work, the nanocomposite powder was composed of 96 vol.% Al and 4 vol.% Al_2O_3 powder. The absorptivity of Al is normally considered 9% (Li and Gu 2014); the absorptivity of Al-Al_2O_3 composite powder may then be determined using equation (4.3), yielding an absorptivity of 8.76%.

The porosity of the powder bed is crucial in SLM, as it affects both the thermal conductivity of the powder in the laser melting stage and the porosity of

the final parts; the powder bed porosity φ' can be expressed as (Li and Gu 2014):

$$\varphi' = 1 - \frac{\rho_p}{\rho_b} \quad (4.4)$$

where ρ_p and ρ_b represent the density of powder and bulk materials, respectively. The density of the bulk composite material can be calculated using the following equation:

$$\rho_b = \sum_{i=1}^{n} \rho_i \gamma_i \quad (4.5)$$

where ρ_i and γ_i denote the density and volume of component i, respectively. The density ρ_b of 2.75 g/cm^3 is found when the composite powder comprises 96 vol.% Al and 4 vol.% Al_2O_3. The density of the powder ρ_p can be evaluated by the apparent density, which is roughly 1.65 g/cm^3. Thus, the porosity of the powder bed is calculated to be 40%, which is in agreement with the findings of Dong et al. (2009), who suggested that the porosity can evolve from 50% (initial powder bed) to the minimum value of 0 (fully dense material) during the laser sintering process.

Using a thermal physics module is necessary because SLM involves a phase-change process; this type of thermal analysis is thus a nonlinear transient analysis and a number of thermophysical properties should be determined for the simulation. In order to analyse the phase transformation, the latent heat should be considered: this represents the heat energy that the system stores or releases during a phase change. To account for latent heat, the enthalpy of the material

H' as a function of the temperature is defined: it is the integral of material density p times specific heat $c(T)$ with respect to temperature T:

$$H' = \int pc(T)dT \qquad (4.6)$$

Other thermophysical properties to consider include the density and thermal conductivity of the powder bed, which can be expressed as (Thummler and Oberacker 1993):

$$k_p = k_b(1 - \varphi') \qquad (4.7)$$

where k_p and k_b denote the thermal conductivity of the powder bed and bulk materials, respectively; Φ' is the porosity of the powder bed. Typical solid thermophysical properties of Al and Al_2O_3 are shown in Figure 4.1.

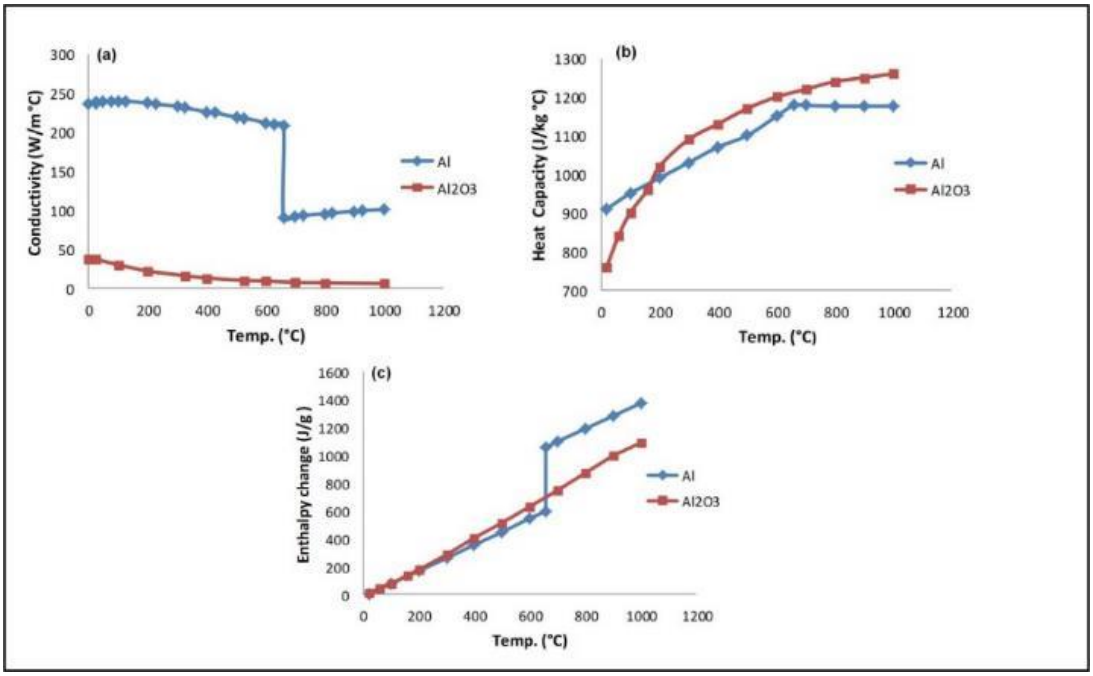

Figure 4.1: Thermophysical properties of Al and Al_2O_3 with temperature (Hatch 1984).

This study used the ANSYS Multiphysics finite element package to build the first layer's scanning model and to conduct the heat transfer simulation. The 3D finite element model that was developed does not rely on 2D assumptions. Figure 4.2 shows the model and the scanning strategy used in scanning the first layer. A rectangular composite powder layer of 5 x 1 x 0.03 mm was built on a 5 x 1 x 0.12 mm Al substrate. The nearly spherical ball-milled composite powder offered around 40% porosity, which was considered when defining the thermophysical properties during the modelling.

The composite powder layer was meshed with 0.015 x 0.015 x 0.015 mm SOLID70 hexahedron element to improve calculation accuracy; coarse mesh, in contrast, was used for the substrate. In order to reduce the simulation time, track 1 was selected to conduct the single track scanning and the first layer that was scanned was composed of three single tracks; a bidirectional scanning strategy was employed to conduct the simulation in the present work.

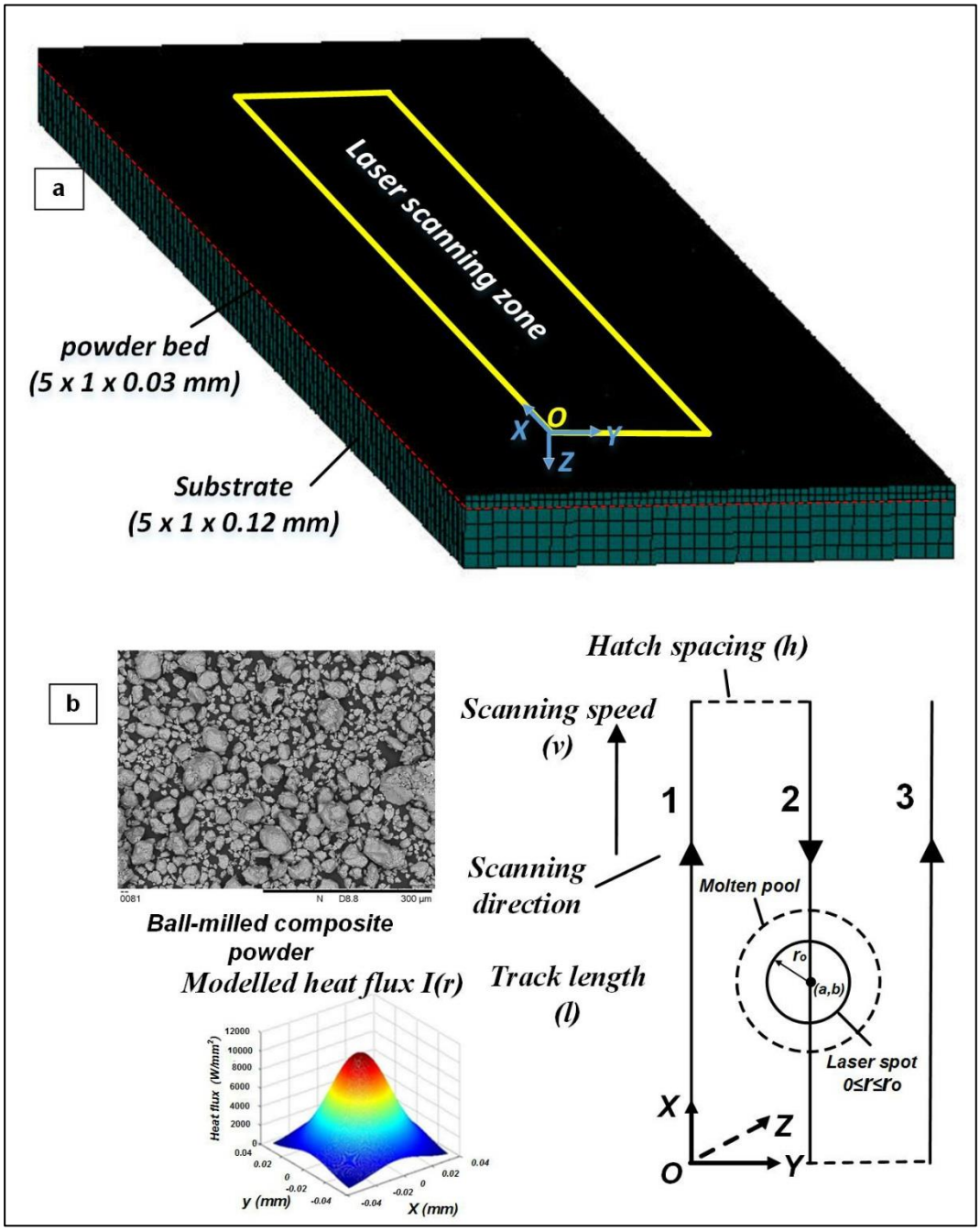

Figure 4.2: 3D finite element model and scanning strategy

The heat flux *I(r)* followed a Gaussian distribution (equation (4.2)); the laser radial distance *r* can be expressed as:

$$r = \sqrt{(X-a)^2 + (Y-b)^2} \qquad (0 \le r \le r_0\ ) \qquad (4.8)$$

where variables *a* and *b* can be determined as:

$$(a,b) = \begin{cases} (vt-(n-1)l,(n-1)h) & (n = 1,3,5,\dots) \\ (nl-vt,(n-1)h) & (n = 2,4,6,\dots) \end{cases} \qquad (4.9)$$

where *v* and *t* denote the scanning speed and scanning time, respectively; n and l represent track number and track length, respectively, and h is the hatch spacing. When three tracks are simulated, the variables a and b can then be determined as:

$$(a,b) = \begin{cases} (vt,0) & (0 \le t \le \frac{l}{v}) \\ (2l-vt,h) & (\frac{l}{v} < t \le \frac{2l}{v}) \\ (vt-2l,2h) & (\frac{2l}{v} < t \le \frac{3l}{v}) \end{cases} \qquad (4.10)$$

In terms of equation (4.2), the heat-flux magnitude strongly depends on the laser power and powder absorptivity. More specifically, the heat-flux magnitude is linearly correlated with employed laser power and absorptivity; Figure 4.3 shows the heat flux magnitude as a function of laser power when the absorptivity was fixed at 8.76%, the heat-flux magnitude was around 4.6 GW/m^2 when the laser power was relatively low, at 100 W; the heat flux magnitude increased to 6.9 GW/m^2 when the laser power increased to 150 W; a 9.2 GW/m^2 heat-flux magnitude was reached when the laser power was increased to 200 W.

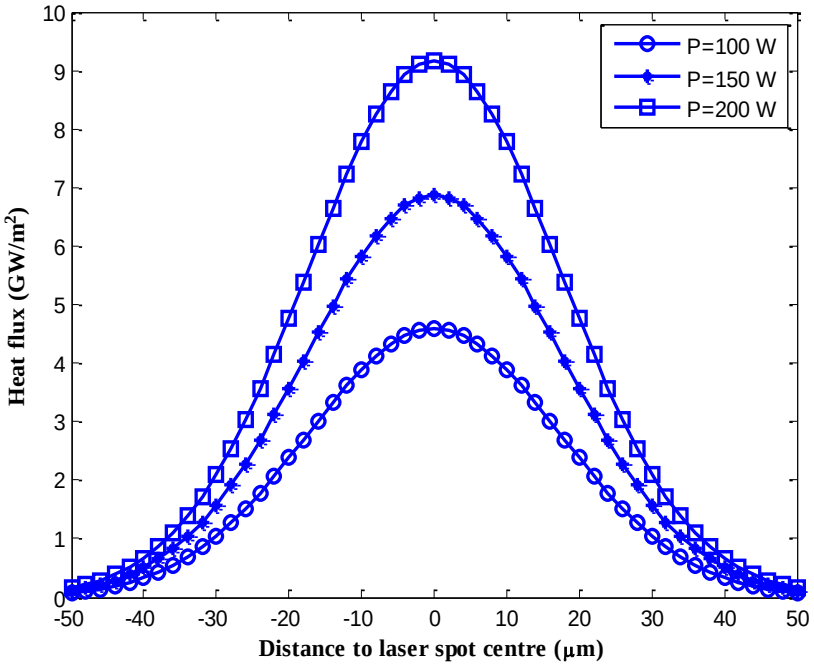

Figure 4.3: Heat-flux magnitude with laser power

Due to the laser scanning-induced temperature gradient in the powder bed, heat transfer occurred via convection between the powder bed and the ambient environment. The ambient temperature was maintained at 20°C; the convective heat transfer coefficient (*H*) can be expressed in *Z* direction, as follows:

$$-k_p \frac{\partial T}{\partial Z} = H(T_s - T_a) \qquad (4.11)$$

where k_p is thermal conductivity and $T_s \; and \; T_a$ denote the powder bed surface temperature and ambient temperature, respectively. In general, *H* is set as 10 W/m$^{2^\circ}$C in finite element simulation (Hussein et al. 2013). Both the heat flux and thermal-convection loads should be applied on the top surface of the composite powder layer; in order to prevent heat flux from overriding the applied convection

load, it is necessary to create surface effect elements. Thermal convection was thus applied on the surface effect elements, and the heat flux was applied on the powder layer surface. The simulation parameters that are chosen to simulate the scanning of the first layer's composite powders are shown in Table 4.1.

Table 4.1: Finite element simulation parameters.

Parameters	**Value**	**Parameters**	**Value**
Absorptivity, *A*	8.76%	Convective heat transfer coefficient, *H*	10 W/m^2°C
Powder bed thickness, *d*	30 μm	Laser power, *P*	100, 150, 200 W
Laser spot radius, r_o	35 μm	Scanning speed, *v*	100–1000 mm/s
Ambient temperature, T_a	20°C	Track length, *l*	4 mm
Number of tracks	3	Hatch spacing, *h*	70,100 and 130 μm

4.2 Thermal Behaviour Prediction

It is important to scan the first layer, as doing so not only determines the subsequent layers' coating behaviour but also affects the dimensional accuracy and mechanical properties of the final parts. The properties of a part produced by this process therefore depend strongly on the quality of the first layer, because that layer determines the nature and shape of the molten pool. Gaining an understanding of the thermal behaviour during the scanning of the first layer is crucial for engineers in order to optimise the laser strategy and to improve component quality using SLM.

4.2.1 Maximum Temperature Distribution

The transient temperature distribution changes rapidly with time during the scanning of first layer. When the powder layer is fixed, the laser power and scanning speed are two main parameters that determine the temperature distribution during the scanning. Combinations of different levels of laser power (100, 150 and 200 W) and scanning speeds (100-1000 mm/s) were employed to study the maximum temperature variation of every recorded points on the three tracks. Figure 4.4 shows the temperature variation of the three tracks with respect to scanning speed under a fixed 200 W laser power and 70 µm hatch spacing.

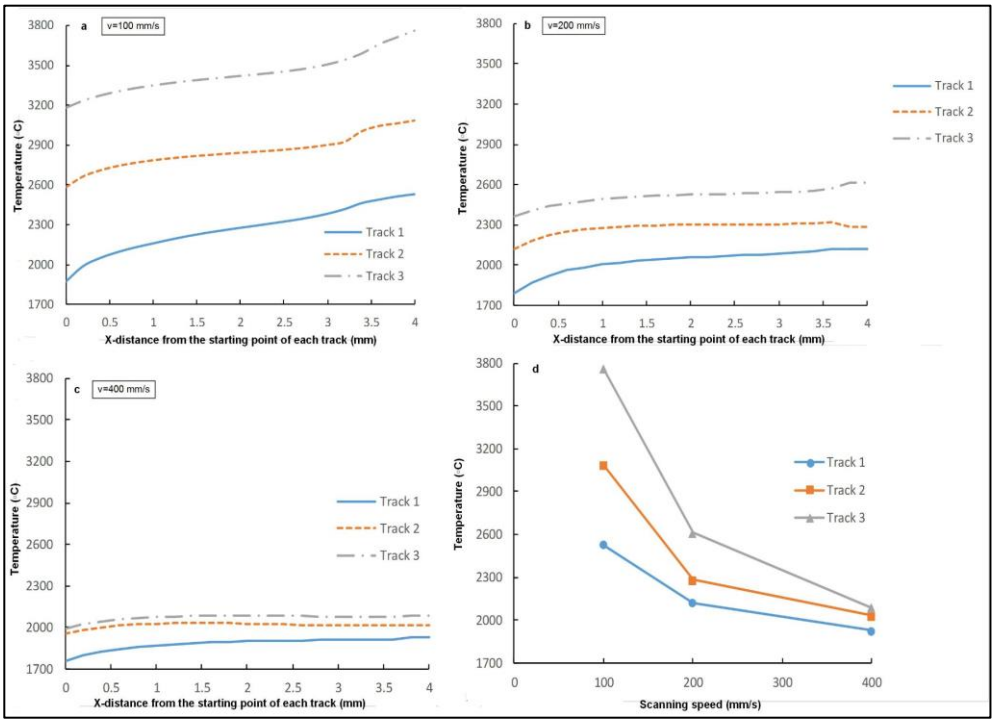

Figure 4.4: Maximum temperature distribution of the first layer using 200 W laser power with different scanning speeds: (a) 100 mm/s, (b) 200 mm/s, (c) 400 mm/s and (d) maximum temperature on three tracks in relation to scanning speed.

More specifically, Figure 4.4a shows the maximum temperature distribution under a 100 mm/s scanning speed; the temperature demonstrated a gradual increase along the scanning route due to the high thermal conductivity of Al and heat accumulation. The relatively long laser irradiation time induced by the slow scanning speed gave rise to around 600 ºC increase in temperature between two adjacent tracks. The maximum temperature that is induced by the laser irradiation should be greater than the melting point of the composite powder in order to fully melt the deposited powder and minimise the defects. When the maximum temperature was greater than the boiling point (2470 ºC for Al), however, the strong evaporation would be associated with recoil pressure that was applied on the molten pool surface. The recoil pressure, together with Marangoni convection could result in the spatter and porosity within the solidified parts.

Figure 4.4b-c, in contrast, shows the maximum temperature distribution when the scanning speed was increased to 200 mm/s and 400 mm/s, respectively. The predicted temperature variation shows similar trend to that of 100 mm/s scanning speed; however, the predicted maximum temperature at each track tended to be stable when it reached the peak along the scanning route under the 200 mm/s and 400 mm/s scanning speed; this can also be explained by the high thermal conductivity of Al powder bed. Figure 4.4d shows the correlation between maximum temperature at each track and employed scanning speed. One can see that when the scanning speed was fixed, the maximum temperature at track 3 was greater than that of track 2 and 1; this trend tended to be more obvious when relatively low scanning speed was used. As for

each track, the reached maximum temperature decreased with an increase in scanning speed because of the reduction in heat energy input.

In order to investigate the influence of laser power on maximum temperature, Figure 4.5a shows the maximum temperature at track 1 with respect to laser power, while the scanning speed was fixed at 200 mm/s. Track 1 was chosen because track 2 and 3 demonstrated much higher maximum temperature due to the heat accumulation and thermal conductivity (see Figure 4.4). In order to produce full dense parts and ensure the dimensional accuracy, the employed process parameters that can fully melt track 1, are considered to fully melt the rest of the tracks.

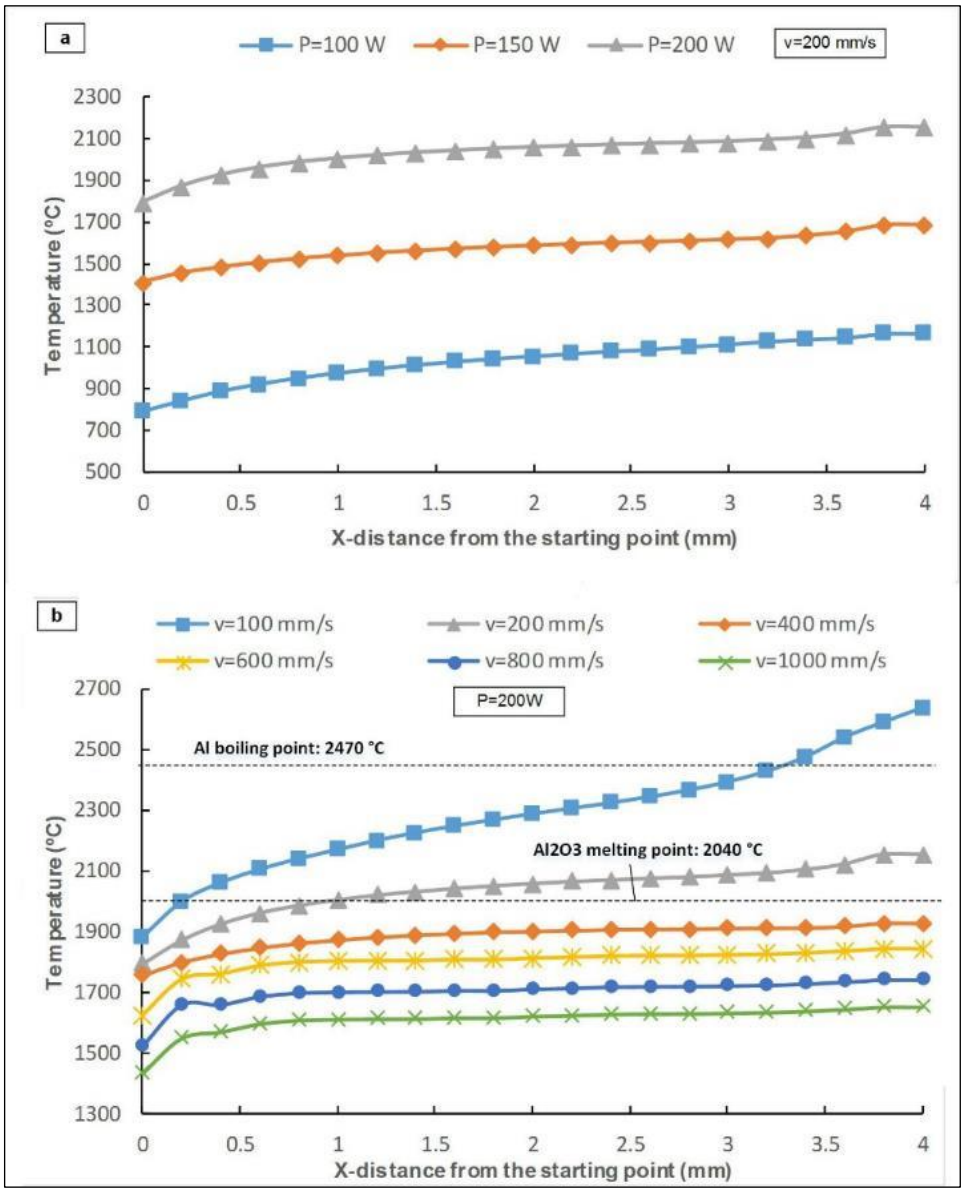

Figure 4.5: Maximum temperature at the scanning track 1 with (a) fixed scanning speed 200 mm/s and (b) fixed laser power 200 W.

It can be seen that the maximum temperature increased slightly with the continued scanning along the tack because of the heat accumulation and thermal conductivity; a maximum temperature at the end of the track reached around 1150 ºC when the laser power was 100 W. The overall maximum temperature

increased by 500 ºC as the laser power increased by 50 W, this is because within the same exposure time, a higher laser power generates more heat energy input. It should be noted that the predicted maximum temperatures under the laser power of 100 W and 150 W were less than 2040 ºC during the single-track scanning, which means the added nano Al_2O_3 particles cannot be fully melted and surface porosity and microcracks could be further generated.

Figure 4.5b, in contrast, shows the maximum temperature distribution at track 1 when laser power was maintained at 200 W. When a relatively low scanning speed (100 mm/s) was used, the predicted maximum temperature at all scanning points were greater than 2040 ºC (except the first recorded point) due to a relatively strong laser energy input induced by long exposure time. Furthermore, the maximum temperature increased with the continued scanning because of the heat accumulation. When the scanning speed increased to 200 mm/s, the predicted maximum temperature showed a slight increase along the scanning route, however, the increase rate was much slower compared to the 100 mm/s scanning speed. It can thus be concluded that, due to the heat accumulation, the predicted maximum temperature showed an increase along the scanning route and the trend become more obvious at low scanning speed. The simulation results also show that the generated temperature on powder bed was less than 2040 ºC when the scanning speed was greater than 400 mm/s, implying partial melting and porosity defects within the fabricated parts. The maximum temperature induced by the laser irradiation needs to be higher than melting point of powder bed in order to fully melt both Al matrix and Al_2O_3 reinforcement and further produce full dense part. Therefore, the range of

scanning speed for laser energy density and scanning speed optimisation was chosen to be 100–600 mm/s when fabricating bulk composite samples in order to save experimental cost.

In addition to the maximum temperature distribution, temperature variation of every point with respect to scanning time is another factor that affects the quality of the solidified track, because the cooling rate determines the level of microstructure refinement and further influences the mechanical properties of the final parts. The midpoint at track 1 was chosen to analyse the temperature variation in relation to different levels of laser power and scanning speed.

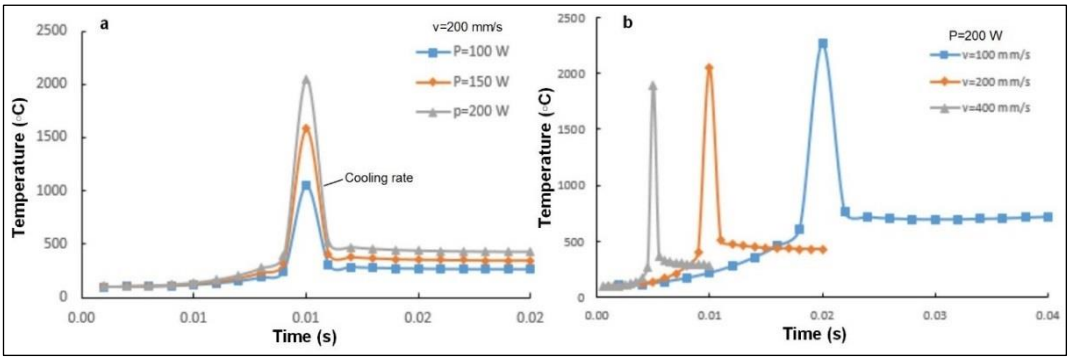

Figure 4.6: The temperature variation with time at the midpoint of the track 1: (a) with fixed scanning speed at 200 mm/s, (b) with fixed laser power at 200 W.

The scanning speed in Figure 4.6a was fixed at 200 mm/s and all temperature peaks occurred at 0.01 s but reached different values because of different heat energy inputs induced by different laser power. The curve slope presents the cooling rate, which rises from 7.4 x10^5 ºC/s to 1.54 x10^6 ºC/s when the laser power increased from 100 W to 200 W. Furthermore, the predicted maximum temperature increased from 1046 ºC to 2050 ºC. Figure 4.6b, in contrast, shows the temperature variation at the midpoint when laser power was

fixed at 200 W, where scanning speed varied from 100 mm/s to 400 mm/s. Three peaks occur at different times, and the maximum temperature decreased from 2267 ºC to 1899 ºC as the scanning speed increased from 100 mm/s to 400 mm/s. With an increase in scanning speed, the composite powder liquid lifetime decreased, which resulted in an obvious increase in cooling rate from 7.5 x 10^5 ºC/s to 3 x 10^6 ºC/s. This is because a relatively higher scanning speed leads to shorter laser exposure time and insufficient laser energy input to the powder layer; they both could give rise to a low temperature and extremely short liquid lifetime.

It can thus be concluded that both the scanning speed and laser power play a crucial role in determining the thermal behaviour within SLM of Al-Al_2O_3 nanocomposite material. In terms of the simulation results, the cooling rate of molten material rises with the increase in both the laser power and scanning speed. Moreover, it implies that the cooling rate is more sensitive to the scanning speed than the laser power. On one hand, extremely short liquid lifetime and high cooling rate induced by relatively high scanning speed are in favour of the grain refinement, but on the other hand, it tends to increase the residual thermal stress and further facilitate the formation of micro cracks.

4.2.2 Molten Pool Dimensions

When the layer thickness is taken into account in the finite element simulation, the temperature distribution of the powder layer top surface is not sufficient to provide the thermal performance during the scanning of first layer in SLM. It would therefore be necessary to analyse the molten pool dimensions, which also

plays a crucial role in determining the layer thickness during the multi layers laser melting process. Therefore, Figure 4.7 shows the predicted molten pool temperature contours at the midpoint of the track 1, where the laser power was maintained at 200 W, while the scanning speed varied from 200 mm/s to 400 mm/s.

The dimensions of the molten pool were measured through the temperature distribution plots recorded at the instant when the laser travelled along its path of scanning. The molten pool length represents the distance along the X axis and parallel to the scanning direction, while the width is the distance along the Y axis and perpendicular the scanning direction, the molten pool depth is taken as the distance from the powder layer surface to the molten depth inside the powder bed along the Z axis.

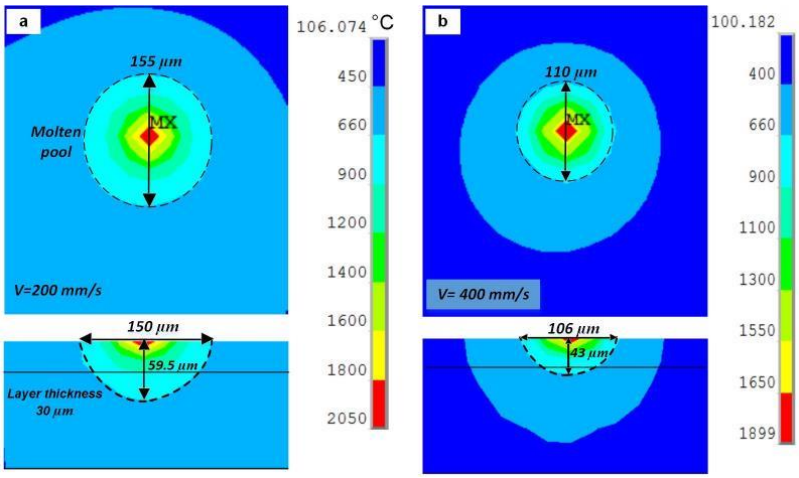

Figure 4.7: Predicted molten pool dimensions at the midpoint of the track 1 with a fixed laser power 200 W: (a) scanning speed at 200 mm/s, (b) scanning speed at 400 mm/s.

Figure 4.7a shows the temperature contours under the 200 mm/s scanning speed, from which three dimensions of the molten pool were measured

from both the top surface and the cross-sectional profile. The predicted molten length is very close to the width, with the size of 155 μm and 150 μm, respectively. The solid line in the cross-sectional profile denotes the interface between composite powder layer and aluminium substrate, while the dash line represents the isotherm at 660 ºC in the temperature contours. It should be noted that the measured molten pool depth is greater than the layer thickness (30 μm), which is 59.5 μm; a strong metallurgical bonding may generate between the solidified layer and the underneath plate. The temperature contours and molten pool dimensions of the midpoint under the 400 mm/s scanning speed are shown in Figure 4.7b. One can see that, very similar molten pool shapes were formed, but the dimensions are much smaller compared to that of 200 mm/s.

It may be concluded that a 200 mm/s increase in scanning speed resulted in a roughly 45 μm decrease in both molten pool length and width; the predicted molten pool length and width were 110 μm and 106 μm, respectively. The predicted 106 μm molten pool width, however, implied no metallurgical bonding between two adjacent hatches when the employed hatch spacing was greater than 100 μm. It should also be noted that the heat-affected zone under 200 mm/s scanning speed was much larger than that of 400 mm/s; this is thought to be induced by different laser energy input under different exposure times.

4.3 Experimental Validation

The simulation results from Section 4.2 indicate that the optimum laser power that can be employed amongst 100, 150 and 200 W to fully melt the composite

powder is 200 W, where the predicted maximum temperature is greater than the melting point of the nanocomposite powder. In this section, the employed laser power used in experiments is thus maintained at 200 W in order to save the experimental cost. The employed scanning speeds were less than 1000 mm/s, while the hatch spacing varied from 70 μm to 130 μm.

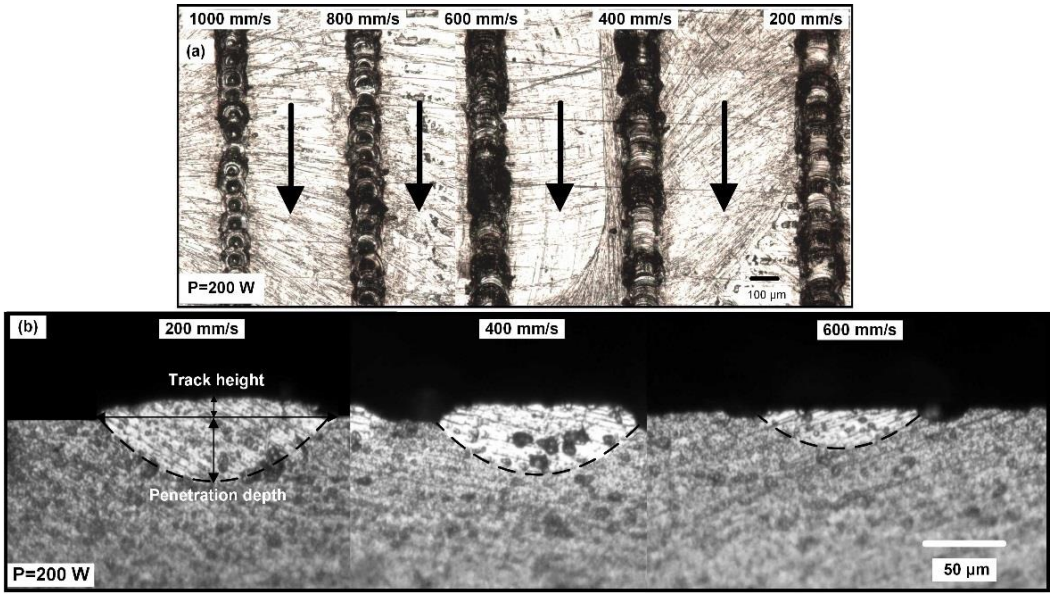

Figure 4.8: OM images showing selective laser melted tracks under the 200 W laser power: (a) top view and (b) cross section view.

Figure 4.8a shows the top view of the selective laser melted tracks with different scanning speeds from 200 mm/s to 1000 mm/s, while the layer thickness was fixed at 30 μm. One can see that the solidified track width decreased with an increase in scanning speed and this trend was more obvious when the scanning speed was greater than 600 mm/s. This situation may be induced by the laser exposure time; a relatively high scanning speed generally gives rise to a short laser exposure time and less laser energy input, which further leads to the

formation of small molten pools. It can be anticipated that the penetration depth also decreases with an increase in scanning speed. Figure 4.8b thus shows the cross section view of the scanned tracks with the scanning speeds varying from 200 mm/s to 600 mm/s. The cross sections of 800 mm/s and 1000 mm/s scanning speeds produced tracks are not shown in this figure, because the measured molten pool depth of the two tracks were very small. One can see that, with an increase in scanning speed from 200 to 400 mm/s, the measured penetration depth decreased from around 38.2 µm to 19.4 µm. These experimental values are considered to be consistent with the predicted depth, shown in Figure 4.7, which was found to be 29.5 and 13 µm, respectively.

This finding shows agreement with the simulation in Section 4.2 that the dimensions of predicted molten pool decrease with an increase in scanning speed when laser power, hatch spacing and layer thickness were constant. It should be noted that the melt track height is less than the height of the deposited layer thickness (30 µm), and it can be explained by the following two factors: first, when the powder is irradiated by the laser beam, it spreads out during the melting, so the height of the scan track will decrease alongside an increase in the width. This phenomenon is also known as wetting ability. It is believed that good wetting behaviour promotes the creation of good metallurgical bonding with the substrate and adjacent layers. With an increase in the laser power and decrease in the scanning speed, the wetting ability tends to improve. Second, due to the porosity of the powder bed, the trapped gas between the powder particles could escape the molten pool during the melting stage, implying the volume occupied will decrease after the solidification.

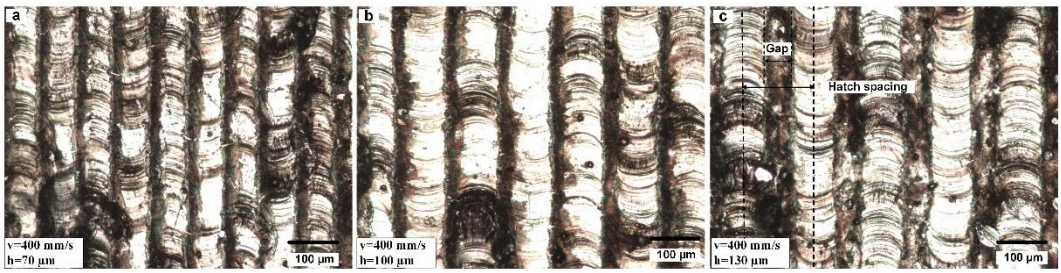

Figure 4.9: Single layer fabrication under hatch spacing of (a) 70 µm, (b) 100 µm and (c) 130 µm.

In order to investigate the effect of hatch spacing on single layer fabrication, Figure 4.9 shows the single layer fabrication under 200 W laser power and 400 mm/s scanning speed with hatch spacing varying from 70 µm to 130 µm. One can see that a hatch gap formed between two adjacent hatches when the hatch spacing was increased to 130 µm, suggesting no metallurgical bonding between the two hatches (Figure 4.9c). Therefore, in order to reduce the experimental cost, the 70 µm and 100 µm hatch spacing values would be employed to optimise the laser energy density and scanning speed when fabricating bulk composite samples using SLM.

4.4 Summary

A 3D finite element model has been developed to predict the thermal behaviour within selective laser melting of the first layer's composite; the single layer consisted of three single tracks in order to save computation time. Different combinations of process parameters such as laser power, scanning speed and hatch spacing have been employed to predict the maximum temperature distribution and molten pool dimensions.

A set of experiments on scanning of single layer have been conducted and the results indicated that the dimensions of molten pool decreased with an increase in scanning speed and this trend was more obvious when the scanning speed was greater than 600 mm/s. It has also been found that no metallurgical bonding could be built between two adjacent hatches when the hatch spacing was increased to 130 μm. In order to save experimental cost in optimising laser density and scanning speed, the range of scanning speeds used in SLM of bulk composite sample was thus limited to 100–600 mm/s; the hatch spacing was chosen to be 70 μm and 100 μm. More detail on process parameters optimisation is provided in chapter V.

Chapter V

Process Parameters Optimisation and Microstructure

This chapter addresses the third research objective of this thesis. The process parameters that are suggested by the finite element simulation in chapter IV are chosen to fabricate bulk composite samples. The optimum laser energy density and scanning speed are determined by quantifying the relative density of the as-fabricated samples in both horizontal and vertical sections. The microstructure of the sections is analysed afterwards. The chapter is organised as follows: Section 5.1 introduces the research methodology, including the material characterisation techniques and research hypotheses; Section 5.2 provides the experimental study; Section 5.3 details the results and discussion and Section 5.4 provides a summary of the chapter.

5.1 Research Methodology

In order to investigate the influences of process parameters on relative density, cubic samples (8x8x8 mm) under different conditions (scanning speed and hatch spacing) were fabricated and then both horizontally and vertically sectioned. The 8x8x8 mm sample size was chosen because this size is widely used in literature. The sectioned samples were then polished using standard techniques prior to optical microscopy (OM) observation; the relative density was evaluated by

image analysis using ImageJ software to determine the optimum process parameters.

Laser energy density (ε), which is used to quantify the laser-energy input, may be expressed as (Simchi 2006):

$$\varepsilon = \frac{P}{vdh} \tag{5.1}$$

where P and v denote laser power and scanning speed, respectively, and d and h represent layer thickness and hatch spacing, respectively.

For the microstructure analysis, the samples were etched using Keller's reagent for 30 s (190 ml distilled water, 5 ml HNO_3, 3 ml HCL, 2 ml HF) prior to the OM and SEM inspection. Phase identification of the samples was performed using X-ray powder diffraction (XRD) with Co kα (λ = 1.789 Å) radiation at 35 kV and 40 mA in continuous-scan mode. Cold-working was performed because it is capable of improving the components' strength; the cold-working process was performed on both horizontally and vertically sectioned samples at room temperature using a universal testing machine (Autograph AG-1 20 KN, Shimadzu, Kyoto, Japan) with a compressive strain rate of 0.5 mm/min until the strain reached 40%.

The research hypotheses of the study include:

i. The relative density may increase with an increase in the scanning speed and laser-energy density until the optimum values; the relative

density then decreases when the scanning speed and laser-energy density exceed the optimum values.

ii. Due to the rapid cooling, a fine microstructure is expected to be formed in the as-fabricated samples. The cold-working may result in grain deformation and elongation by plastic deformation, and further change the microstructure of the samples.

5.2 Experimental Study

A Renishaw AM250 (Renishaw Plc, Wotton-under-Edge, Gloucestershire, UK) SLM system that employs a modulated ytterbium fibre laser with a wavelength of 1,071 nm was used to fabricate tensile and cubic samples; the nominal diameter of the focussed laser spot is 70 µm. The as-fabricated 8 x 8 x 8 mm cubic samples were vertically and horizontally sectioned using the YZ and XY planes to investigate the effect of process parameters on the porosity distribution and to determine the optimum process parameters (Figure 5.1).

Because the laser that was employed uses discrete point exposures instead of running continuously, the equivalent scanning speed may be determined by:

$$v = \frac{l_p \cdot v_l}{l_p + v_l \cdot t_e} \tag{5.2}$$

where l_p and t_e denote the point distance and exposure time, respectively; v_l represents the laser's moving speed between two adjacent points; it remains fixed at 5,000 mm/s (Figure 5.1b). As shown in Figure 5.1c, a bidirectional

scanning strategy with a striped fill-hatch-type scanning was employed for this study; the rotation angle between each adjacent layer was set to 67° to eliminate the chance of scan lines repeating themselves directly on top of one another, thus creating poor material properties.

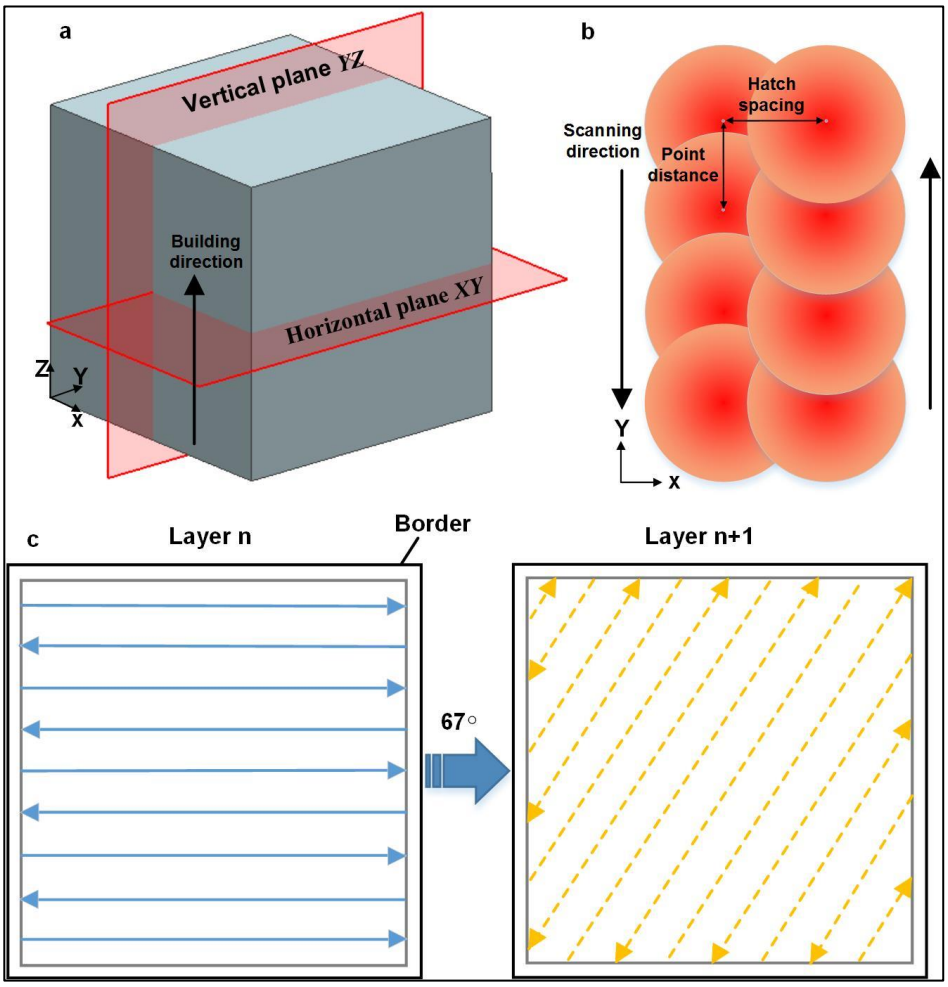

Figure 5.1: Schematic diagram of (a) section strategy for cubic sample; (b) laser working mode; (c) laser scanning strategy for multiple layers.

The synthesised composite powder was placed to dry in a furnace set at 100°C for 24 h under argon atmosphere. The process parameters used in the study are shown in Table 5.1.

Table 5.1: Process parameters

Parameters	**Value**
Laser power, P	200 W
Layer thickness, d	30 µm
Substrate temperature, T_o	170°C
Point distance, l_p	80 µm
Hatch spacing, h	70, 100 µm
Scanning speed, v	100, 150, 200, 300, 400, 600 mm/s

5.3 Results and Discussion

This section details the results and discussion, including the process parameters optimisation by evaluating the relative density, phase identification and microstructure as well as relevant discussion.

5.3.1 Process Parameters Optimisation

Figure 5.2 shows the relative density of the as-fabricated samples in relation to laser energy density and scanning speed when laser power and layer thickness were maintained at 200 W and 30 µm, respectively.

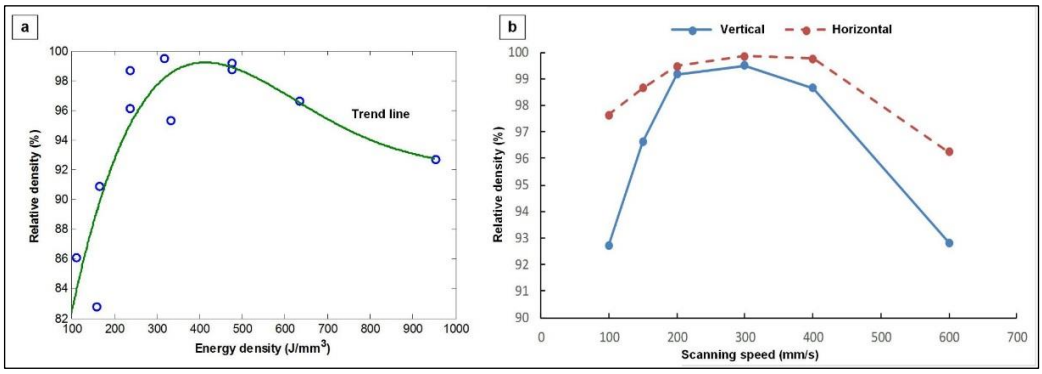

Figure 5.2: Relative density in relation to (a) laser-energy density and (b) scanning speed.

Figure 5.2a shows the correlation between the laser energy density and the relative density of the as-fabricated vertically sectioned composite samples. The relative density increases with an increase in the laser-energy density up to 317.5 J/mm^3, at which point the calculated relative density reached 99.49%; the relative density decreased with an increase in the energy density afterwards. Variations in the laser energy density are generally caused by the scanning speed; as Figure 5.2b shows, the relative density thus varied as a function of the scanning speed in both the vertically and horizontally sectioned samples when the hatch spacing was maintained at 70 µm. The relative density of both the vertically and horizontally sectioned samples reached their maximums (99.49% and 99.85%, respectively) at a scanning speed of 300 mm/s (Han et al. 2017b).

When the scanning speed was greater than this threshold, however, the relative density decreased with an increase in scanning speed. This situation could be explained by the fact that more heat energy was dispersed to the powder bed due to the high thermal conductivity of Al. In addition, because less

heat energy accumulated at high scanning speeds, the accumulated heat energy was insufficient to fully melt the composite powder.

The decrease in the relative density also may have been caused by the reduction of the scanning speed when the scanning speed that was employed was lower than the threshold. This situation may be explained by the laser's working-mode transition from conduction to keyhole mode, because a decrease in the scanning speed generally resulted in a dramatic increase in laser energy density when the scanning speed was below the threshold. It should be noted that the overall relative density of the horizontally sectioned samples was higher than that of the vertically sectioned samples at each of the scanning speeds that were employed; this is thought to have been caused by the building direction (see Figure 5.1).

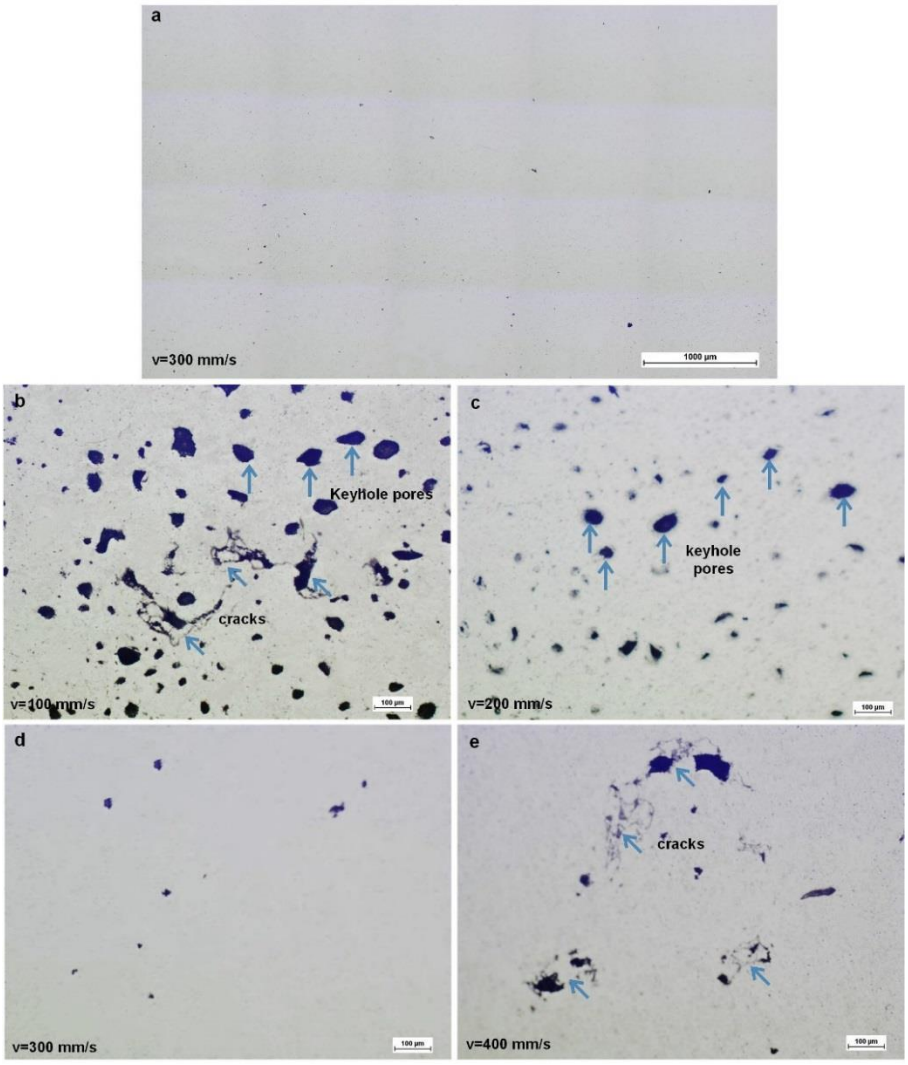

Figure 5.3: Optical microscopy (OM) images showing porosity development with scanning speeds of (a) elongated sample at 300 mm/s; (b) 100 mm/s; (c) 200 mm/s; (d) 300 mm/s; (e) 400 mm/s.

The microstructure and porosity distribution of the vertically sectioned samples under different scanning speeds are shown in Figure 5.3. Figure 5.3a shows the porosity distribution of the elongated sample fabricated at 300 mm/s; a very small number of metallurgical pores and keyhole pores were formed under this process condition. Figure 5.3b–e show typical microstructure and porosity

distribution when the scanning speed varied from 100 mm/s to 400 mm/s. Both cracks and keyhole pores were generated in the samples fabricated at 100 mm/s and 400 mm/s, but only keyhole pores were observed in the sample under 200 mm/s; this situation may be attributable to the laser energy density variation and the poor wettability of the Al_2O_3 particles under different scanning speeds.

5.3.2 Phase Identification and Microstructure

Figure 5.4 shows the XRD patterns of the composite powder ball-milled for 20 h and the as-fabricated composite sample fabricated at 300 mm/s. The diffraction patterns exhibit typical Al peaks, which suggests that contamination elements (e.g. iron) were not present or were below detectable levels in both the high-energy ball milling and SLM processes. It should be noted that the patterns of the Al_2O_3 powder were not detected in the XRD patterns, which is thought to have been induced by the relatively low-volume percentage of Al_2O_3 (4 vol.%) that was added in the Al matrix. Compared to the standard patterns of commercial pure Al, however, the peaks of the two composite samples exhibited a slightly horizontal offset. This can be explained by the fact that the Al_2O_3 reinforcements were embedded in the Al matrix, which also broadened the peaks of the composite samples.

Furthermore, in terms of the Scherrer equation, the term ‘full width at half maximum’ (FWHM) refers to the grain size of the measured samples (Choi et al. 2008). In general, a larger FWHM value indicates a smaller grain size. The measured FWHM of the as-fabricated composite sample was found to be 0.4723,

which was a greater value than that of the composite powder (0.3149). This indicates that fine grains were formed in the as-fabricated composite samples because of the very high cooling rate that occurs with the SLM process.

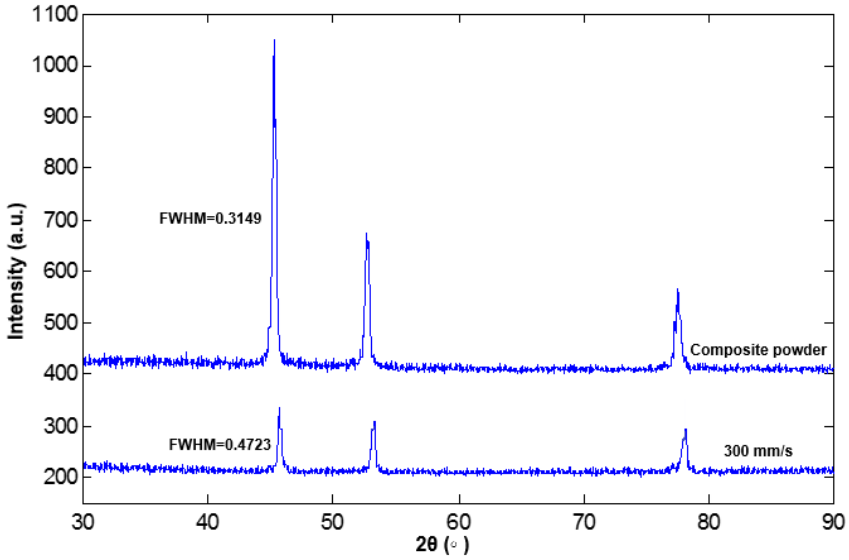

Figure 5.4: X-ray diffraction (XRD) patterns of the composite powder and as-fabricated composite sample fabricated at 300 mm/s.

Figure 5.5 shows the microstructure of the as-fabricated and cold-worked composite samples fabricated at 300 mm/s. Figure 5.5a (1–3) shows the microstructure of the as-fabricated horizontally sectioned sample with three different magnifications. The molten pool tracks after solidification were clear and intact without obvious porosity present, thus implying that Al_2O_3 particles showed good wetting ability and that dense parts could be produced under the process parameters that were employed. The as-fabricated sample showed a granular microstructure; the microstructure was considered to be that of Al caused by the rapid solidification due to the laser irradiation, as reported in literature (Kimura et al. 2017). Furthermore, the microstructure at the molten pool region showed

different development; in that case, a relatively fine microstructure was observed within the molten pool as compared to the coarse microstructure found at the boundary regions of the molten pool (Figure 5.5a-2, 3).

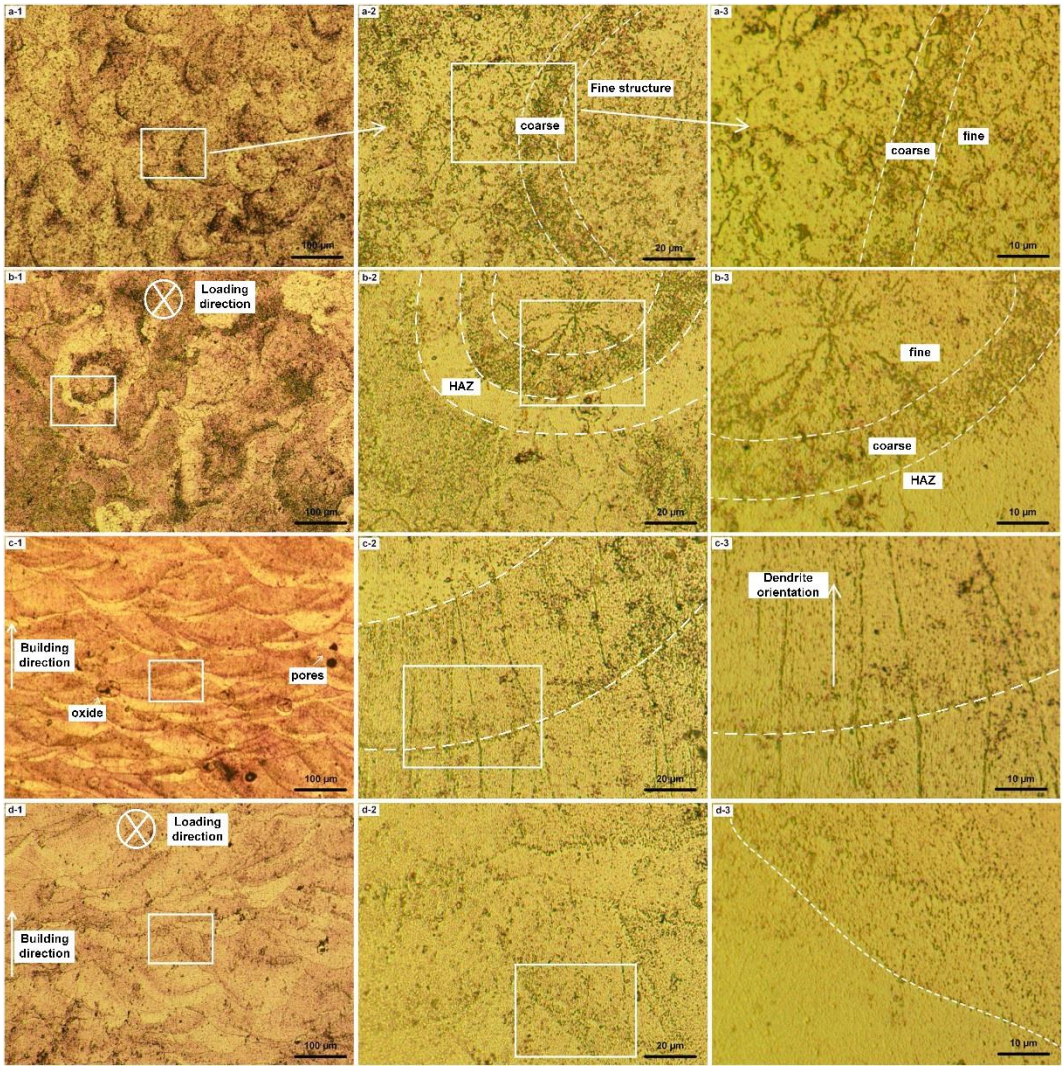

Figure 5.5: OM images showing the microstructure of composite samples fabricated at 300 mm/s: (a1–a3) as-fabricated horizontal section; (b1–b3) horizontal section after cold working (loading direction indicated); (c1–c3) as-fabricated vertical section; (d1–d3) vertical section after cold working (loading direction indicated).

The microstructure of the cold-worked horizontal section is shown in Figure 5.5 b(1–3). Compared to the as-fabricated sample, cold working tended to close the porosity by deforming the solidified molten pool profile. Furthermore, the grains became deformed and elongated due to the plastic deformation; this contributed to an improvement in strength because of the entanglement of dislocations with grain boundaries and with one another. Both relatively fine and coarse microstructures were also observed at the molten pool region.

It should be noted that a heat-affected zone (HAZ) around the molten pool in the previously deposited layers was also clearly visible. This finding shows agreement with the work of Thijs et al. (2013); their study found that a transition from a fine to a coarse cell structure formed during the SLM of an Al alloy.

Figure 5.5c (1–3) shows the microstructure of an as-fabricated vertically sectioned composite sample. The formation of semi-circular molten pools was attributable to the Gaussian-distributed heat flux. Molten pools were present at a certain angle, which is thought to have been induced by the rotation angle (67°C) between each adjacent layer; the layering was done to eliminate the chance of scan lines repeating themselves directly on top of one another. A good metallurgical bonding between two adjacent layers was thus formed under this condition, though some open pores and oxides still remained (Figure 5.5c–1).

It should be noted that columnar grains were formed and grew along the building direction – or rather they grew along the positive temperature gradient (Figure 5.5c 2–3). The microstructure of the cold-worked vertical section is shown in Figure 5.5d (1–3), which shows the effect of cold working on the microstructure

change. This was similar to the microstructure at the horizontal section: that is, the semi-circular molten pools at the vertical section tended to be deformed and close porosity due to severe plastic deformation. The columnar and dendrite microstructures, however, were observed to be reduced greatly compared to the microstructure at the as-fabricated vertical section (Figure 5.5c 2–3). This is thought to have been induced by the cold-working process: since the direction of the compression force that was employed was perpendicular to the vertical section, the grains tended to become deformed and elongated when subjected to plastic deformation. The columnar and dendrite microstructures were thus broken, which contributed to the entanglement of dislocations with grain boundaries and with one another (Figure 5.5d 2–3).

Figure 5.6 shows the back-scattered SEM micrographs of as-fabricated and cold-worked samples; these images are useful for further investigation of the microstructure change. The distribution of Al_2O_3 particles is shown in Figure 5.6a-1. The energy-dispersive X-ray spectroscopy (EDS) mapping indicates that the Al and O contents at the measured surfaces were 98.4 wt.% and 1.6 wt.%, respectively (Figure 5.6a 2–3). The measured O content was lower than the theoretical weight percentage of O 2.66 wt.% (Han et al. 2016), which may be explained by two factors. First, the EDS element analysis is a semi-quantitative analysis, which means that it can only measure the element content at the sample surface rather than the bulk sample; second, due to the oxidation that occurs, a very thin oxide film (roughly 3 nm) was formed on the sample surface.

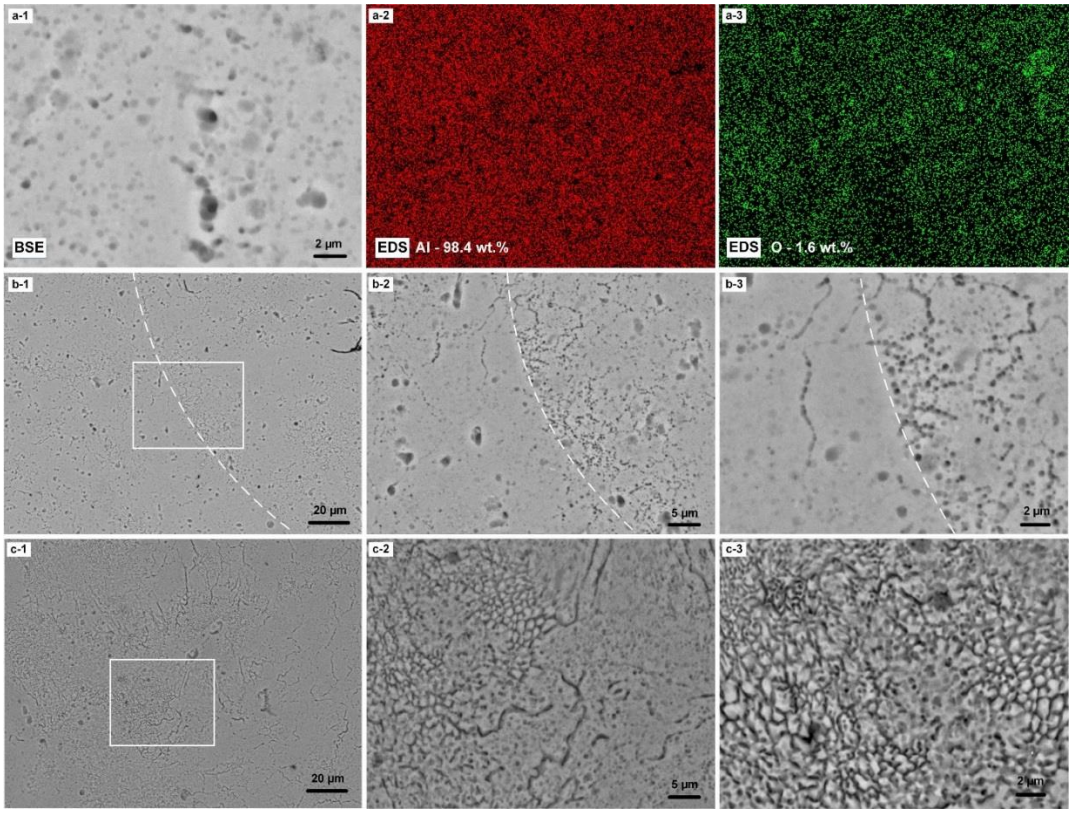

Figure 5.6: Back-scattered SEM micrographs showing (a) uniform distribution of Al_2O_3 reinforcement in Al matrix (via energy-dispersive X-ray spectroscopy [EDS]); (b) as-fabricated horizontally sectioned sample; (c) cold-worked horizontally sectioned sample.

The back-scattered SEM micrograph, together with the EDS mapping, confirmed that the Al_2O_3 particles were distributed relatively uniformly amongst the Al matrix, though a few agglomerates did remain. The microstructure shown in Figure 5.6b shows agreement with the observation shown in Figure 5.5a that both granular grains and dendrite microstructures were formed because of the rapid solidification and thermal gradient. The microstructure subjected to plastic deformation is clearly shown in Figure 5.6c; the deformed and elongated grains became entangled with one another, which contributed to strength alteration.

5.3.3 Discussion

This investigation demonstrated that the microstructure formed was non-uniform at the molten pool region (Figure 5.5). This microstructure is thought to have been induced by the temperature gradient during the laser irradiation. The temperature at the boundary regions was much lower than that inside the molten pool, because the heat flux that was employed followed a Gaussian distribution. During the solidification process, the cooling rate inside the molten pool was thus more rapid than in the boundary regions. A previous study has shown that rapid cooling produces smaller grains, whereas slow cooling produces larger grains (Kalpakjian and Schmid 2014); in the current study, both fine and coarse microstructures formed at the molten pool regions. Within single-layer processing, another factor that can contribute to the formation of non-uniform microstructure is the remelting process, which occurs between any two adjacent discrete point exposures when the laser beam is in motion. In addition, due to the hatch overlap, the boundary regions of the molten pools also melted twice, and the grain grew along the positive temperature gradient to form a non-uniform microstructure.

Generally, during the SLM process, the powder layer is irradiated and the induced heat energy is transferred from the surface of a deposited powder layer to the solidified layers underneath; columnar grains form during the solidification process due to the temperature gradient within the molten pool. In the present study, the grains that formed in the solidified layers underneath also grew along the temperature gradient and further formed columnar grains because of the heat conduction and remelting process; dendrite microstructures were thus formed

(Figure 5.5c 2–3). This finding shows agreement with the literature (H. Zhang et al. 2016; Song et al. 2014), in which columnar grains have also been observed when SLM is used to process Fe and Al alloys.

5.4 Summary

The optimum laser energy density and scanning speed have been determined by evaluating the relative density of the as-fabricated composite samples. The transition of laser working mode from conductive to keyhole-mode is thought to be the primary factor that causes the formation of pores when relative slow scanning speeds were employed.

The phase of Al_2O_3 has not been detected in the as-fabricated composite samples due to the relatively low volume percentage (4 vol.%). The hypothesis was validated that a fine granular-dendrite microstructure of the as-fabricated composite samples was formed due to the rapid cooling within SLM; the columnar microstructure along the building direction is attributed to the thermal gradient at the molten pool region. Further, the influence of cold working on microstructure change was also examined; the grains were found to be deformed and elongated due to plastic deformation, which may contribute to the alteration of mechanical properties of the fabricated samples. The cold-worked parts are expected to find applications in which improved hardness and strength are required. More detail on the investigation of mechanical properties are discussed in next chapter.

Chapter VI

Mechanical Properties Investigation

This chapter addresses the fourth research objective of this thesis. It studies the tensile behaviour, microhardness, macro and nanoscale friction and wear behaviour of the fabricated samples. The chapter is organised as follows: Section 6.1 offers the research methodology, including the employed techniques and research hypotheses. Section 6.2 provides the experimental study; Section 6.3 and Section 6.4 detail the results and discussion, respectively. Section 6.5 summaries this chapter.

6.1 Research Methodology

In order to investigate the mechanical properties of the fabricated samples, several advanced testing and analytical techniques are employed. The tensile specimens were fabricated horizontally and their dimensions were determined according to ASTM-E8 / E8M-13a (Anon n.d.). The cubic samples (8x8x8 mm) that were used for microstructure analysis in chapter 5 were also used for microhardness investigation to explore the influences of microstructure change on mechanical property alteration.

The pin-on-disc dry sliding test was performed to study the macro wear behaviour of the fabricated samples to explore the influences of Al_2O_3

reinforcement on friction and wear behaviour. The indicator that is used to evaluate material's wear behaviour is material wear rate (ω), which may be expressed as:

$$\omega = \frac{V_\Delta}{N \cdot L} \qquad (6.1)$$

where V_Δ denotes the volume loss of the specimen; N and L represent the applied normal load and sliding distance, respectively. V_Δ may be determined by:

$$V_\Delta = \frac{W_\Delta}{\rho} \qquad (6.2)$$

where W_Δ denotes the weight loss of specimen after the wear test, while ρ is the density of the specimen.

The development of SLM has led to composite materials finding more applications in aerospace and automotive industries. Recently, interest has emerged with regard to using SLM to manufacture micro-electromechanical systems (MEMS) (Clare et al. 2008) such as MEMS gyroscopes that are widely used in modern cars and planes. The wear behaviour may be a significant determiner of their life and performance; due to the length scale limitation, the macro wear test (e.g. pin-on-disc testing) is inapplicable to study the wear behaviour however, the nanoscale wear test (e.g. AFM nanoscratching) is thereby employed to study the nanoscale wear behaviour in order to predict and improve the life and performance of the MEMS gyroscopes. AFM tip-based nanoscratching was also used to examine the influences of pores that were

formed within SLM on the nanoscale friction and wear behaviour under different loads.

The research hypotheses within the study of mechanical properties include:

i. Both tensile strength and microhardness of the nearly full-dense composite samples are higher than the pure Al samples because of the added reinforcement.
ii. Cold working induced grain deformation and elongation (observed in chapter 5) may contribute to the microhardness alteration.
iii. Due to the addition of Al_2O_3 reinforcement, the macro wear performance of the composite samples is expected to be better than pure Al.
iv. The pores that are formed within SLM could influence the friction coefficient distribution during the AFM nanoscratching.

6.2 Experimental Study

The tensile tests were carried out at room temperature using a Zwick/Roell tester with a strain rate of 0.3 mm/min. Vickers microhardness tests were performed using Innovatest (Maastricht, Netherlands) with a 100 g load and 10 s dwell time. An in-house developed pin-on-disc tribometer was used to conduct the macro wear test at room temperature. The applied normal load was set to be 1N for the as-fabricated composite and pure Al samples. The rotation diameter, sliding speed and sliding time were set at 7 mm, 25 rpm and 30 min, respectively.

A commercial AFM instrument (Park Systems XE-100, Suwon, South Korea) equipped with a pyramidal diamond tip (DNISP, Veeco Inc., USA; tip radius < 40 nm) was used to scratch the polished composite sample at room temperature. The ambient environment was temperature controlled, which was 21±0.5 ºC, and the humidity was measured using the rotronic HYGROLOG hygrometer (Crawley, West Sussex, UK), which was 43.2±1.3%. The spring constant of the cantilever as specified by the manufacturer was 221 N/m. The scratching speed was fixed at 2 µm/s, using different normal loads (ranging from 10 µN to 40 µN) in order to investigate the influence of the keyhole pores and nano Al_2O_3 reinforcement on the friction coefficient and material-wear rate of the as-fabricated SLM components.

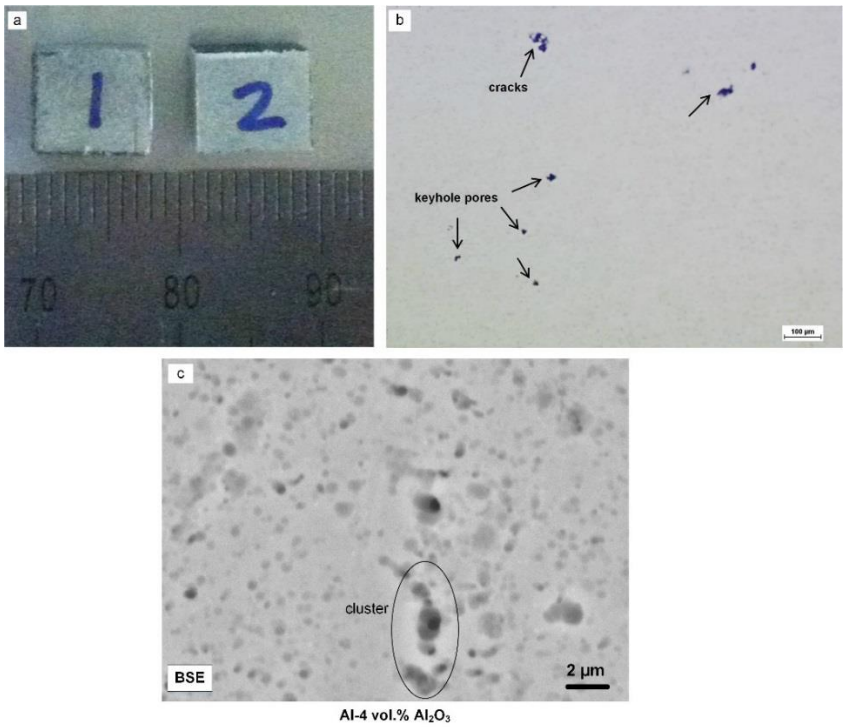

Figure 6.1: Images showing (a) cubic samples for microhardness and wear test, (b) porosity of the sample on the top surface and (c) distribution of Al_2O_3 in Al.

Figure 6.1a shows the cubic samples fabricated under the optimum condition of 200 W laser power and an exposure time of 250 µs, which is equivalent to a 300 mm/s scanning speed (chapter 5). Figure 6.1b shows the top surface of a polished sample in which a few keyhole pores and microcracks have formed. The porosity on the composite specimen surface (Figure 6.1b) was evaluated using ImageJ software, and was found to be 0.168%. The average circularity of the keyhole pores was 0.812 and the measured pore size varied from 10 to 38 µm with an average value of 22.4 µm. Furthermore, the as-fabricated cubic samples were both horizontally and vertically sectioned to investigate the spatial distribution of Al_2O_3 particulates; the Al_2O_3 particulates were found to distribute fairly uniformly amongst the Al matrix. Figure 6.1c shows the distribution of Al_2O_3 particulates in the vertically sectioned cubic sample. The distribution density of Al_2O_3 was also evaluated using ImageJ software, and was found to be 13.9%; the circularity of the measured Al_2O_3 particulates was 0.81 with an average size of 350 nm; a few clusters were still formed though (Han et al. 2017c).

6.3 Results

This section details the results of tensile test, microhardness test, macro and nanoscale wear test.

6.3.1 Tensile Behaviour of As-fabricated Samples

Figure 6.2 shows the tensile results of pure Al samples and composite samples under different conditions. The composite sample under optimum process

parameters exhibited a 36.3% improvement in yield strength ($\sigma_{0.2}$) as compared to the pure Al sample fabricated under the same conditions: 109 MPa and 80 MPa, respectively. The ultimate tensile strengths (UTSs) of the composite and pure Al samples were found to be 160 MPa and 110 MPa, respectively, indicating a 45.5% improvement in UTS. Figure 6.2a also shows the tensile behaviour of the as-fabricated composite sample fabricated at 100 mm/s; a 106 MPa UTS and 2.4% elongation were noted. The tensile samples used in this study are shown in Figure 6.2b.

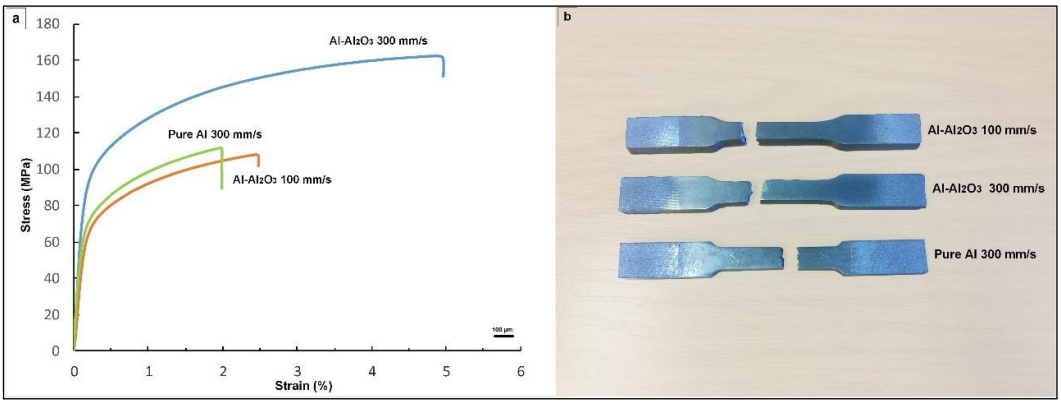

Figure 6.2: (a) Tensile stress-strain curves of as-fabricated pure Al and composite samples; (b) photograph of the samples after the tensile testing.

Figure 6.3 shows the fractures of the as-fabricated composite samples fabricated at 100 mm/s (Figure 6.3a–c) and 300 mm/s (Figure 6.3d–e), respectively. A few obvious cracks (A_1-A_5) were present in the fracture surface of the sample fabricated at 100 mm/s; these cracks contributed to a brittle fracture associated with a low elongation, which was consistent with the tensile performance shown in Figure 6.2.

EDS analysis (Figure 6.3b) confirmed that the present cracks were attributable to oxides that were from the original feedstock and/or were generated during the SLM process. Figure 6.3d–f shows the fracture surface of the composite sample fabricated at 300 mm/s. The fracture surface shows a higher number of fine dimple structures and fewer cracks compared to the tensile samples fabricated at 100 mm/s, which suggests a ductile fracture rather than a brittle fracture. One can see that a few deep holes were formed and surrounded by very fine dimple structures at the fracture surface; this implies that the microstructure at the vertical section (along the building direction) was not particularly uniform because of the grain growth.

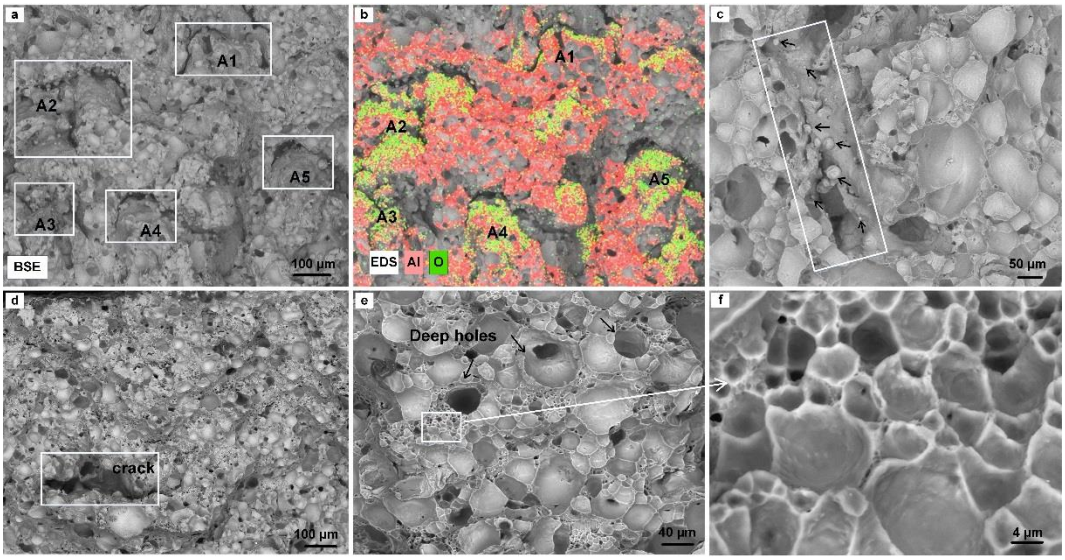

Figure 6.3: SEM micrographs showing the fracture surfaces of as-fabricated composite samples fabricated at (a–c) 100 mm/s and (d–f) 300 mm/s (A1-A5 presenting the observed cracks under the scanning speed of 100 mm/s).

The pure Al samples were also fabricated and tested to investigate the influence of added Al_2O_3 reinforcement on tensile behaviour. The tensile behaviour of pure Al fabricated at 300 mm/s showed agreement with Kimura et al.

(2017) and exhibited much stronger strength than the pure wrought-aluminium values described in the literature (Kalpakjian and Schmid 2014), which were 35 MPa and 90 MPa for yield strength and UTS, respectively. This is believed to have been induced by the rapid cooling within the SLM process. The elongation of pure Al (2%), however, was lower than that of the composite sample (5%); this elongation is thought to have been induced by the scanning speed.

Compared to the composite powder, the pure Al powder exhibited higher thermal conductivity; the optimum scanning speed (300 mm/s) for the composite powder may not have been optimum for accumulating sufficient heat to fully melt the powder. Porosity as well as partially melted powders were found to have formed, which was confirmed by the microstructure observation. The composite sample fabricated at 100 mm/s scanning speed exhibited poorer mechanical strength than that of the 300 mm/s scanning speed; this poorer tensile behaviour is thought to have been induced by the interaction between recoil pressure and Marangoni convection under super-slow scanning speeds, which contributed to the formation of keyhole pores and microcracks (oxides) (King et al. 2014; Khairallah et al. 2016).

The fracture surface of the tensile sample fabricated at 100 mm/s showed a few cracks, and EDS analysis confirmed that these cracks had been caused by oxidation (Figure 6.3a–b). Similar fracture surfaces were also observed in the SLM of Al alloys by others (Louvis et al. 2011; Read et al. 2015). The thin oxide films in the present study failed to wet the surrounding powders properly, thus contributing to poor metallurgical bonding due to the formation of pores and

microcracks. It is likely that some of the powder could have be trapped in the poor-bonding regions (e.g. pores) when depositing the subsequent powder layer. These defects led to the formation of large cracks in the failed samples, as shown in Figure 6.3c.

6.3.2 Microhardness Behaviour

Figure 6.4 shows the microhardness of the composite samples and pure Al samples fabricated at 300 mm/s. Figure 6.4a shows the microhardness of the as-fabricated horizontal section (8 x 8 mm) as measured in three directions (a, b and c). It is clear that the average hardness values in the three directions were very close (49.48, 47.57 and 48.35 HV/0.1, respectively), which suggests that microhardness is directionally independent. Overlapping regions are generally thought to be weaker than other regions within one layer. In this work, however, the uniformity of the measured microhardness showed that the microhardness was independent of direction at the horizontal plane.

The microhardness of the pure Al sample in three directions was also measured; these results are shown in Figure 6.4b. An average microhardness of 41.3 HV/0.1 was obtained from the three directions, compared to a 48.5 HV/0.1 microhardness for the composite sample. The 17.5% increase in the microhardness is thought to have been caused by the addition of the Al_2O_3 reinforcement, which tends to improve strength by increasing the dislocation density in the composite sample because of the pinning effect of Al_2O_3 nano powder on grain boundaries.

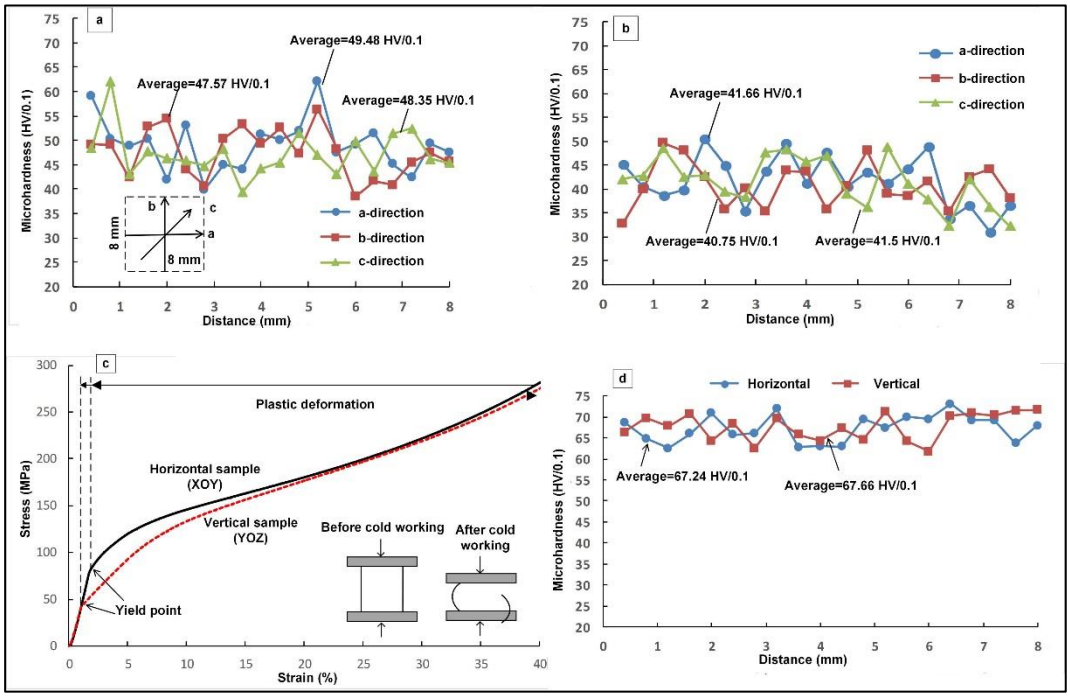

Figure 6.4: Microhardness of the samples fabricated at 300 mm/s: (a) composite and (b) pure Al; (c) stress-strain curve of the composite samples under cold working; (d) microhardness of the samples subjected to cold working.

Figure 6.4c shows the stress-strain curves of the horizontally and vertically composite samples induced by cold working. One can see that the compressive behaviour of the two samples were consistent at the elastic-deformation stage, while the horizontal sample exhibited a higher yield stress than the vertical sample; this is believed to have been induced by the building direction. After the yield points, the samples were subjected to plastic deformation, at which point the compressive behaviour tended to be consistent when the strain was greater than 20%.

Figure 6.4d shows the microhardness of the two cold-worked samples with a 40% strain. Because this study has shown that the microhardness of

samples fabricated using SLM is directionally independent at the horizontal plane, the hardness of the two cold-worked samples was only measured in one direction (the ‘a’ direction). The horizontal and vertical samples exhibited very close average microhardness values of 67.24 and 67.66 HV/0.1, respectively. Further, the hardness behaviour of the two samples showed consistency with their compressive behaviour within the cold-working process: a 40% strain was associated with a roughly 280 MPa stress for both the horizontal and vertical samples (Figure 6.4c).

The experimental results demonstrated that cold working played a significant role in microhardness alteration. The marked observed increase in microhardness (about 39%) compared to the as-fabricated composite samples is attributable to the plastic deformation that occurs within the cold-working process. During the cold working, the grains become deformed and elongated. The deformed samples exhibit high strength and hardness because of the entanglement of the dislocations with grain boundaries and with one another. This finding validates the hypothesis in section 6.1 and the microstructure observation shown in chapter 5, in which both molten pool tracks and grains were shown to be deformed and elongated after the cold-working process. The increase in strength depends on the degree of plastic deformation that occurs: in general, the higher the deformation, the stronger the part becomes. Cold working, however, results in a product with anisotropic properties due to the preferred orientation (e.g. reduction in ductility).

6.3.3 Pin-on-disc Friction and Wear Performance

Figure 6.5 shows the friction and wear performance of the composite and pure Al samples after the pin-on-disc tests. Figure 6.5a shows the friction coefficient variation of the composite specimen fabricated at 300 mm/s. At the beginning of sliding, the friction coefficient offered a large fluctuation due to the vibration and it tended to be relatively stable afterwards. The average friction coefficient of the composite specimen was determined to 0.83 after 30 minutes' sliding. The friction performance of pure Al exhibited similar vibration trend at the beginning of sliding, while a smaller average friction coefficient was determined, which was 0.74 (Figure 6.5b) (Han et al. 2017c).

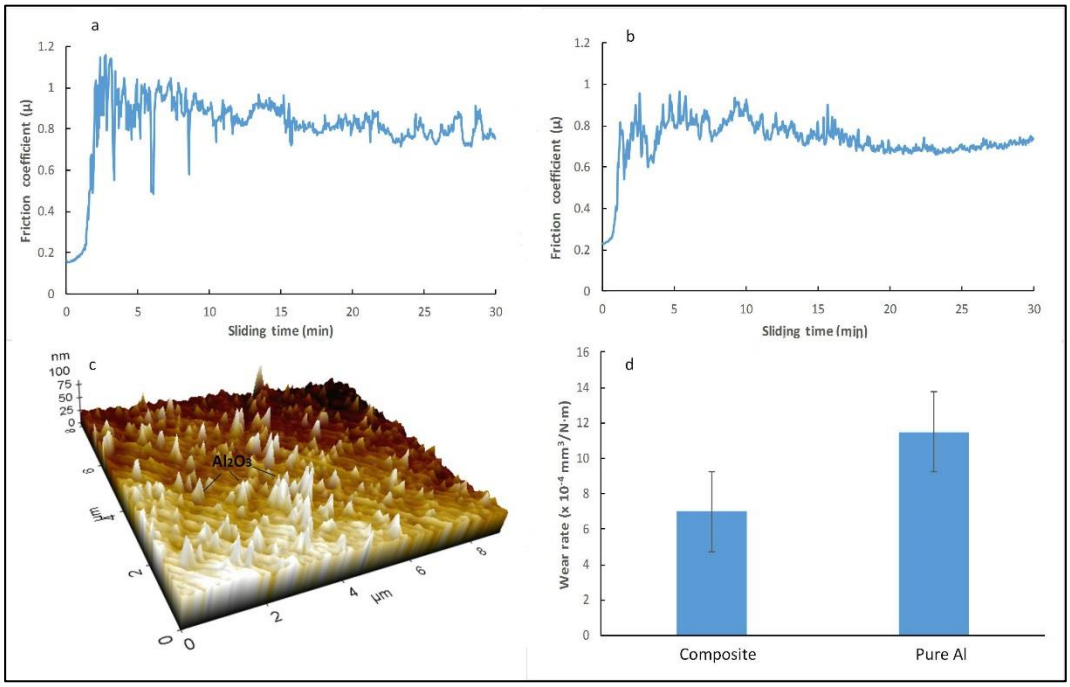

Figure 6.5: Friction and wear behaviour: friction coefficient variation of (a) composite, (b) pure Al, (c) AFM 3D topography and (d) wear rate.

By comparison with pure Al, the composite specimen offered a slight improvement in average friction coefficient, and this situation may be explained by the uniform distribution of Al_2O_3 reinforcement amongst Al matrix. Due to the significant hardness difference between the Al_2O_3 and Al phases, part of the Al_2O_3 particulates were exposed outside the Al matrix after the polishing process, which in turn resulted in a rougher surface topography than pure Al specimen. This situation was confirmed by the 3D AFM topography image (Figure 6.5c). In addition to the friction coefficient distribution, another indicator is wear rate.

Figure 6.5d shows the wear rate of the composite and pure Al specimens after wear tests, which were 7 and 11.5 x 10^{-4} mm^3/Nm, respectively. Compared to the pure Al specimen, the composite exhibited better wear behaviour with a smaller wear rate, which may be attributed to the addition of Al_2O_3 reinforcement.

In order to further investigate the wear mechanism of SLM produced composites during the wear tests, the SEM images of both composite and pure Al specimens after wear tests are shown in Figure 6.6. Figure 6.6a (1–3) show the wear trace of the composite specimen with different magnifications. It is clear that several microchips were produced and narrow grooves left on the specimen surface (Figure 6.6a–3), which implies the dominating wear mechanism was abrasive wear. It should be noted that the delamination took place on the composite surface; with a continued sliding, the upper layer would delaminate from the specimen surface and formed microchips and wear particles subsequently.

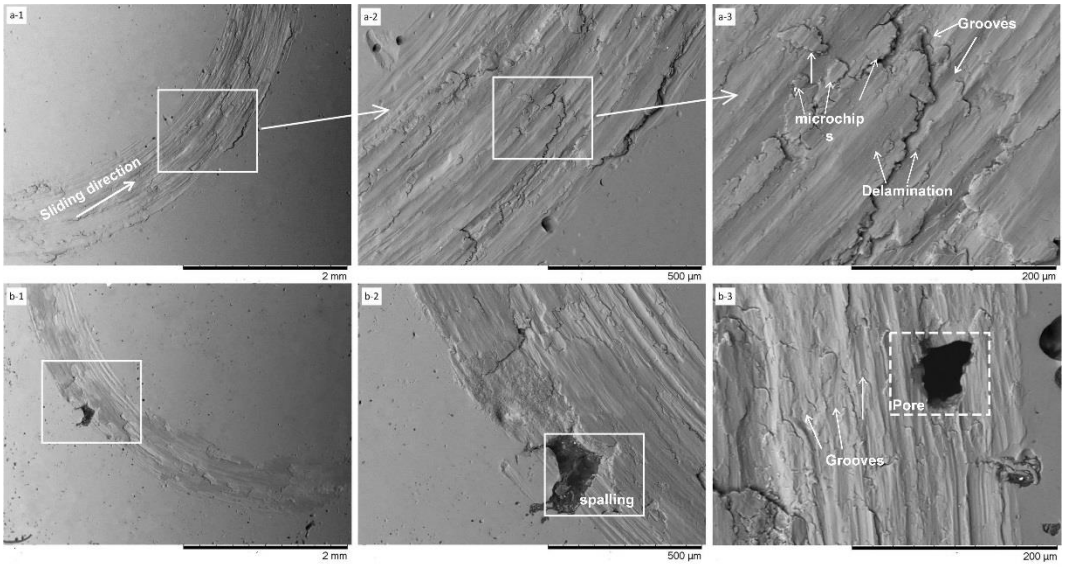

Figure 6.6: SEM images showing the worn region of the composite and pure Al samples.

Compared to the composite specimen, the pure Al specimen tended to offer worse wear behaviour and flake spalling was observed on the worn surface (Figure 6.6b-2). A larger number of parallel and narrow grooves were formed on the worn specimen surface due to the generation of microchips and wear particles (Figure 6.6b-3). Since the Al specimen exhibited higher porosity than the composite specimen, a relatively huge pore was also observed on the worn surface of the pure Al specimen.

6.3.4 Nanoscale Friction Behaviour

Figure 6.7 shows typical AFM images of the polished vertical section from the as-built cube sample. Figure 6.7a and b show the two-dimensional (2D) surface profile, which indicated a uniform distribution of Al_2O_3 (the white and yellow features in Figure 6.7a and b, respectively).

To further help to understand the details of Al_2O_3 reinforcement in the sample, Figure 6.7c shows the 3D topography of the sample. Due to the significant hardness difference between the Al_2O_3 and Al phases, part of the Al_2O_3 particulates were exposed outside the Al matrix after the polishing process, which then resulted in the observed roughness at the sample surface. Figure 6.7d shows the topography details when the surface was horizontally and perpendicularly sectioned using straight lines *a* and *b* (Figure 6.7a).

Several special positions are indicated in Figure 6.7d, which shows the rough dimensions and distribution of the Al_2O_3 reinforcement. It should be noted that this sample showed a slight slope in the perpendicular direction, which is thought to be induced by the placement of the testing sample; this may be observed from the perpendicular surface topography shown in Figure 6.7d.

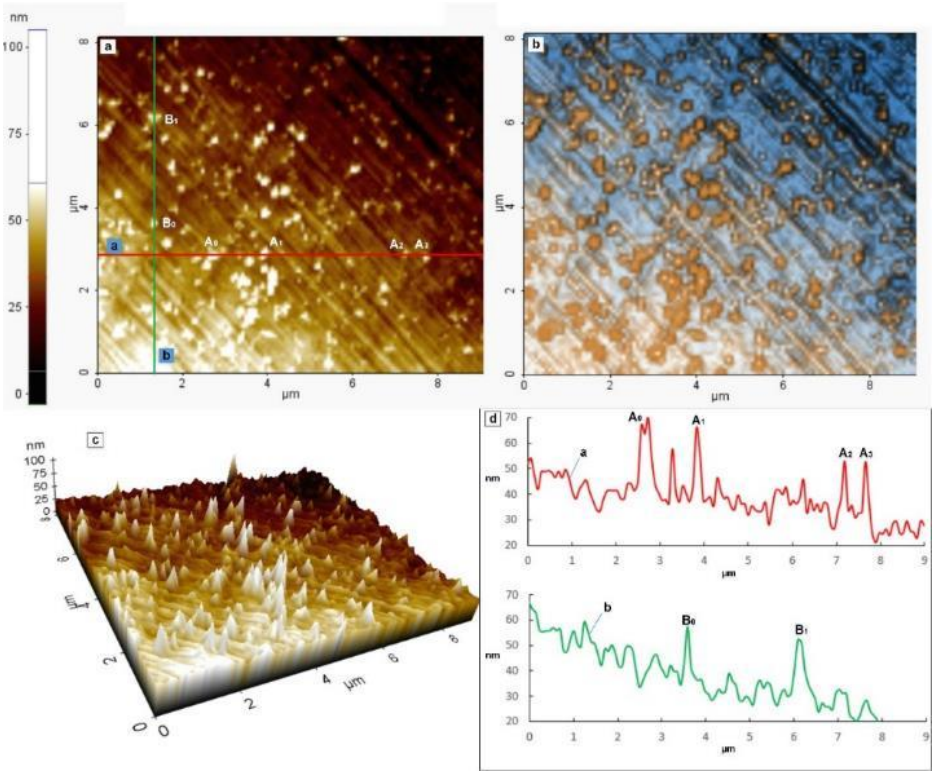

Figure 6.7: Atomic force microscopy (AFM) image of the polished vertical section. 2D profile images (a) and (b) that imply a uniform distribution of Al_2O_3 particulates (white and yellow dots); (c) 3D image of the sample surface; (d) surface-topography distribution, indicating a slight slope of the sample. (For interpretation of the colour references, the reader is referred to the electronic version.)

Figure 6.8a shows a schematic of AFM nanoscratching and the pyramidal diamond tip that was used in this study, with a nominal radius of less than 40 nm, as indicated in the SEM image. Figure 6.8b shows a 3D AFM image of the sample that was scratched under the normal load of 30 µN. As the figure shows, a clear groove through a keyhole pore was generated, along with produced pile-up. The lateral voltage output difference and Z signal were then captured (Figure 6.8c). The lateral signal was used to determine the friction force during the scratching and the conversion factor α was calculated using a standard

calibration grating, which was 23.75 μN/V. The *Z* signal output is the displacement of piezoelectric actuator that defines the motion of the AFM probe in the Z direction and as a result, indicates the surface roughness of the scratched path. A hole in the sample surface is generally indicated by a convex shape; a surface hill, in contrast, would be indicated by a concave shape in the captured Z signal graph.

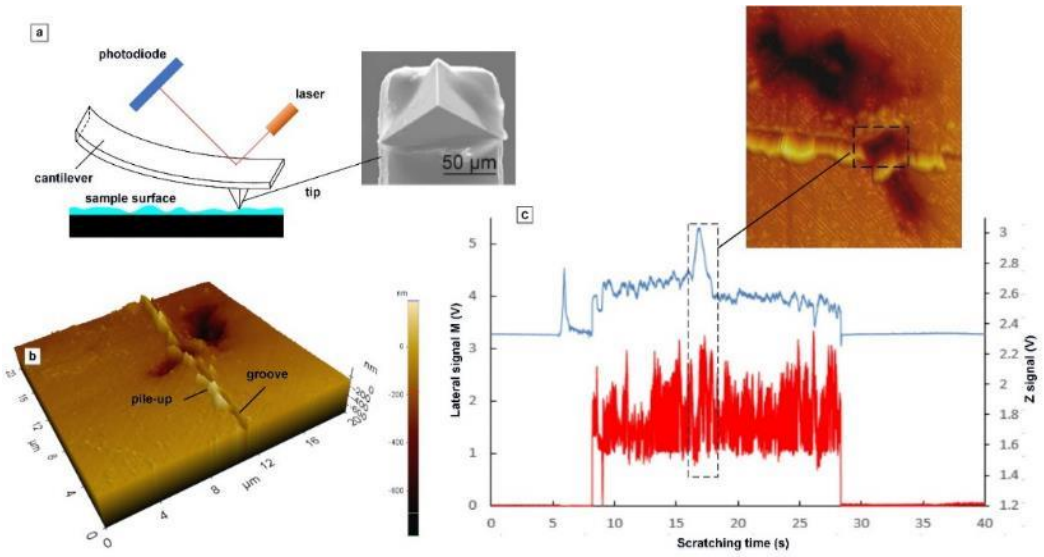

Figure 6.8: Scratched sample surface with a pore and detected signals: (a) schematic of the scratching and SEM image of the diamond tip; (b) 3D image of the scratched sample surface; (c) detected lateral voltage output (red line) and *z* signal (blue line) during the scratching.

A clear convex profile was captured in the *Z* signal graph, which indicates that the marked keyhole was scratched and recorded. It should be noted that the lateral signal fluctuated after the beginning of the scratching and continued until the end; this may be explained by the uniform distribution of Al_2O_3 particulates, which were exposed outside the Al matrix after the polishing and thus resulted in

a rough sample surface; this shows agreement with the observation in Figure 6.7. Another phenomenon that should be mentioned is that the lateral signal experienced relatively dramatic fluctuations at the pore position, which suggests that the pore surface could have an important effect on the friction-force distribution during the AFM nanoscratching.

It should be reminded that keyholes are actually defects that occur during the SLM process and that, ideally, parts should be produced without them, as they could influence the friction and wear behaviour, in particular at nanoscale. To further understand the influence of the keyhole pore on friction force during the scratching, Figure 6.9a shows a magnification of the lateral signal at the pore position. The figure shows details of the lateral and Z signal's fluctuation within 2 s of scratching; the fluctuation of the lateral-voltage output from roughly 2.8 V to 0.8 V implies an irregularity in the scratched pore surface. Figure 6.9b shows the magnification of the pore surface with several marked specific positions (from A to F) in order to clarify the effect of the pore surface on the lateral signal output; the corresponding positions are from A' to F' in the lateral signal graph. Specifically, the scratching starts from position A to position F under a normal load (30 μN) and scratching speed (2 μm/s). Position A is the front edge of this keyhole pore, with a lateral voltage output of roughly 2.8 V; when the tip moves from position A to the bottom of the pore (illustrated as position B), the direction of the induced friction force is upwards along the slope.

Due to the deformation of the cantilever, however, a horizontal force and torsion moment are exerted on the tip to balance the contact load, friction force

and applied normal load; the lateral force is thus reduced when the tip experiences a downhill motion. According to Figure 6.9a, the Z signal shows an uphill motion between points B' and F', however, the lateral force increased and decreased considerably despite the Z gradient being fairly regular. The variation in lateral force can be explained by the fact that the tip was trying to follow the path of least resistance and some lateral movements were thus detected.

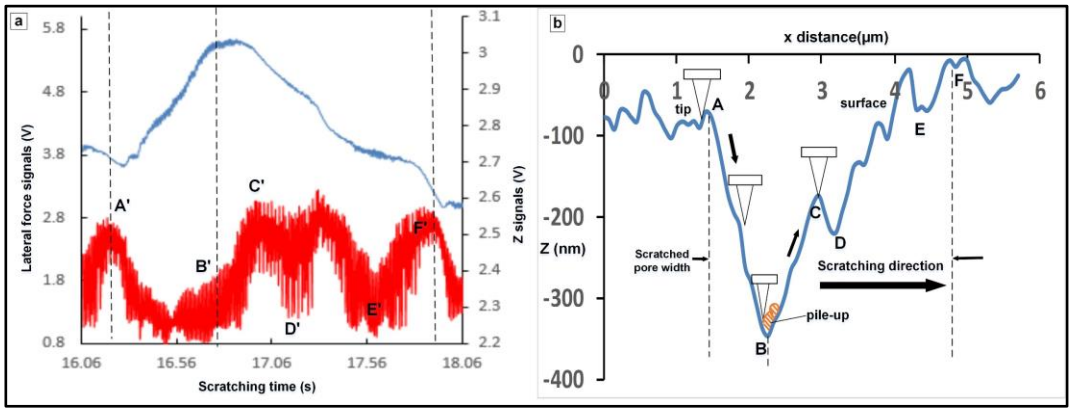

Figure 6.9: Influence of pore surface on lateral-force distribution: (a) magnification of the detected lateral-force signals at a pore; (b) magnification of the contact relation between the tip and pore surface.

It should be noted that when the tip reached the bottom position B, the lateral voltage output was not the minimum value; instead, it was greater than the minimum value, which suggests that the minimum lateral force was reached before it reached the bottom position, while the tip scratched the keyhole pore. This is thought to be induced by the pile-up accumulation; that is, while the tip experiences a downhill motion, the generated pile-up may accumulate in front of the tip and settle at the bottom position. When the tip arrives at the bottom position, the accumulated pile-up can exert a force on the tip that increases the lateral force. It can be determined that the difference in the lateral voltage output

between position A and the minimum (0.8 V) is roughly 2 V, and the friction-force difference induced by the downhill motion can also be determined; the difference is roughly up to 47.5 μN. When considering the applied normal force of 30 μN, we can conclude that the marked pore significantly influences the friction-force distribution during the AFM nanoscratching.

After reaching the bottom position B, the tip experiences an uphill movement along the slope. Due to the irregularity of the pore surface, the lateral voltage output fluctuates with the continued scratching. More specifically, an internal hill is located in position C; the direction of the induced friction force is thus downwards along the slope when the tip moves from position B to C. Further, due to the exerted horizontal force and the torsion moment by the deformed cantilever, the friction force increases with the continued scratching; the lateral voltage output thus reaches a peak at position C. A downhill motion then follows, which contributes to a decrease in the lateral output until the tip reaches position D. Between positions D and F, the irregular slope surface results in fluctuation of the lateral voltage output. The position F is another edge of the keyhole; the tip moves out of the keyhole pore afterwards.

It can thus be concluded that the keyhole pore plays an important role in lateral-force distribution, which implies that the friction-coefficient distribution would also be affected during AFM nanoscratching. The friction coefficient is the division of friction force by applied normal load; Figure 6.10 shows the friction coefficient distribution with respect to scratching time under different normal loads, varying from 10 μN to 40 μN. Figure 6.10a shows the friction coefficient

distribution under a normal force of 10 μN; the friction coefficient fluctuated from 0.3 to 2.1, with an average value of 1.12.

It should be noted, however, that apart from very limited positions with friction coefficient values of less than 0.5, the remainder of the scratched positions had a minimum friction coefficient of around 0.8. This can be explained by the pores that formed on the sample surface, which resulted in the jump of the friction coefficient; two typical pores are marked in the graph. The figure shows a magnified image of the friction coefficient distribution that was affected by the pore; the figure also includes a trend line. A friction-coefficient fluctuation from 2 to 0.3 is thought to be induced by the marked keyhole pore; the irregularity of the pore surface is also implied by the trend line.

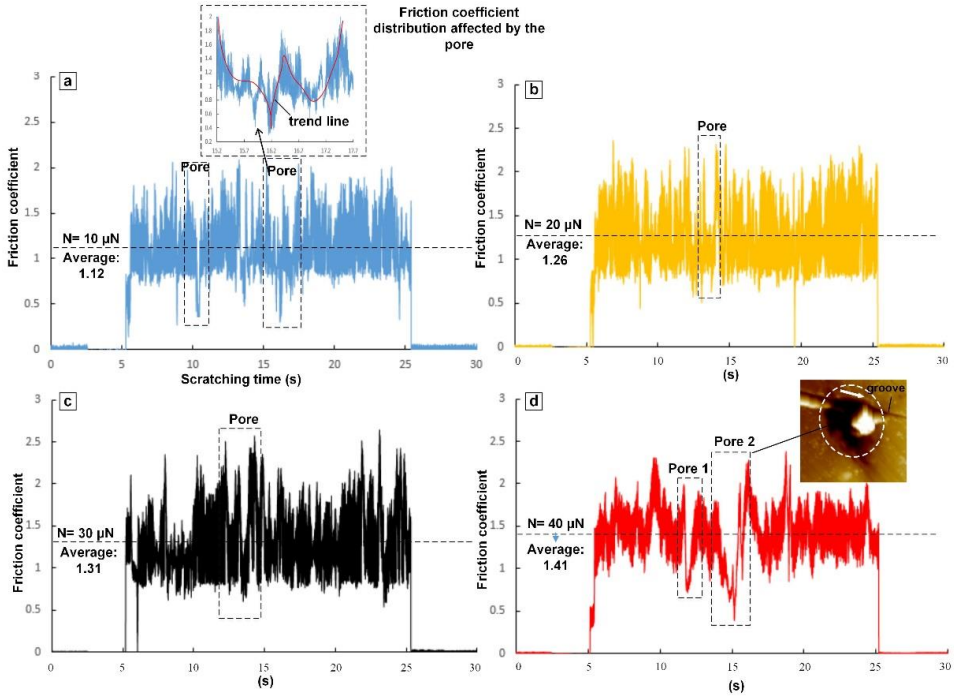

Figure 6.10: Friction coefficient distribution under normal loads of (a) 10 μN, (b) 20 μN, (c) 30 μN and (d) 40 μN.

The uniform distribution of the added nano Al_2O_3 reinforcement could be another significant factor to contribute to the fluctuation of the friction coefficient distribution. Al_2O_3 particulates were exposed outside Al matrix after polishing and contributed to a rough sample surface; a rough surface tends to increase the friction coefficient and an average friction coefficient of 1.12 was then determined. Figure 6.10b shows the friction coefficient distribution under the normal load of 20 µN; the figure indicates a friction coefficient distribution zone that was affected by a pore. Compared to Figure 6.10a, a slight overall increase in the calculated friction coefficient was observed, and an average value of 1.26 was determined. With a continuous increase in applied normal load (from 30 µN to 40 µN), the average friction coefficient increased from 1.31 to 1.41, respectively (Figure 6.10c and d).

6.3.5 Material Wear Rate

In addition to the friction coefficient, another significant indicator that is often used to characterise nanoscale-wear behaviour during AFM nanoscratching is the material wear rate, which is attained by dividing the grooved cross-sectional area by the applied normal load. The wearing of the pyramidal diamond tip during the scratching was assumed to be zero in this work in order to calculate the material wear rate. Figure 6.11 shows the measurements of the groove depth and width under an applied normal load of 30 µN. Figure 6.11a shows a typical AFM image of a groove; three different positions (a, b and c) on the groove were chosen to determine the groove dimensions by averaging the three measurements.

The cross-sectional profiles of the three marked positions are shown in Figure 6.11b; the groove profile was assumed to be triangular when calculating the section area. As the figure shows, the three different positions shared nearly the same measured width (d') of 313 nm; the measured depth (h'), however, varied from 104 nm to 114 nm. This situation may be explained by the addition of nano Al_2O_3 particles, which offer higher hardness when the tip touches these particulates at the groove bottom; a relatively shallower depth could thus be obtained, such as the chosen position 'a' shown in Figure 6.11a.

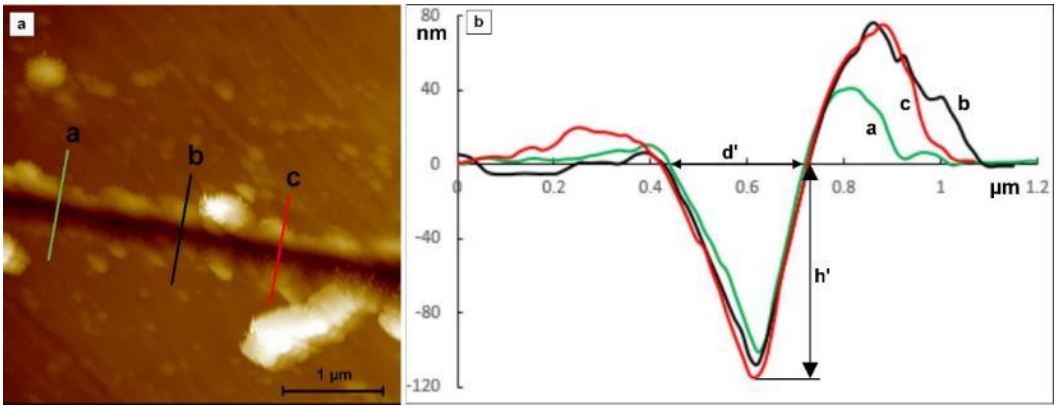

Figure 6.11: Groove-dimension measurement: (a) typical AFM image of groove; (b) groove depth and width variation at three different positions under 30 μN. (For interpretation of the colour references, the reader is referred to the electronic version.)

The averaged groove depth and width under normal loads from 10 μN to 40 μN are shown in Figure 6.12a; the measured groove depth increased from 52 nm to 135.6 nm, while the groove width increased from 204 nm to 337 nm. Further, it can be determined that both groove depth and width offer a nearly linear correlation with applied normal load. The calculated material wear rate and friction coefficient variation in relation to applied normal load are shown in Figure

6.12b. The figure shows that the wear rate increased from 5.3 x10^{-4} to 5.7 x 10^{-4} mm^2/N as the normal load varied from 10 µN to 40 µN.

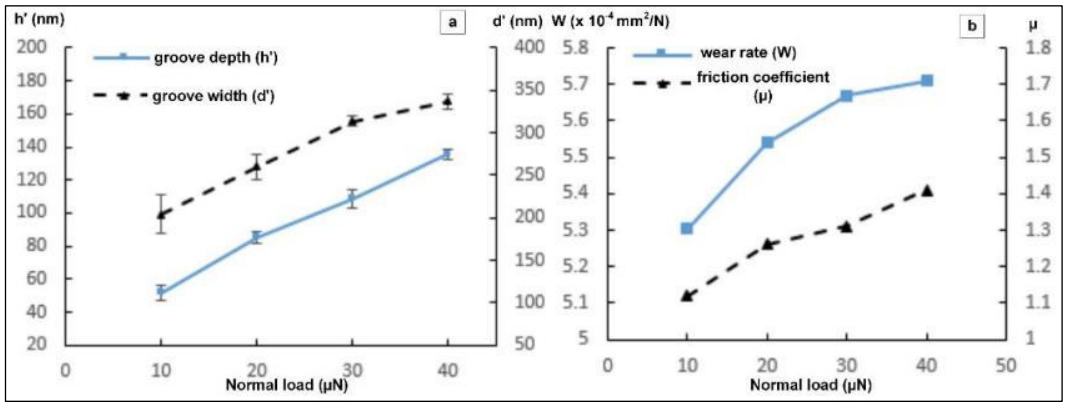

Figure 6.12: Material wear rate calculation with (a) measured groove dimensions and (b) calculated wear rate and friction coefficient in relation to normal load.

6.4 Discussion

6.4.1 Wear Rate and Microhardness

The wear rate of composite and pure Al specimens were determined to be 7 and 11.5x10^{-4} mm^3/Nm, respectively (Figure 6.5d). Kang et al. (2016) reported that the wear rate of Al-12Si alloy fabricated by SLM was 9x10^{-4} mm^3/Nm (Kang et al. 2016). One can see that the nearly full-dense composite samples exhibit better wear behaviour than the widely used Al alloy; this may be explained by the addition of Al_2O_3 reinforcement. It has been found that the abrasive-wear resistance is proportional to the part's hardness; abrasive wear can thus be reduced by increasing the hardness of materials (e.g. heat treatment) or by reducing the normal load (Kang et al. 2016; Kalpakjian and Schmid 2014). Figure 6.13 shows the measured microhardness of the composite and pure Al samples

as measuring 20 discrete locations. The averaged microhardness of composite and pure Al were 48.35 and 40.75 HV/0.1, respectively. The 18.6% increase in microhardness of the composite sample is thought to be induced by the addition of 4 vol.% Al_2O_3 reinforcement. This finding confirms the harder composite specimen tended to exhibit better abrasive wear behaviour than unreinforced Al specimen.

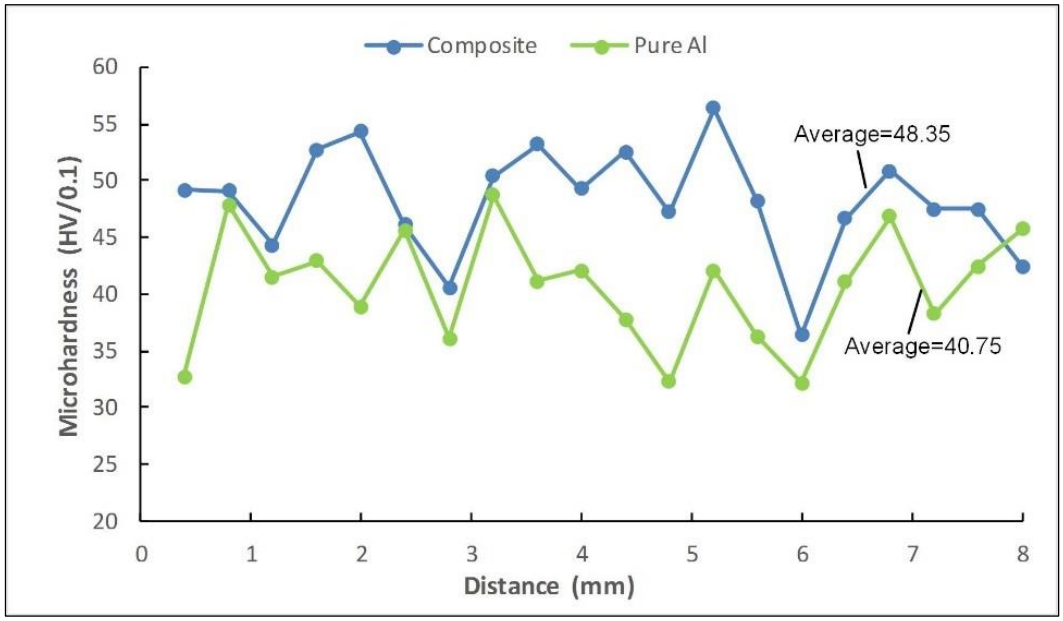

Figure 6.13: Microhardness of the composite and pure Al samples fabricated at 300 mm/s.

6.4.2 Nanoscale Wear Behaviour with Normal Load

The AFM nanoscratching results indicated the friction coefficient increased with an increase in applied normal load (Figure 6.10); this situation may be explained by a change of the contact condition and adhesion force between the AFM tip and the specimen. Specifically, an increase in the normal load generally results in an increase in groove depth; when the groove depth is greater than the height of

the diamond tip's spherical apex (with a tip radius of less than 40 nm), the dominant contact condition between the tip and the specimen becomes pyramidal rather than spherical. A pyramidal contact offers a larger contact area and further increases the adhesion force; an increase in adhesion force between tip and specimen thus leads to an increase in the friction force and friction coefficient. This finding is in agreement with (Chung et al. 2003), in which an AFM was used to investigate the fundamental micro-wear rate; that study found that the increase in adhesion force due to an increased contact area caused the contact pressure to increase during the scratching when a Si_3N_4 tip was employed to scratch a Si specimen surface with an applied load from 10 to 800 nN.

According to the wear behaviour that the composite exhibited (Figure 6.12), the average groove depth (52 nm) under a 10 μN normal load was slightly larger than the height of the diamond tip's spherical apex, with a tip radius of less than 40 nm (Figure 6.12a); this situation implies that the contact condition included a spherical contact that was induced by the tip radius and pyramidal contact, which in turn was induced by the pyramidal shape of the tip. With an increase in the normal load to 40 μN, the groove depth increased and the pyramidal contact became the dominating contact condition. The increased contact area led to an increase in adhesion force and further contributed to an increase in the friction coefficient. The variation trend of the wear rate showed agreement with the friction coefficient trend; both can be explained by the change in contact condition within the AFM nanoscratching.

6.5 Summary

Advanced testing and analytical techniques were employed to investigate the mechanical properties of the SLM fabricated samples in this chapter and the experimental results validated the hypotheses. That is, the uniform-distributed Al_2O_3 reinforcement contributed to the alteration of mechanical properties. Compared to pure Al, 36.3% and 17.5% increases in yield strength and microhardness (respectively) for the composite samples were achieved. Cold working played a significant role in enhancing mechanical strength via changes to the material microstructure. Compared to the as-fabricated composite sample, the cold-worked composite sample showed a 39% increase in microhardness. This increase is thought to have been caused by the plastic deformation, in which grains were deformed and elongated. A higher shear stress was thus required to cause further slippage.

The added Al_2O_3 reinforcement contributed to the alteration of macroscale wear behaviour. Compared to pure Al, a smaller wear rate for the composite specimen was achieved. Irregular pore surfaces may result in dramatic fluctuations in the frictional coefficient at the pore position during the AFM nanoscratching process. The measurements of single point contacts demonstrate that the presence of the pores can significantly increase friction if asperities contacting the surface engage with them.

The size effect and working principle difference contributed to the difference in friction coefficient at macro and nano scales. That is, the recorded average friction coefficient of the composite specimen under 1 N normal load was

0.83 during the pin-on-disc sliding, while the average friction coefficient during the atomic force microscopy nanoscratching increased from 1.12 to 1.41 as the applied normal load varied from 10 μN to 40 μN. Third, during the atomic force microscopy nanoscratching, both average friction coefficient and wear rate showed nearly linear correlation with applied normal load. This was thought to have been induced by the change of adhesion force and contact condition between the diamond tip and the tested specimen.

The experimental findings of this work will help to achieve an improved understanding of mechanical properties alteration that are affected by the reinforcements of the Al-Al_2O_3 nanocomposites often used in aerospace and automotive industries. This study also seeks to expand the potential applications of the combination of selective laser melting and atomic force microscopy in researching nanoscale wear behaviour.

Chapter VII

Contributions, Conclusions and Future Work

This chapter concludes the work presented in this thesis. Section 7.1 lists the main contributions of this research. Section 7.2 provides the conclusions, while the directions of future work are presented in Section 7.3.

7.1 Contributions

The contributions of this study are as follows:

i. A method is developed for synthesising and characterising nanocomposite powder suitable for selective laser melting. An advanced Al-4 vol.% Al_2O_3 nanocomposite powder suitable for selective laser melting is synthesised using high-energy ball-milling and characterised using systematic analytical techniques. The influences of milling and pause duration on the fabrication of ball-milled powder for selective laser melting are studied and found that the short milling (10 min) and long pause (15 min) combination provided a higher yield and narrower particle size distribution range than long milling (15 min) and a short pause (5 min).

ii. A simulation model is developed for predicting thermal behaviour within selective laser melting the first layer. A 3D finite element model is developed in the ANSYS platform to predict the thermal behaviour (e.g. transient temperature distribution and molten pool dimensions. The thermal simulation enables a more efficient selection of process parameters used in manufacturing bulk samples; the range of scanning speeds is thus limited to 100-600 mm/s and the hatch spacing is chosen to be 70 and 100 μm.

iii. A methodology is developed for selective laser melting process parameters optimisation. The SLM process parameters used to manufacture nearly full-dense composite samples are optimised and the microstructure of the fabricated samples is analysed. The optimum laser energy density and scanning speed are determined to be 317.5 J/mm^3 and 300 mm/s, respectively. The fabricated composite samples are observed to exhibit fine granular-dendrite microstructure due to the rapid cooling, while the thermal gradient at the molten pool region along the building direction is found to facilitate the formation of columnar grains. Due to the plastic deformation, cold working results in grain deformation and elongation.

iv. A method is developed for studying the influence of reinforcement on composites' mechanical properties. The studied mechanical properties of the fabricated composites samples include tensile strength, microhardness and wear behaviour. It examines the influences of nano Al_2O_3 reinforcement and cold working on mechanical property alteration.

The pin-on-disc wear testing and AFM nanoscratching are performed to study the macro and nanoscale wear behaviour, which will help to achieve an improved understanding of macro and nanoscale friction and wear mechanisms that are affected by the reinforcement and porosity of the Al-Al_2O_3 nanocomposites.

7.2 Conclusions

The main aim of this study is to manufacture an advanced Al-4 vol.% Al_2O_3 nanocomposites using the selective laser melting. In this thesis, the main aim together with individual research objectives have been achieved.

High-energy ball-milling was employed to synthesise the advanced Al-Al_2O_3 nanocomposite powder suitable for selective laser melting. It investigated the effect of milling and pause duration on the yield of Al-Al_2O_3 nanocomposite powder and employed advanced nano-metrology methods and analytical techniques to study the characteristics of the composite powder. The composite powder ball-milled for 20 h was considered to be suitable for selective laser melting due to its nearly spherical morphology, good flowability and high mechanical property. It also found that that the short milling (10 min) and long pause (15 min) combination provided a higher yield and narrower particle size distribution range than long milling (15 min) and a short pause (5 min). In addition, the employed analytical techniques and advanced metrology can also be used to explore the synthesis of other new materials used for selective laser melting.

A 3D finite element model has been developed to predict the thermal behaviour within selective laser melting of the first layer's composite powder; the single layer consisted of three single tracks in order to reduce computation time. A range of combinations of process parameters such as laser power, scanning speed and hatch spacing have been employed to predict the transient temperature distribution and molten pool dimensions. A set of experiments on scanning of single layer have been conducted and the results indicated that, the dimensions of molten pool decreased with an increase in scanning speed and this trend was more obvious when the scanning speed was greater than 600 mm/s. It has also been found that no metallurgical bonding could be built between two adjacent hatches when the hatch spacing was increased to 130 μm. In order to save experimental cost in optimising laser energy density and scanning speed, the range of scanning speeds used in SLM of bulk composite samples was thus limited to 100–600 mm/s; the hatch spacing was chosen to be 70 μm and 100 μm.

The optimum laser energy density and scanning speed have been determined by evaluating the relative density of the as-fabricated composite samples. The mechanism of pore formation within SLM was discussed. The transition of laser working mode from conductive to keyhole-mode was thought to be the primary factor that causes the formation of pores when relatively low scanning speeds are employed. The phase of Al_2O_3 has not been detected in the as-fabricated composite samples due to the relatively low volume percentage (4 vol.%). The OM and SEM images show the fine granular-dendrite microstructure of the as-fabricated composite samples due to the rapid cooling within SLM; the

columnar microstructure along the building direction was attributed to the thermal gradient at the molten pool region. The influence of cold working on microstructure change was also examined; the grains were found to be deformed and elongated due to plastic deformation, which contributed to the alteration of mechanical properties of the fabricated samples.

Advanced testing and analytical techniques were employed to investigate the mechanical properties of the SLM fabricated samples. The results indicated that the fairly uniform-distributed Al_2O_3 reinforcement contributed to the alteration of mechanical properties. Compared to pure Al, 36.3% and 17.5% increases in yield strength and microhardness (respectively) for the composite samples were achieved. Cold working played a significant role in enhancing mechanical strength via changes to the material microstructure. Compared to the as-fabricated composite sample, the cold-worked composite sample showed a 39% increase in microhardness. This increase is thought to have been caused by the plastic deformation, in which grains were deformed and elongated.

The added Al_2O_3 reinforcement contributed to the alteration of macroscale wear behaviour. Compared to pure Al, a smaller wear rate for the composite specimen was achieved. Irregular pore surfaces resulted in dramatic fluctuations in the frictional coefficient at the pore position during the AFM nanoscratching process. The measurements of single point contacts demonstrate that the presence of the pores can significantly increase friction if asperities contacting the surface engage with them. The size effect and working principle difference contributed to the difference in friction coefficient at macro and nano scales. That

is, the recorded average friction coefficient of the composite specimen under 1 N normal load was 0.83 during the pin-on-disc sliding, while the average friction coefficient during the atomic force microscopy nanoscratching increased from 1.12 to 1.41 as the applied normal load varied from 10 μN to 40 μN. Third, during the atomic force microscopy nanoscratching, both average friction coefficient and wear rate showed nearly linear correlation with applied normal load. This was thought to have been induced by the change of adhesion force and contact condition between the diamond tip and the tested specimen.

The experimental findings on wear behaviour will help to achieve an improved understanding of mechanical properties alteration that are affected by the reinforcements of the Al-Al_2O_3 nanocomposites often used in aerospace and automotive industries. This study also seeks to expand the potential applications of the combination of selective laser melting and atomic force microscopy in researching nanoscale wear behaviour.

7.3 Future Work

The following is a list of potential work that can be considered in the future:

- The composite powder used in this study was ball-milled for 20 hours by employing a short milling (10 min) and long pause (15 min) combination. Whilst a short milling a long pause combination generates a relative high yield for SLM, it consumes more working time. An optimum milling and pause combination should be determined to balance the yield and working efficiency in the future work.

- The ball-milled composite powder comprises 96 vol.% Al and 4 vol.% Al_2O_3 powders. The Al_2O_3 reinforcement is found to distribute uniformly amongst Al matrix after 20 hours of milling, and the SLM fabricated composite samples exhibit better mechanical properties than pure Al (e.g. tensile strength, microhardness and wear resistance). The future work may explore the ball-milling of composite powder with higher volume percentage of Al_2O_3 reinforcement such as 8 vol.% and 12 vol.%.
- A 3D finite element model is developed in this study in order to investigate the thermal behaviour of the powder bed during the laser scanning. The modelling scale, however, is at macroscale which means the powder bed is assumed to be a solid block. The future work may build a microscale finite element model, where the powder bed should consist of discrete spherical balls.
- The microstructure and mechanical properties of as-fabricated composite samples are studied in this work, the future work may investigate the influence of post process (e.g. heat treatment) on microstructure and mechanical properties change of the SLM fabricated parts. The addition of Al_2O_3 reinforcement is thought to enhance the mechanical properties of the composites at high temperature; the future work may also need to study the tensile behaviour of the SLM fabricated samples at high temperature.

Appendix A

This appendix includes additional information to illustrate the composite powder synthesis and characterisation presented in the thesis.

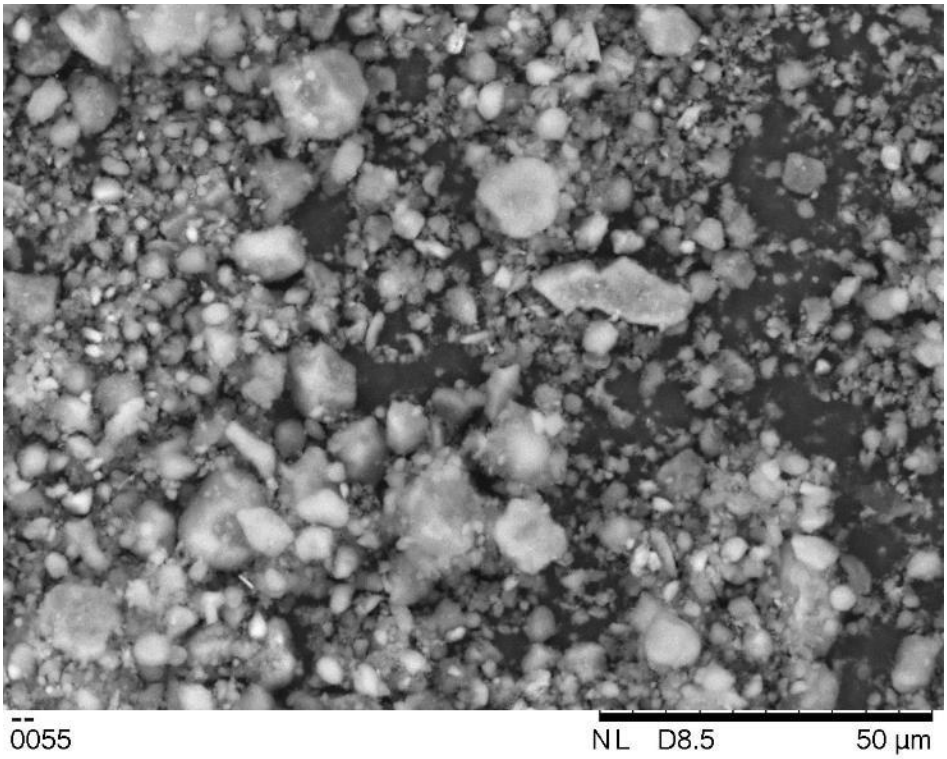

Figure A-1: SEM image showing the morphology of raw Al_2O_3 powder.

Figure A-2: Ball-milled pure Al for 6 hours without PCA.

Figure A-3: The employed shaker and produced flake-like powders.

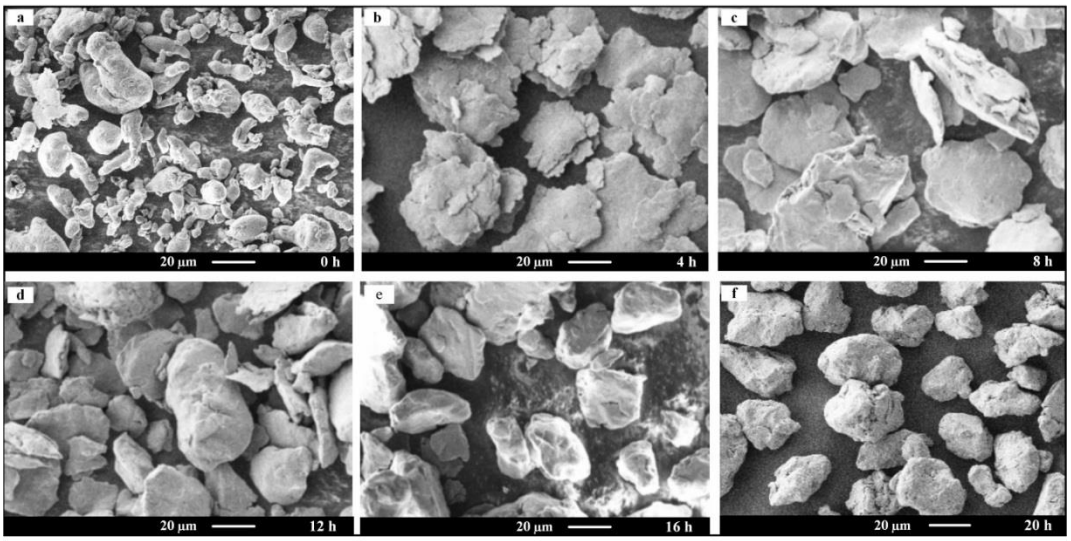

Figure A-4: The morphology of Al powder after milling for (a) 0 h, (b) 4 h, (c) 8 h, (d) 12 h, (e) 16 h and (f) 20 h.

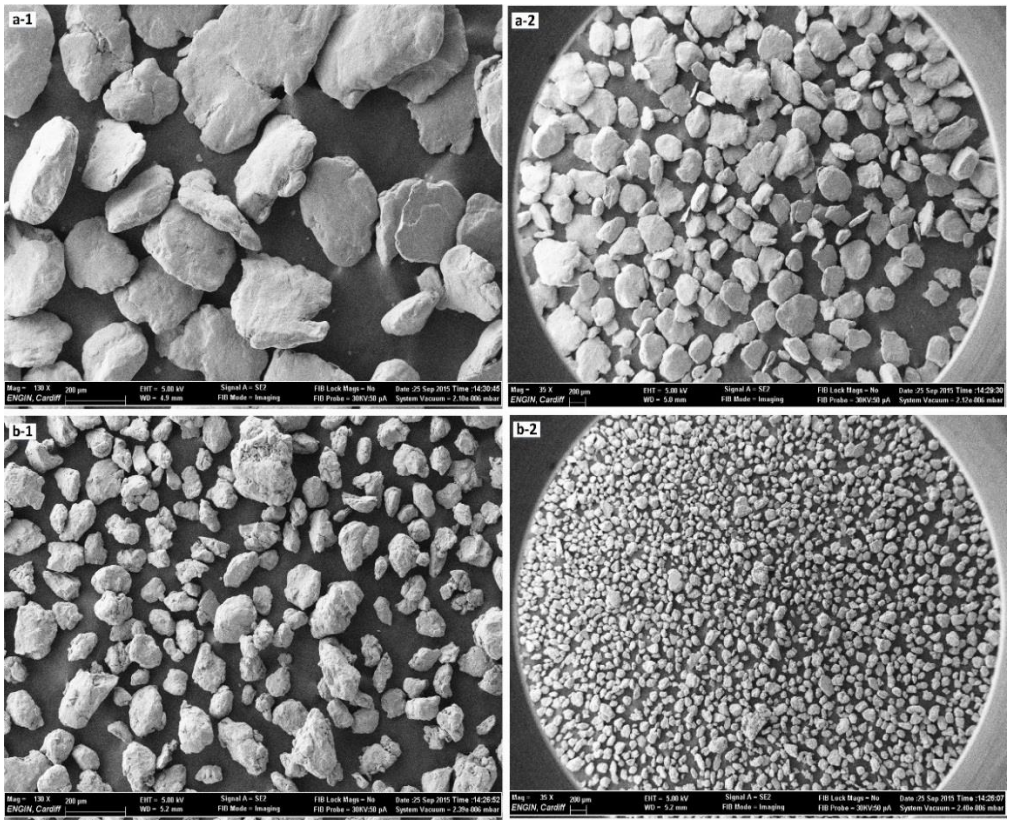

Figure A-5: SEM images showing the morphology of ball-milled composite powder for (a) 14 h and (b) 20 h.

Result

Size (µm)	% Volume In	Size (µm)	% Volume In	Size (µm)	% Volume In	Size (µm)	% Volume In	Size (µm)	% Volume In	Size (µm)	% Volume In	Size (µm)	% Volume In	Size (µm)	% Volume In
0.0100	0.00	0.0597	0.00	0.357	0.00	2.13	0.00	12.7	0.76	76.0	5.43	454	0.00	2710	0.00
0.0114	0.00	0.0679	0.00	0.405	0.00	2.42	0.00	14.5	1.07	86.4	2.69	516	0.00	3080	0.00
0.0129	0.00	0.0771	0.00	0.460	0.00	2.75	0.00	16.4	1.54	98.1	0.06	586	0.00	3500	
0.0147	0.00	0.0876	0.00	0.523	0.00	3.12	0.00	18.7	2.25	111	0.00	666	0.00		
0.0167	0.00	0.0995	0.00	0.594	0.00	3.55	0.00	21.2	3.24	127	0.00	756	0.00		
0.0189	0.00	0.113	0.00	0.675	0.00	4.03	0.00	24.1	4.54	144	0.00	859	0.00		
0.0215	0.00	0.128	0.00	0.767	0.00	4.58	0.02	27.4	6.13	163	0.00	976	0.00		
0.0244	0.00	0.146	0.00	0.872	0.00	5.21	0.07	31.1	7.89	186	0.00	1110	0.00		
0.0278	0.00	0.166	0.00	0.991	0.00	5.92	0.12	35.3	9.61	211	0.00	1260	0.00		
0.0315	0.00	0.188	0.00	1.13	0.00	6.72	0.17	40.1	11.01	240	0.00	1430	0.00		
0.0358	0.00	0.214	0.00	1.28	0.00	7.64	0.24	45.6	11.77	272	0.00	1630	0.00		
0.0407	0.00	0.243	0.00	1.45	0.00	8.68	0.32	51.8	11.59	310	0.00	1850	0.00		
0.0463	0.00	0.276	0.00	1.65	0.00	9.86	0.42	58.9	10.35	352	0.00	2100	0.00		
0.0526	0.00	0.314	0.00	1.88	0.00	11.2	0.56	66.9	8.17	400	0.00	2390	0.00		

Figure A-6: Particle size distribution of ball-milled composite powder for 20 h.

Appendix B

This appendix includes additional information to illustrate the samples fabricated by the selective laser melting presented in the thesis.

Table B-1: Parameters used in selective laser melting of single track and single layer.

Layer thickness (µm)			30		
Point distance (µm)			60	80	100
Track No.	Laser power (W)	Scanning speed (mm/s)	Exposure time (µs)	Exposure time(µs)	Exposure time(µs)
1	100	200	288	384	480
2	100	400	138	184	230
3	100	600	88	117	147
4	100	800	63	84	105
5	100	1000	48	64	80
6	150	200	288	384	480
7	150	400	138	184	230
8	150	600	88	117	147
9	150	800	63	84	105
10	150	1000	48	64	80
11	200	200	288	384	480
12	200	400	138	184	230
13	200	600	88	117	147
14	200	800	63	84	105
15	200	1000	48	64	80

Table B-2: Parameters used in selective laser melting bulk samples.

P=200W d=30 µm	speed (v, mm/s)	Point distance (lp, µm)	Hatch spacing (h, um)	Exposure time (te, µs)	Rotation angle (◦)	Energy density (E, J/mm^3)
1	100	80	70	784	67	952.4
2	150	80	70	517	67	634.9
3	200	80	70	384	67	476.2
4	300	80	70	250	67	317.5
5	400	80	70	184	67	238
6	600	80	70	117	67	158.7
7	200	80	100	384	67	333.3
8	400	80	100	184	67	166.7
9	600	80	100	117	67	111.1

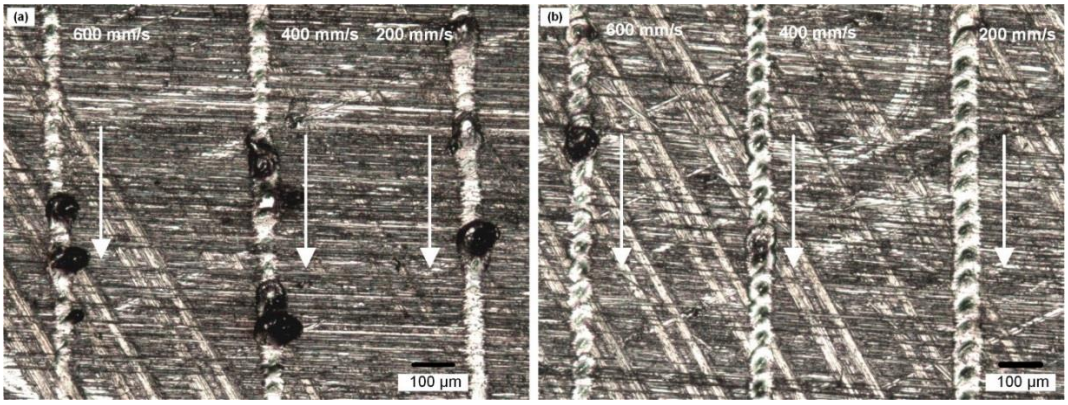

Figure B-1: Fusion lines on substrate with an exposure point distance 60 µm (a) P=100 W and (b) P=150 W

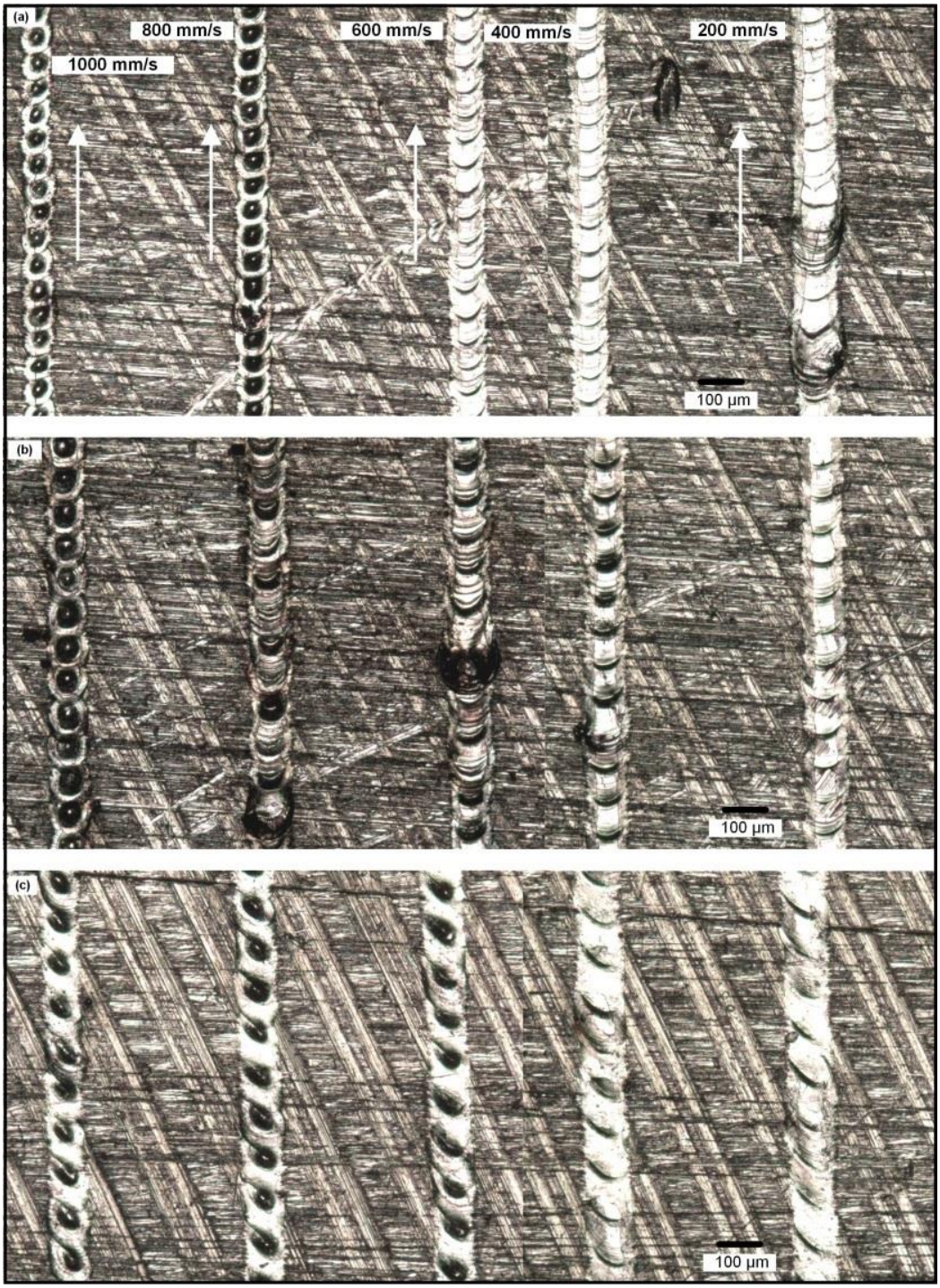

Figure B-2: Fusion lines with laser power 200 W (a) point distance of 60 µm, (b) point distance of 80 µm and (c) point distance of 100 µm

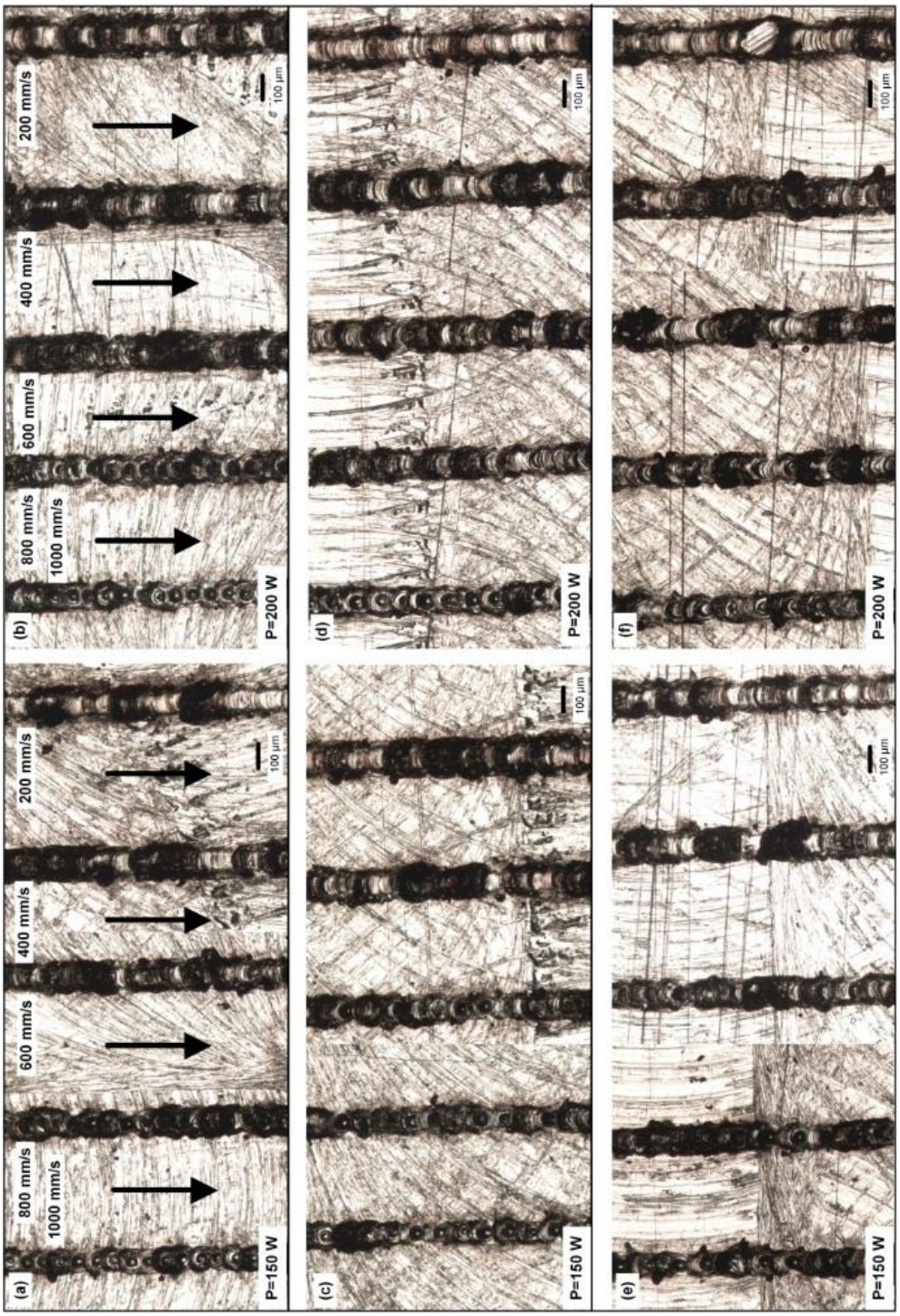

Figure B-3: Single tracks with exposure point distance of 60 µm for (a) and (b), 80 µm for (c) and (d) and 100 µm for (e) and (f)

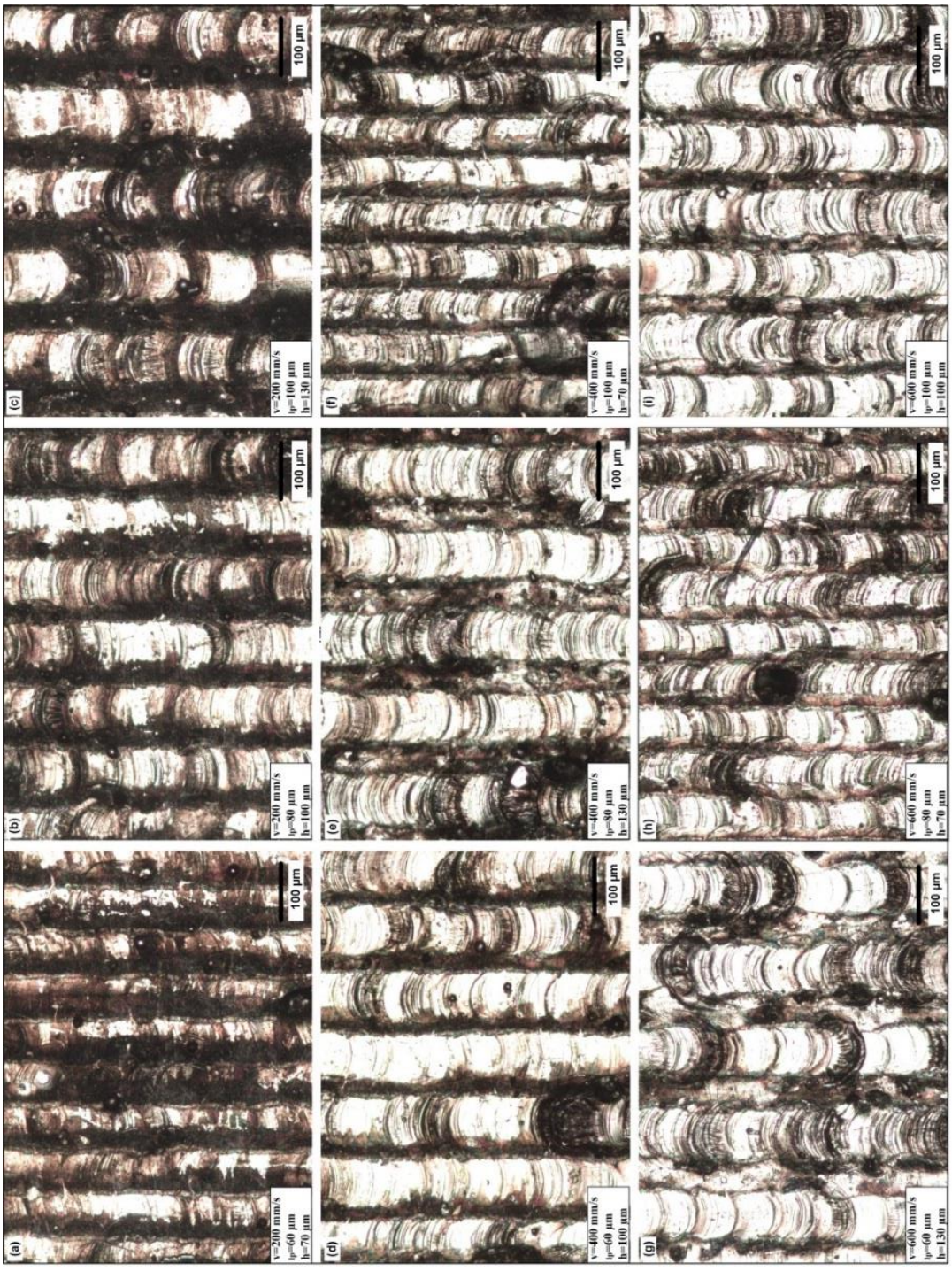

Figure B-4: Single layers with different process parameters combination.

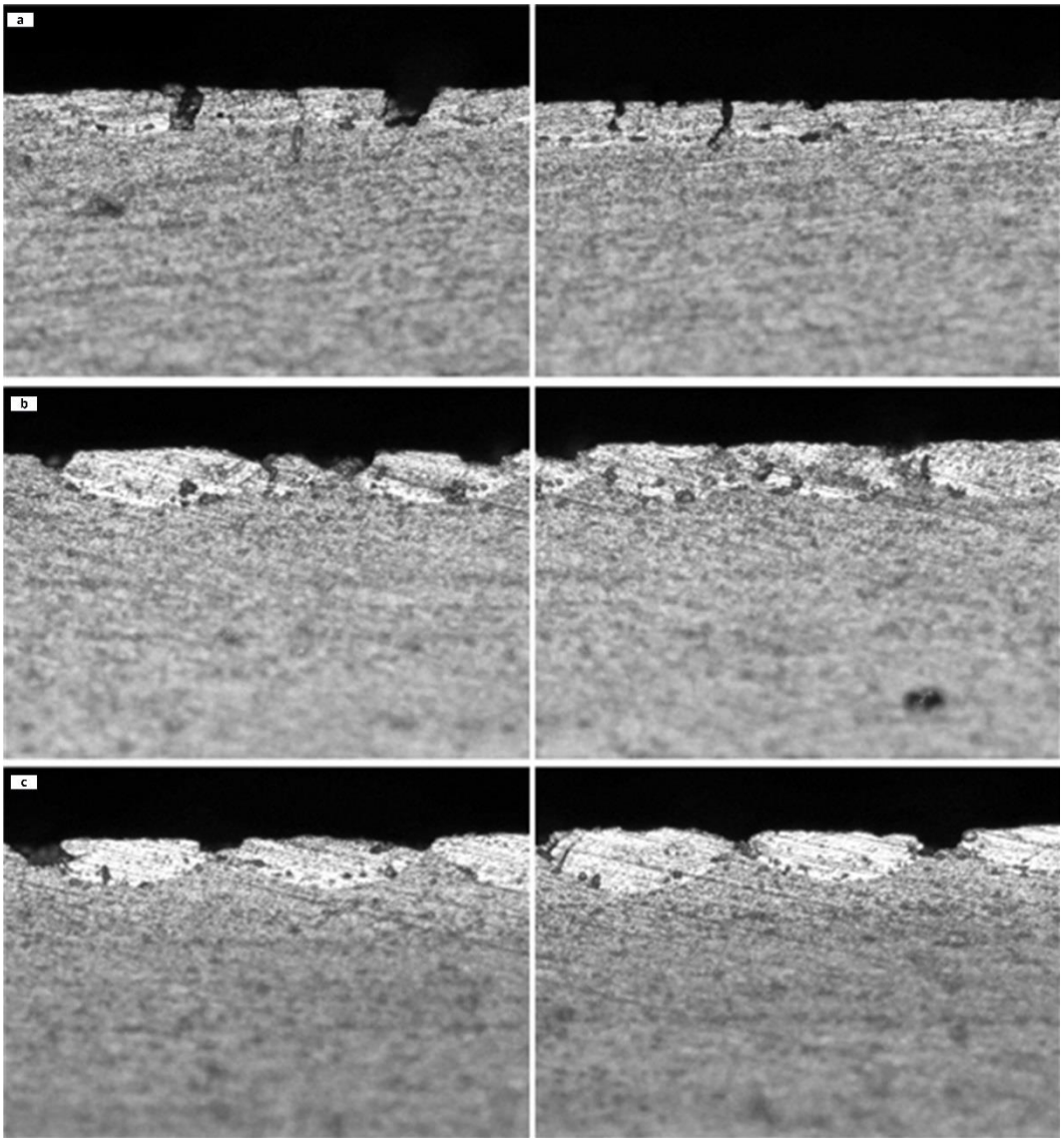

Figure B-5: Cross sections of single layers under 200 W laser power with (a) h=70 µm, (b) h=100 µm and (c) h=130 µm.

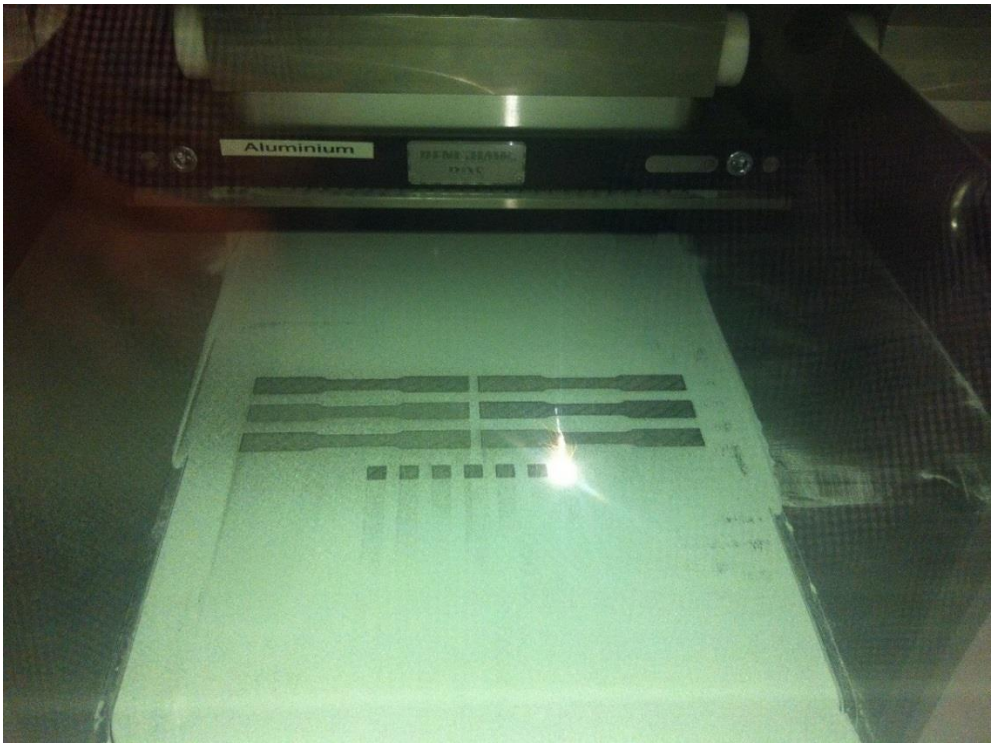

Figure B-6: Photograph showing the selective laser melting process.

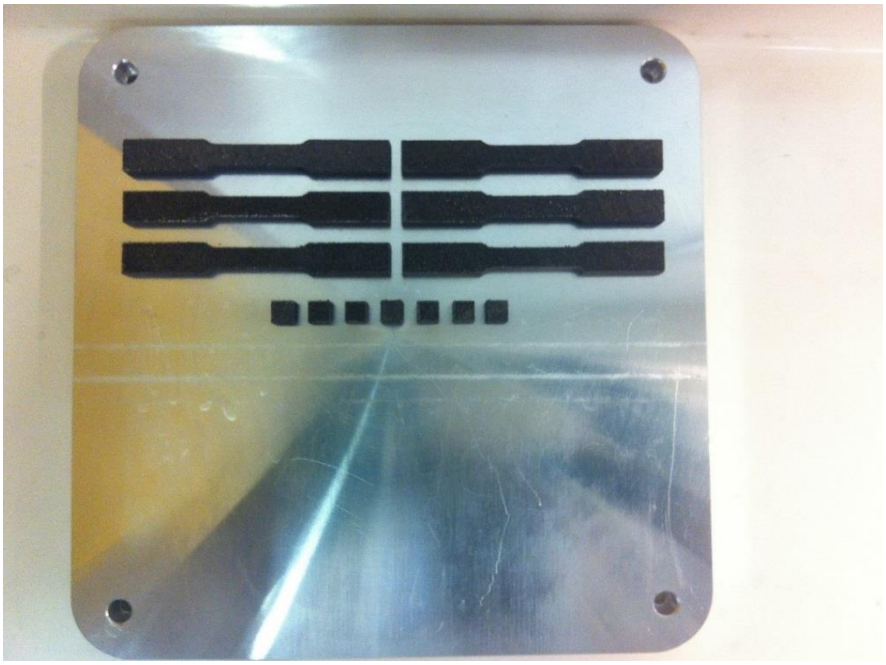

Figure B-7: The fabricated composite samples.

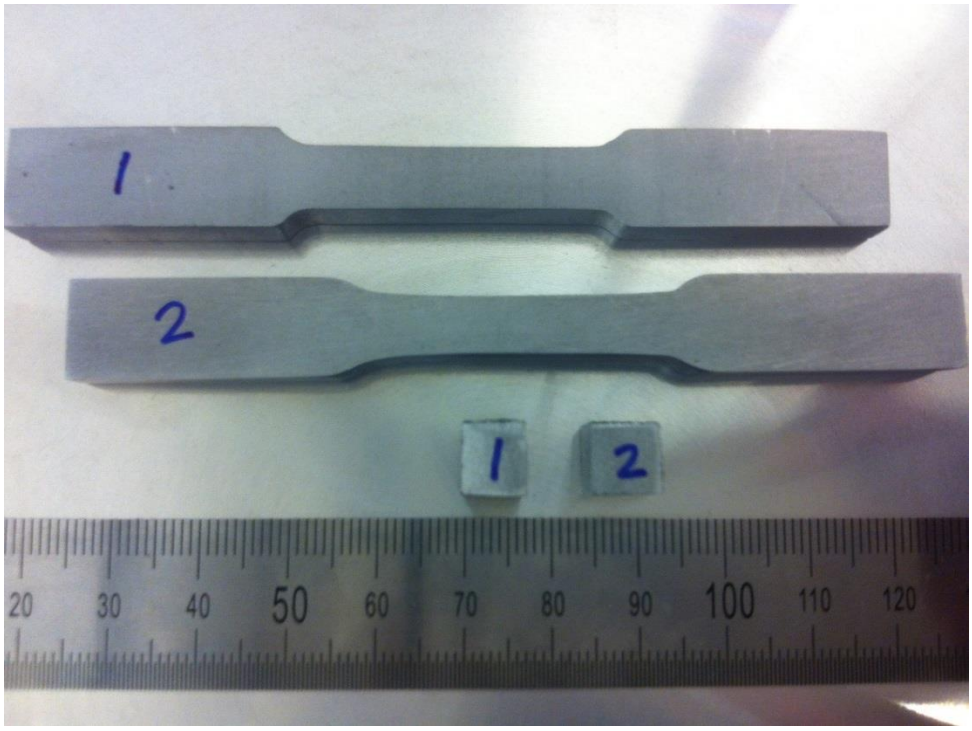

Figure B-8: The grinding composite samples after wire electrical discharge machining (WEDM).

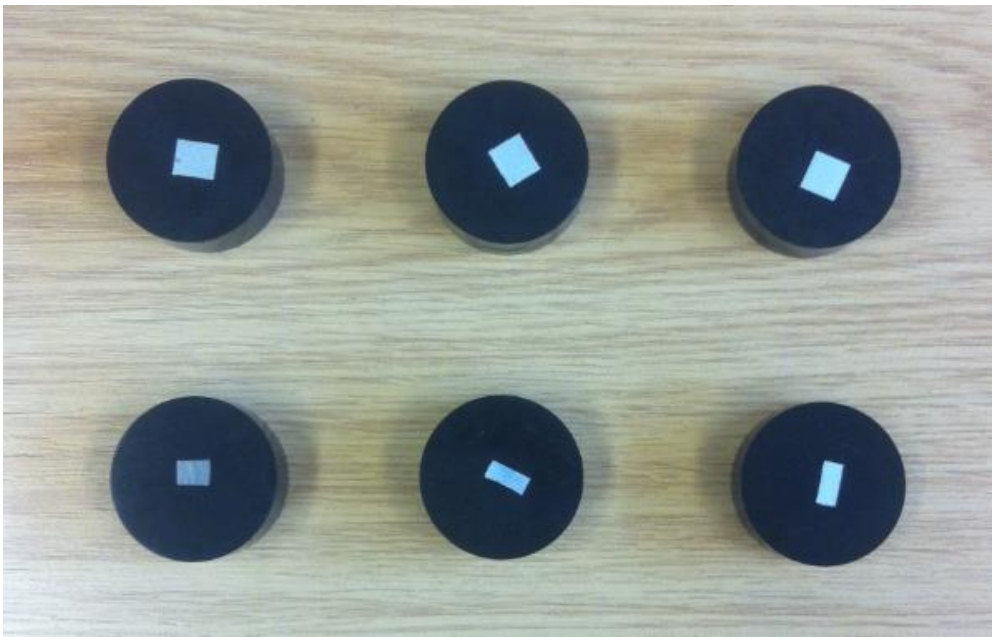

Figure B-9: Samples used in microstructure analysis.

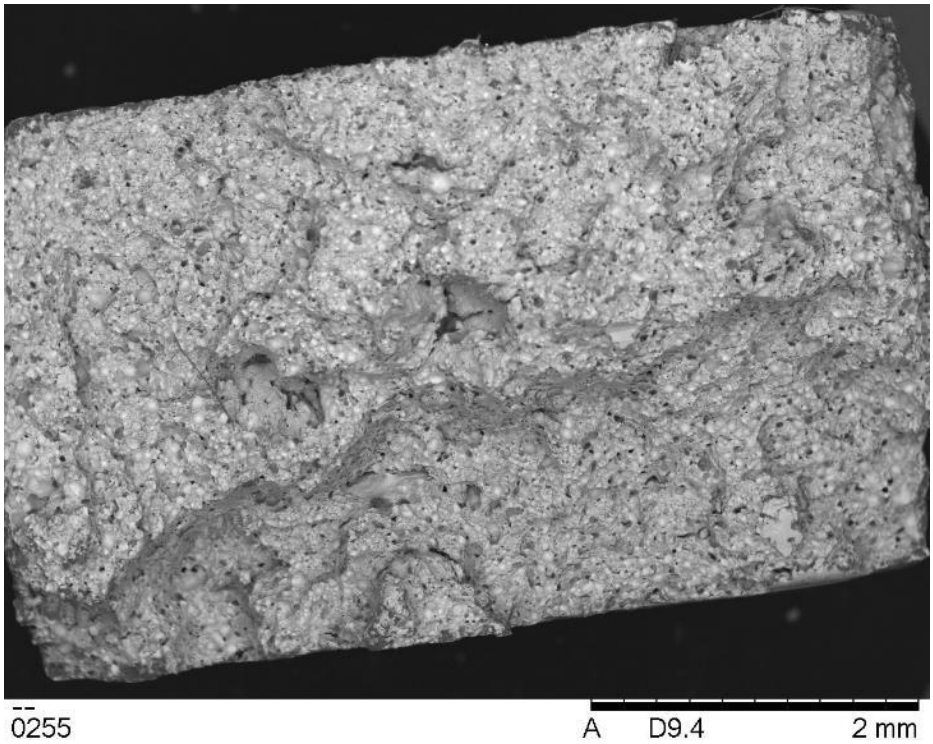

Figure B-10: Fracture surface of the composite sample fabricated at 300 mm/s.

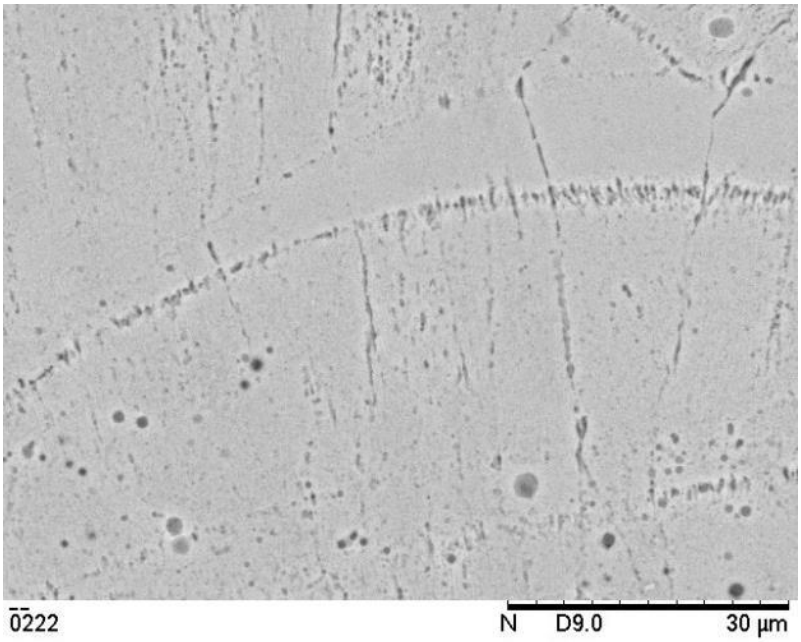

Figure B-11: SEM image showing vertical section of the composite sample fabricated at 300 mm/s.

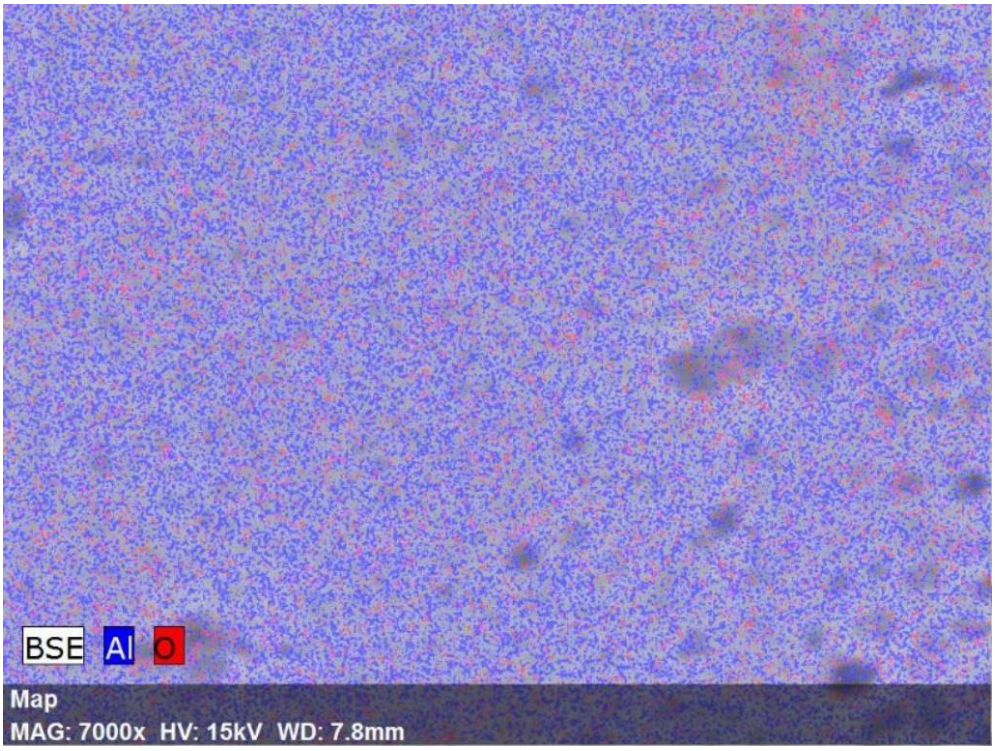

Figure B-12: EDS mapping showing the distribution of Al and O elements of the composite sample fabricated at 300 mm/s.

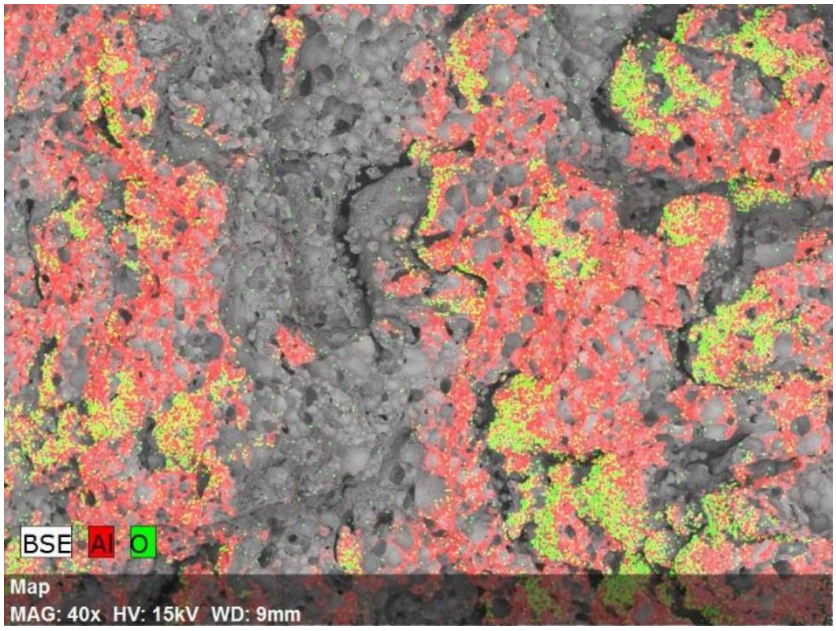

Figure B-13: EDS mapping showing fracture surface oxidation of the composite sample fabricated at 100 mm/s.

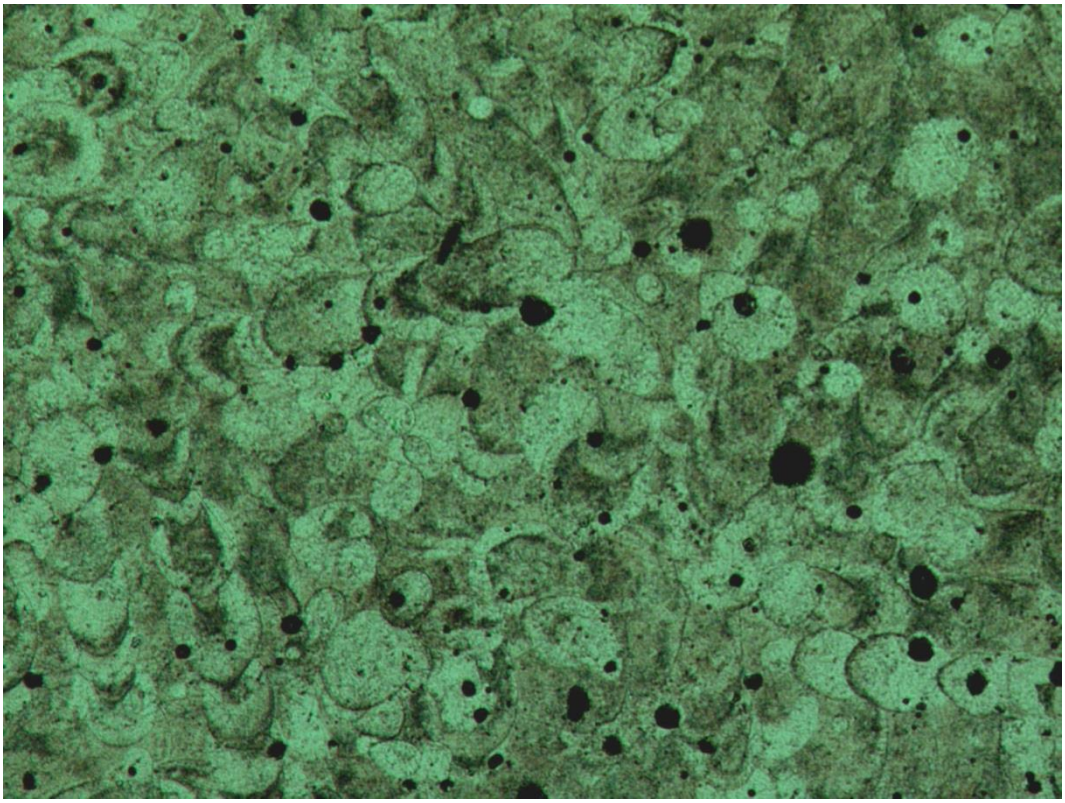

Figure B-14: OM image showing microstructure of the horizontal section of composite sample fabricated at 400 mm/s.

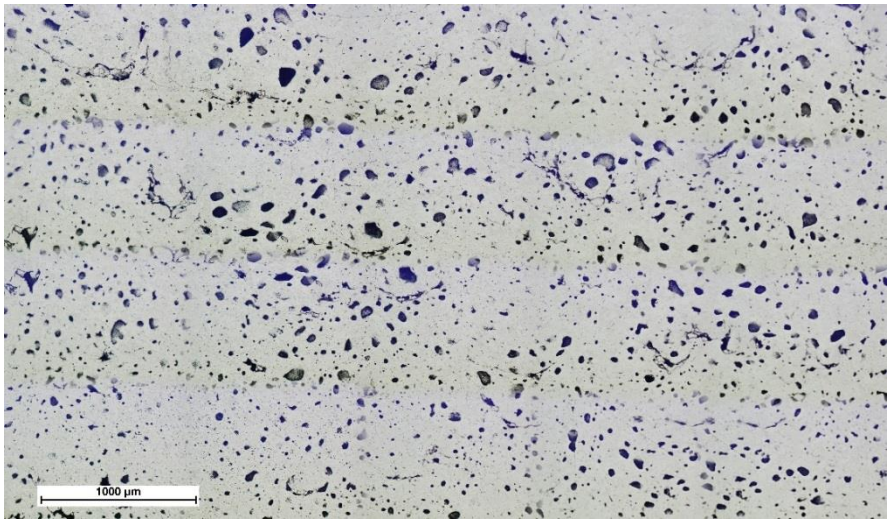

Figure B-15: OM image showing porosity of the vertical section of composite sample fabricated at 100 mm/s

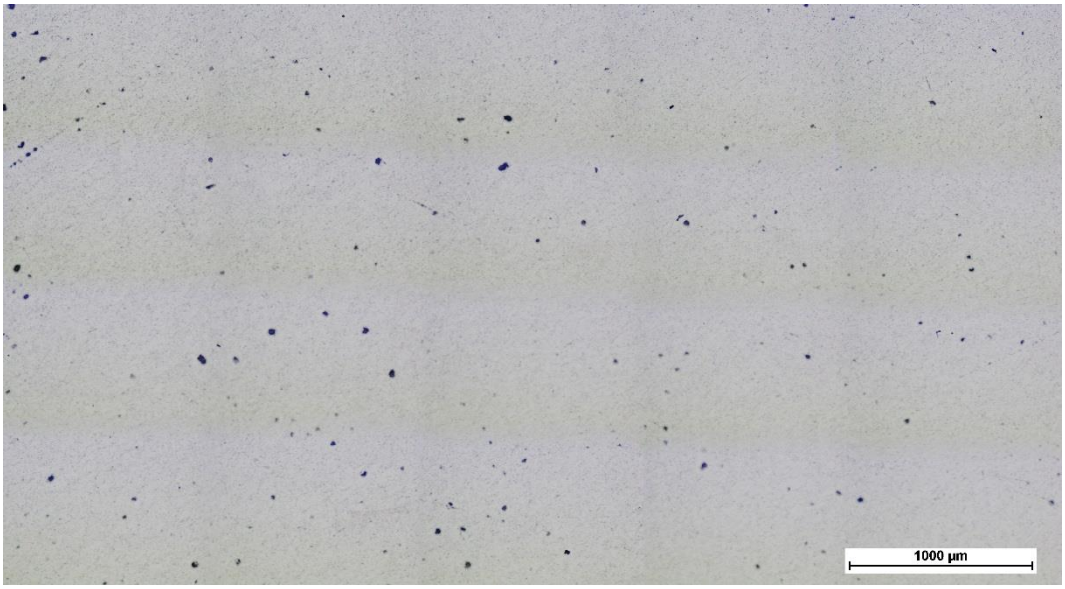

Figure B-16: OM image showing porosity of the vertical section of composite sample fabricated at 200 mm/s

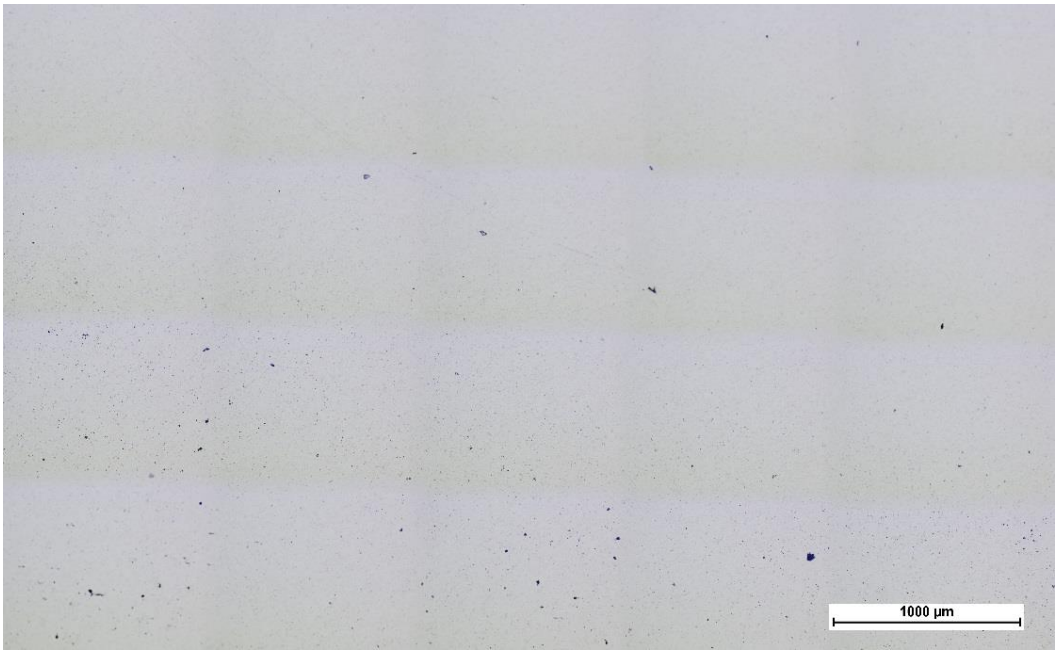

Figure B-17: OM image showing porosity of the vertical section of composite sample fabricated at 300 mm/s

References

Aboulkhair, N.T. et al. 2014. Reducing porosity in AlSi10Mg parts processed by selective laser melting. *Additive Manufacturing* 1, pp. 77–86.

Aboulkhair, N.T. et al. 2016. On the formation of AlSi10Mg single tracks and layers in selective laser melting: Microstructure and nano-mechanical properties. *Journal of Materials Processing Technology* 230, pp. 88–98.

Anisimov, S. and Khokhlov, V. 1995. *Instabilities in laser matter interaction*. CRC press.

Anon Standard Test Methods for Tension Testing of Metallic Materials [Accessed: 7 February 2017].

Bhushan, B. and Kwak, K.J. 2007. Velocity dependence of nanoscale wear in atomic force microscopy. *Applied Physics Letters* 91, p. 163113.

Buchbinder, D. et al. 2008. Rapid manufacturing of aluminium parts for serial production via selective laser melting (SLM). *International Conference on Rapid Manufacturing*. Loughborough, pp. 2394–2440.

Cain, J. 2002. Flowability Testing-An Alternative Technique fore Determining ANSI/CEMA Standard 550 Flowability Ratings for Granular Materials. *Powder Handling and Processing* 14, pp. 218–220.

Carr, R. 1965. Classifying flow properties of solids. *Chemical Engineering* 72, p. 69.

Childs, T. 2005. Selective laser sintering (melting) of stainless and tool steel powders: experiments and modelling. *Proceedings of the Instution of Mechanical Engineers, Part B: Journal of Engineering Manufacture* 219, pp. 339–357.

Childs, T.H.C. et al. 2004. Mapping and Modelling Single Scan Track Formation in Direct Metal Selective Laser Melting. *CIRP Annals - Manufacturing Technology* 53, pp. 191–194.

Cho, M.H. 2009. The role of transfer film and back transfer behavior on the tribological performance of polyoxymethylene in sliding. *Journal of Mechanical science and Technology* 23, pp. 2291–2298.

Choi, H.J. et al. 2008. Tensile behavior of bulk nanocrystalline aluminum synthesized by hot extrusion of ball-milled powders. *Scripta Materialia* 59, pp. 1123–1126.

Chung, K.-H. et al. 2003. Fundamental investigation of micro wear rate using an atomic force microscope. *Tribology Letters* 15, pp. 135–144.

Chung, K.H. and Kim, D.E. 2007. Wear characteristics of diamond-coated atomic force microscope probe. *Ultramicroscopy* 108, pp. 1–10.

Cintas, J. et al. 2005. High-strength PM aluminium by milling in ammonia gas and sintering. *Scripta Materialia* 53, pp. 1165–1170.

Clare, A.T. et al. 2008. Selective laser melting of high aspect ratio 3D nickel-titanium structures two way trained for MEMS applications. *International Journal of Mechanics and Materials in Design* 4, pp. 181–187.

Dadbakhsh, S. et al. 2012. Experimental investigation on selective laser melting behaviour and processing windows of in situ reacted Al/Fe_2O_3 powder mixture. *Powder Technology* 231, pp. 112–121.

Dahotre, N.B. and Harimakar, S.P. 2008. *Laser fabrication and machining of materials*. Springer Science and Business Media.

Dai, K. and Shaw, L. 2002. Distortion minimization of laser-processed components through control of laser scanning patterns. *Rapid Prototyping Journal* 8, pp. 270–276.

Dong, L. et al. 2009. Three-dimensional transient finite element analysis of the selective laser sintering process. *Journal of Materials Processing Technology* 209, pp. 700–706.

Durai, T.G. et al. 2007. Synthesis and characterization of Al matrix composites reinforced by in situ alumina particulates. *Materials Science and Engineering A* 445, pp. 100–105.

Fischer, P. et al. 2003. Sintering of commercially pure titanium powder with a Nd:YAG laser source. *Acta Materialia* 51, pp. 1651–1662.

Geng, Y. et al. 2014. Depth prediction model of nano-grooves fabricated by AFM-based multi-passes scratching method. *Applied Surface Science* 313, pp. 615–623.

Gibson, I. et al. 2010. *Additive manufacturing technologies: Rapid prototyping to direct digital manufacturing*.

Gnecco, E. et al. 2002. Abrasive wear on the atomic scale. *Physical Review Letters* 88, p. 215501.

Gu, D. et al. 2011. Nanocrystalline TiC reinforced Ti matrix bulk-form nanocomposites by Selective Laser Melting (SLM): Densification, growth mechanism and wear behavior. *Composites Science and Technology* 71, pp. 1612–1620.

Gu, D. et al. 2015. Rapid fabrication of Al-based bulk-form nanocomposites with novel reinforcement and enhanced performance by selective laser melting. *Scripta Materialia* 96, pp. 25–28.

Gu, D. et al. 2012. Laser additive manufacturing of metallic components: materials, processes and mechanisms. *International Materials Reviews* 57, pp. 133–164.

Guan, K. et al. 2013. Effects of processing parameters on tensile properties of selective laser melted 304 stainless steel. *Materials and Design* 50, pp. 581–586.

Haboudou, A. et al. 2003. Reduction of porosity content generated during Nd: YAG laser welding of A356 and AA5083 aluminium alloys. *Materials Science and Engineering A* 363, pp. 40–52.

Han, Q. et al. 2016. Synthesis and characterisation of advanced ball-milled Al-Al_2O_3 nanocomposites for selective laser melting. *Powder Technology* 297, pp. 183–192.

Han, Q. et al. 2017a. Characterisation and milling time optimisation of nanocrystalline aluminium powder for selective laser melting. *International Journal of Advanced Manufacturing Technology* 88, pp. 1429–1438.

Han, Q. et al. 2017b. Selective laser melting of advanced Al-Al_2O_3 nanocomposites: Simulation, microstructure and mechanical properties. *Materials Science and Engineering A* 698, pp. 162–173.

Han, Q. et al. 2017c. Macro and nanoscale wear behaviour of Al-Al_2O_3 nanocomposites fabricated by selective laser melting. *Composites Part B: Engineering* 127, pp. 26–35.

Harrison, N.J. et al. 2015. Reduction of micro-cracking in nickel superalloys processed by Selective Laser Melting: A fundamental alloy design approach. *Acta Materialia* 94, pp. 59–68.

Hatch J.E. 1984. Aluminum Properties and Physical Metallurgy. *ASM ,Ohio, US*.

Hussein, A. et al. 2013. Finite element simulation of the temperature and stress fields in single layers built without-support in selective laser melting. *Materials and Design* 52, pp. 638–647.

Jue, J. et al. 2017. Microstructure evolution and mechanical properties of Al-Al_2O_3 composites fabricated by selective laser melting. *Powder Technology* 310, pp. 80–91.

Kalpakjian, S. and Schmid, S.R. 2014. *Manufacturing engineering and technology*. Seventh Ed. Sekar, K. V. ed. Prentice Hall, Pearson Education South Asia Pte Ltd., Singapore.

Kang, N. et al. 2016. Wear behavior and microstructure of hypereutectic Al-Si alloys prepared by selective laser melting. *Applied Surface Science* 378, pp. 142–149.

Kang, Y.C. and Chan, S.L.I. 2004. Tensile properties of nanometric Al_2O_3 particulate-reinforced aluminum matrix composites. *Materials Chemistry and Physics* 85, pp. 438–443.

Kempen, K. et al. 2011. Process optimization and microstructural analysis for selective laser melting of AlSi10Mg. In: *22nd Annual International Solid Freeform Fabrication Symposium - An Additive Manufacturing Conference, SFF 2011*. pp. 484–495.

Khairallah, S.A. et al. 2016. Laser powder-bed fusion additive manufacturing: Physics of complex melt flow and formation mechanisms of pores, spatter, and denudation zones. *Acta Materialia* 108, pp. 36–45.

Khan, A.S. et al. 2008. Effect of grain refinement on mechanical properties of ball-milled bulk aluminum. *Materials Science and Engineering A* 489, pp. 77–84.

Khorshid, M.T. et al. 2010. Mechanical properties of tri-modal Al matrix composites reinforced by nano- and submicron-sized Al_2O_3 particulates developed by wet attrition milling and hot extrusion. *Materials and Design* 31, pp. 3880–3884.

Kim, H.J. et al. 2012. Nano-scale wear: A review. *International Journal of Precision Engineering and Manufacturing* 13, pp. 1709–1718.

Kimura, T. et al. 2017. Effect of silicon content on densification, mechanical and thermal properties of Al-xSi binary alloys fabricated using selective laser melting. *Materials Science and Engineering: A* 682, pp. 593–602.

King, W.E. et al. 2014. Observation of keyhole-mode laser melting in laser powder-bed fusion additive manufacturing. *Journal of Materials Processing Technology* 214, pp. 2915–2925.

Koli, D.K. et al. 2013. Properties and characterization of Al-Al_2O_3 composites processed by casting and powder metallurgy routes. *International Journal of Latest Trends in Engineering and Technology* 2, pp. 486–496.

Kolossov et al. 2004. 3D FE simulation for temperature evolution in the selective laser sintering process. *International Journal of Machine Tools and Manufacture* 44, pp. 117–123.

Kruth, J.P. et al. 2004. Selective laser melting of iron-based powder. *Journal of Materials Processing Technology* 149, pp. 616–622.

Kumar, A. et al. 2013. Fabrication and characterization of A359/Al_2O_3 metal matrix composite using electromagnetic stir casting method. *Journal of Materials*

Research and Technology 2, pp. 250–254.

Li, R. et al. 2012. Balling behavior of stainless steel and nickel powder during selective laser melting process. *International Journal of Advanced Manufacturing Technology* 59, pp. 1025–1035.

Li, X.P. et al. 2016. Selective laser melting of Al-12Si alloy: Enhanced densification via powder drying. *Additive Manufacturing* 10, pp. 10–14.

Li, Y. and Gu, D. 2014. Parametric analysis of thermal behavior during selective laser melting additive manufacturing of aluminum alloy powder. *Materials and Design* 63, pp. 856–867.

Liao, J. and Tan, M.-J. 2011. Mixing of carbon nanotubes (CNTs) and aluminum powder for powder metallurgy use. *Powder Technology* 208, pp. 42–48.

Limmaneevichitr, C. and Kou, S. 2000. Visualization of Marangoni convection in simulated weld pools containing a surface-active agent. *Welding Journal* 79, pp. 324–330.

Lloyd, D.J. 1994. Particle reinforced aluminium and magnesium matrix composites. *International Materials Reviews* 39, pp. 1–23.

Louvis, E. et al. 2011. Selective laser melting of aluminium components. *Journal of Materials Processing Technology* 211, pp. 275–284.

Matsumoto, M. et al. 2002. Finite element analysis of single layer forming on metallic powder bed in rapid prototyping by selective laser processing. *International Journal of Machine Tools and Manufacture* 42, pp. 61–67.

Mazahery, a. et al. 2009. Development of high-performance A356/nano-Al_2O_3 composites. *Materials Science and Engineering A* 518, pp. 61–64.

Mercelis, P. and Kruth, J. 2006. Residual stresses in selective laser sintering and selective laser melting. *Rapid Prototyping Journal* 12, pp. 254–265.

Murty, S.V.S.N. et al. 2003. On the hot working characteristics of 6061Al–SiC and 6061–Al_2O_3 particulate reinforced metal matrix composites. *Composites Science and Technology* 63, pp. 119–135.

Natarajan, N. et al. 2006. Wear behaviour of A356/25SiCp aluminium matrix composites sliding against automobile friction material. *Wear* 261, pp. 812–822.

Ozden, S. et al. 2007. Investigation of impact behaviour of aluminium based SiC particle reinforced metal-matrix composites. *Composites Part A: Applied Science and Manufacturing* 38, pp. 484–494.

Patil, R.B. and Yadava, V. 2007. Finite element analysis of temperature distribution in single metallic powder layer during metal laser sintering.

International Journal of Machine Tools and Manufacture 47, pp. 1069–1080.

Poirier, D. et al. 2010. Fabrication and properties of mechanically milled alumina/aluminum nanocomposites. *Materials Science and Engineering A* 527, pp. 7605–7614.

Prabhu, B. et al. 2006. Synthesis and characterization of high volume fraction Al-Al_2O_3 nanocomposite powders by high-energy milling. *Materials Science and Engineering A* 425, pp. 192–200.

Prashanth, K.G. et al. 2014. Microstructure and mechanical properties of Al–12Si produced by selective laser melting: Effect of heat treatment. *Materials Science and Engineering: A* 590, pp. 153–160.

Rahimian, M. et al. 2009. The effect of particle size, sintering temperature and sintering time on the properties of Al-Al_2O_3 composites, made by powder metallurgy. *Journal of Materials Processing Technology* 209, pp. 5387–5393.

Ramnath, B. V et al. 2014. Aluminium metal matrix composites - A review. *Reviews on Advanced Materials Science* 38, pp. 55–60.

Rao, H. et al. 2016. The influence of processing parameters on aluminium alloy A357 manufactured by Selective Laser Melting. *Materials and Design* 109, pp. 334–346.

Razavi Tousi, S.S. et al. 2009. Production of Al-20wt.% Al_2O_3 composite powder using high energy milling. *Powder Technology* 192, pp. 346–351.

Read, N. et al. 2015. Selective laser melting of AlSi10Mg alloy: Process optimisation and mechanical properties development. *Materials and Design* 65, pp. 417–424.

Roberts, I.A. et al. 2009. A three-dimensional finite element analysis of the temperature field during laser melting of metal powders in additive layer manufacturing. *International Journal of Machine Tools and Manufacture* 49, pp. 916–923.

Simchi, A. 2006. Direct laser sintering of metal powders : Mechanism , kinetics and microstructural features. *Materials Science and Engineering: A* 428, pp. 148–158.

Song, B. et al. 2014. Vacuum heat treatment of iron parts produced by selective laser melting: Microstructure, residual stress and tensile behavior. *Materials and Design* 54, pp. 727–733.

Srivatsan, T.S. et al. 1991. Processing techniques for particulate-reinforced metal aluminium matrix composites. *Journal of Materials Science* 26, pp. 5965–5978.

Steen, W. et al. 2010. *Laser material processing*. Springer Science and Business

Media.

Su, H. et al. 2012. Processing, microstructure and tensile properties of nano-sized Al2O3 particle reinforced aluminum matrix composites. *Materials and Design* 36, pp. 590–596.

Sun, Y. et al. 2014. Sliding wear characteristics and corrosion behaviour of selective laser melted 316L stainless steel. *Journal of Materials Engineering and Performance* 23, pp. 518–526.

Sun, Z. et al. 2016. Selective laser melting of stainless steel 316L with low porosity and high build rates. *Materials and Design* 104, pp. 197–204.

Surappa, M.K. 2003. Aluminium matrix composites: Challenges and opportunities. *Sadhana* 28, pp. 319–334.

Suryanarayana, C. 2001. Mechanical alloying and milling. *Progress in Materials Science* 46, pp. 1–184.

Thijs, L. et al. 2010. A study of the microstructural evolution during selective laser melting of Ti-6Al-4V. *Acta Materialia* 58, pp. 3303–3312.

Thijs, L. et al. 2013. Fine-structured aluminium products with controllable texture by selective laser melting of pre-alloyed AlSi10Mg powder. *Acta Materialia* 61, pp. 1809–1819.

Thummler, F. and Oberacker, R. 1993. *An Introduction to Powder Technology*. London: The University Press.

Tolochko, N.K. et al. 2000. Absorptance of powder materials suitable for laser sintering. *Rapid Prototyping Journal* 6, pp. 155–161.

Vandenbroucke, B. and Kruth, J. 2007. Selective laser melting of biocompatible metals for rapid manufacturing of medical parts. *Rapid Prototyping Journal* 13, pp. 196–203.

Varenberg, M. et al. 2003. An improved wedge calibration method for lateral force in atomic force microscopy. *Review of Scientific Instruments* 74, pp. 3362–3367.

Wang, F. and Zhao, X. 2007. Effect of contact stiffness on wedge calibration of lateral force in atomic force microscopy. *Review of Scientific Instruments* 78, p. 43701.

Wang, X. et al. 2015. Humidity dependence of tribochemical wear of monocrystalline silicon. *ACS applied materials and interfaces* 7, pp. 14785–14792.

Yadroitsev, I. et al. 2007. Parametric analysis of the selective laser melting process. *Applied Surface Science* 253, pp. 8064–8069.

Yadroitsev, I. et al. 2007. Strategy of manufacturing components with designed internal structure by selective laser melting of metallic powder. *Applied Surface Science* 254, pp. 980–983.

Yadroitsev, I. 2009. *Selective laser melting: Direct manufacturing of 3D-objects by selective laser melting of metal powders*. Saarbrucken: Lambert Academic Publishing.

Yadroitsev, I. et al. 2010. Single track formation in selective laser melting of metal powders. *Journal of Materials Processing Technology* 210, pp. 1624–1631.

Zebarjad, S.M. and Sajjadi, S.A. 2007. Dependency of physical and mechanical properties of mechanical alloyed Al-Al_2O_3 composite on milling time. *Materials and Design* 28, pp. 2113–2120.

Zebarjad, S.M. and Sajjadi, S. a. 2006. Microstructure evaluation of Al-Al_2O_3 composite produced by mechanical alloying method. *Materials and Design* 27, pp. 684–688.

Zhang, D.L. 2004. Processing of advanced materials using high-energy mechanical milling. *Progress in Materials Science* 49, pp. 537–560.

Zhang, F. et al. 2016. Friction behavior in nanoscratching of reaction bonded silicon carbide ceramic with Berkovich and sphere indenters. *Tribology International* 97, pp. 21–30.

Zhang, H. et al. 2016. Selective laser melting of high strength Al-Cu-Mg alloys: Processing, microstructure and mechanical properties. *Materials Science and Engineering A* 656, pp. 47–54.